ABSTRACT

Title of dissertation: CLASSICAL AND QUANTUM DYNAMICS
OF BOSE-EINSTEIN CONDENSATES

Ranchu Mathew, Doctor of Philosophy, 2017

Dissertation directed by: Professor Eite Tiesinga
Department of Physics

After the first experimental realization of a Bose-Einstein condensate (BEC) in 1995, BECs have become a subject of intense experimental and theoretical study. In this dissertation, I present our results on the classical and quantum dynamics of BECs at zero temperature under different scenarios.

First, I consider the analog of slow light in the collision of two BECs near a Feshbach resonance. The scattering length then becomes a function of the collision energy. I derive a generalization of the Gross-Pitaevskii equation for incorporating this energy dependence. In certain parameter regimes, the group velocity of a BEC traveling through another BEC decreases. I also study the feasibility of an experimental realization of this phenomena.

Second, I analyze an experiment in which a BEC in a ring-shaped trap is stirred by a rotating barrier. The phase drop across and current flow through the barrier

is measured from spiral-shaped density profiles created by interfering the BEC in the ring-shaped trap and a concentric reference BEC after release from all trapping potentials. I show that a free-particle expansion is sufficient to explain the origin of the spiral pattern and relate the phase drop to the geometry of a spiral. I also bound the expansion times for which the phase drop can be accurately determined and study the effect of inter-atomic interactions on the expansion time scales.

Third, I study the dynamics of few-mode BECs when they become dynamically unstable after preparing an initial state at a saddle point of the Hamiltonian. I study the dynamics within the truncated Wigner approximation (TWA) and find that, due to phase-space mixing, the expectation value of an observable relaxes to a steady-state value. Using the action-angle formalism, we derive analytical expressions for the steady-state value and the time evolution towards this value. I apply these general results to two systems: a condensate in a double-well potential and a spin-1 (spinor) condensate.

Finally, I study quantum corrections beyond the TWA in the semiclassical limit. I derive general expressions for the dynamics of an observable by using the van Vleck-Gutzwiller propagator and find that the interference of classical paths leads to non-perturbative corrections. As a case study, I consider a single-mode nonlinear oscillator; this system displays collapse and revival of observables. I find that the interference of classical paths, which is absent in the TWA, leads to revivals.

CLASSICAL AND QUANTUM DYNAMICS
OF BOSE-EINSTEIN CONDENSATES

by

Ranchu Mathew

Dissertation submitted to the Faculty of the Graduate School of the
University of Maryland, College Park in partial fulfillment
of the requirements for the degree of
Doctor of Philosophy
2017

Advisory Committee:
Professor Jay Deep Sau, Chair
Professor Eite Tiesinga, Co-Chair/Advisor
Professor William Dorland
Professor Dionisios Margetis
Professor Jacob Taylor

Dedicated to my parents for their love.

Acknowledgments

First and foremost, I acknowledge and thank my advisor Eite Tiesinga for his constant support and guidance in the last five and half years. Honestly, he is one of the coolest people I have met in my life. His cheerful disposition and availability for discussions (many a time they were day-long) have been vital for my research. I hope to emulate his intellectual honesty and approach to physics. Also, I am grateful for the freedom Eite gave me to work on my own projects at my own pace.

Next, I would like to thank others with whom I had the opportunity to do research. I owe special thanks to Banibrata Mukhopadhyay for my first research project in physics and for his help in getting me into graduate school. I thank Ted Jacobson for guiding me through my first research problem of my graduate studies. I would like to thank my other collaborators: Stephen Eckel, Mark Edwards, Jacob Taylor, and Minh Tran. Working with them has been an enriching experience. Also, I am grateful for the discussions that I had with Wrick Sengupta and Efim Rozenbaum, which were fruitful for the later part of my dissertation.

I would like to thank Jacob Taylor, Bill Dorland, and Dionisios Margetis for agreeing to serve as the members of my dissertation committee, and Jay Deep Sau for chairing the committee. Also, I thank Dionisios Margetis for organizing a RIT on atomic physics, which led to some interesting discussions.

Eight years is a long time, even for a doctorate. Throughout these years, I made many wonderful friends. I would like to thank them, especially, Jonathan, Arijit, Wrick, Biswadip, Anup & Sofia, Siddharth, David, Margaret, Tom & Barbara,

iii

Table of Contents

List of Tables

List of Figures

Chapter 1:   General introduction

In 1925 Albert Einstein predicted that a gas of non-interacting bosons at low temperatures [1] condenses into a single quantum state, forming a Bose-Einstein condensate (BEC). Seventy years later, a research group led by Carl Wieman and Eric Cornell [2] experimentally realized BEC in ultracold atoms. It was a result of a concerted experimental effort made possible by the development of novel cooling and trapping techniques. Advances in these technologies have led to an explosion of innovations in the field of ultracold physics. For example, ultracold atoms are now used in quantum simulation and computation.

Bose-Einstein condensation in a weakly interacting gas of bosons occurs when the thermal de Broglie wavelength is comparable to the typical inter-particle separation. Then, a macroscopic fraction of particles occupy the same quantum state below a critical temperature T_c. At zero temperature, this fraction is almost one. This condensation is a so-called continuous phase transition, with an order parameter which is zero and non-zero for temperatures above and below T_c, respectively. For a weakly-interacting BEC, this order parameter is a complex function of space and time, and describes the mode that is macroscopically occupied. In the mean-field limit, the dynamics of this order parameter is governed by the time-dependent

Gross-Pitaevskii equation [3]. We briefly describe the theory of BEC in Sec. 1.1. An introduction to BEC physics would be incomplete without a look into the experimental techniques used for their creation. These techniques will be briefly discussed in Sec. 1.2.

Macroscopic occupation of a single mode leads to coherence. Shortly after the first experimental realization of a BEC, a group led by Wolfgang Ketterle demonstrated coherence by interfering two BECs. The coherence of a BEC is similar to that of a laser. As a matter of fact, the field of atom optics is based on finding analogs of optical phenomena using atoms. For example, atomic lasers [4, 5], mirrors and beam splitters [6] have been realized. In chapter 2, I study the collision of two BECs near a Feshbach resonance and find that, analogous to slow light, a BEC slows down when traveling through another BEC.

Furthermore, coherent control and transport of ultracold atoms have led to the creation of the field of atomtronics, which deals with atomic analogs of electronic components. Though the field is still in a nascent stage, atomic analogs of circuit elements like capacitors and transistors have been experimentally realized. In chapter 3, I analyze an experimental realization of one such system, namely an atomic analog of a superconducting quantum interference device.

In optical interferometry, the relative error of a measurement using uncorrelated photons is $1/\sqrt{N}$, where N is the number of photons used in the measurement. This is the so-called standard quantum limit. To go beyond this limit, correlated photons in squeezed states are produced using the Kerr nonlinearity of the medium. This nonlinearity is usually very weak for photons. In contrast, nonlinearity in ultra-

cold atoms, which stems from atom-atom interactions, is much stronger. Squeezed states in atoms can be prepared by evolving a BEC from a dynamically unstable point of its mean-field Hamiltonian. They have been used in interferometric measurements that beat the standard quantum limit [7]. In chapter 4, I study the dynamics following dynamical instability in two few-mode bosonic systems: a condensate in a double-well potential and a spinor gas under a single-mode approximation.

1.1 Theory of Bose-Einstein condensates

A classical gas in thermal equilibrium obeys Maxwell-Boltzmann statistics. A classical treatment is valid when the particles are distinguishable and quantum effects become important when this distinguishability breaks down. Quantum degeneracy occurs when the de Broglie wavelength ($\lambda = h/p$, where h is Planck's constant and p is the momentum) of a particle is comparable to the average inter-particle distance $d = n^{-1/3}$, where n is the particle number density. As the typical momentum of a particle at temperature T scales as $(mk_BT)^{1/2}$, the degeneracy temperature $T_{\deg} \sim \hbar^2 n^{2/3}/(k_B m)$, where $\hbar = h/(2\pi)$ and k_B is the Boltzmann constant. For fermions, this temperature is the Fermi temperature, which in normal metals is typically in the range 200-300 K due to the small mass of an electron. Thus, for metals, quantum effects are important even at room temperature. In contrast, in atomic bosonic systems the degeneracy temperature is much lower because of the larger atomic mass. In Helium-4, a light atom, the degeneracy sets in at around 2 K

leading to a transition from a normal fluid to a superfluid. In ultracold atoms, quantum degeneracy occurs at much lower nanokelvin temperatures as their densities are much lower than air at room temperature and pressure.

Condensation in a degenerate non-interacting Bose gas occurs because the density of the thermal fraction of the gas has an upper bound. When this upper bound is reached increasing the density or lowering the temperature leads to a macroscopic occupation of the single-particle ground state, i.e., a BEC is formed. This picture remains qualitatively correct when the Bose gas is weakly interacting.

1.1.1 Definition of a BEC

There are several ways of defining the presence of a BEC in an interacting many-body system. The first definition invokes the concept of spontaneous symmetry breaking. Let the annihilation and creation operators of a particle, at position $\mathbf{x} = (x_1, \cdots, x_d)$ in a d-dimensional space and time t, be $\widehat{\psi}(\mathbf{x}, t)$ and $\widehat{\psi}^\dagger(\mathbf{x}, t)$, respectively. They obey the commutation relation $[\widehat{\psi}(\mathbf{x}, t), \widehat{\psi}^\dagger(\mathbf{x}', t)] = \delta(\mathbf{x} - \mathbf{x}')$. Then, in the presence of a condensate $\psi(\mathbf{x}, t) = \left\langle \widehat{\psi}(\mathbf{x}, t) \right\rangle$, the expectation value with respect to the many-body quantum state, has a finite value, breaking the global phase invariance.

Onsager and Penrose [8,9], on the other hand, defined a BEC using the single-particle density matrix $\left\langle \widehat{\psi}^\dagger(\mathbf{x}, t) \widehat{\psi}(\mathbf{x}', t) \right\rangle$. Because of hermiticity, it has an eigen-decomposition $\left\langle \widehat{\psi}^\dagger(\mathbf{x}, t) \widehat{\psi}(\mathbf{x}', t) \right\rangle = \sum_{i=0}^{\infty} n_i(t) \phi_i^*(\mathbf{x}, t) \phi_i(\mathbf{x}', t)$ with eigenfunctions $\phi_i(\mathbf{x}, t)$ and occupation numbers n_i. The system is said to be Bose condensed when

there is a single eigenvalue n_i, say $i = 1$, that is of the order of the total atom number. Then, the order parameter is the eigenfunction $\phi_1(\mathbf{x}, t)$.

1.1.2   The Gross-Pitaevskii equation

For ultracold atoms interacting via a short-range atom-atom potential, the two-body collision is dominated by s-wave scattering (when the relative angular momentum of two colliding atoms is zero). Non-zero partial-wave scattering is suppressed by a centrifugal barrier. The strength of s-wave scattering is determined by a single length scale called the scattering length a. In fact, the short-range interatomic potential $V_{2B}(\mathbf{r})$, where $\mathbf{r}$ is the relative position vector, can be approximated by a contact interaction $g\,\delta(\mathbf{r})$. The interaction strength g in three dimensions is related to the scattering length by $g = 4\pi\hbar^2 a/m$, where m is the mass of the atom. The relationship between g and a is different in one or two dimensions.

The many-body Hamiltonian in the contact approximation is

$$H_{\mathrm{MB}} = \int d\mathbf{x} \left[\widehat{\psi}^\dagger(\mathbf{x}, t) \left(-\frac{\hbar^2}{2m}\nabla^2 + V_{\mathrm{ext}}(\mathbf{x}) \right) \widehat{\psi}(\mathbf{x}, t) + \frac{g}{2}\widehat{\psi}^\dagger(\mathbf{x}, t)\widehat{\psi}^\dagger(\mathbf{x}, t)\widehat{\psi}(\mathbf{x}, t)\widehat{\psi}(\mathbf{x}, t) \right],$$

(1.1)

where $V_{\mathrm{ext}}(\mathbf{x})$ is the external single-particle potential. Then, the evolution of the order parameter in a d-dimensional space [1] $\psi(\mathbf{x}, t) = \left\langle \widehat{\psi}(\mathbf{x}, t) \right\rangle$ is given by the

---

[1] Note that in one and two dimensions a translationally-invariant interacting Bose gas with $V_{\mathrm{ext}}(\mathbf{x}) = 0$ does not undergo Bose-Einstein condensation in the thermodynamic limit (length of the system goes to infinity with finite density). This is due to a proliferation of long-wavelength fluctuations. This result is known as the Mermin-Wagner theorem [10, 11].

Gross-Pitaevskii equation (GPE)

$$i\hbar\frac{\partial}{\partial t}\psi(\mathbf{x},t) = -\frac{\hbar^2}{2m}\nabla^2\psi(\mathbf{x},t) + V_{\text{ext}}(\mathbf{x})\psi(\mathbf{x},t) + g|\psi(\mathbf{x},t)|^2\psi(\mathbf{x},t). \qquad (1.2)$$

The GPE can be derived by using the Heisenberg equation of motion for $\widehat{\psi}(\mathbf{x})$, i.e., $i\hbar\partial_t\widehat{\psi}(\mathbf{x},t) = [H_{\text{MB}}, \widehat{\psi}(\mathbf{x},t)]$, where H_{MB} is the many-body Hamiltonian of Eq. 1.1 and $[\widehat{A}, \widehat{B}] = \widehat{A}\widehat{B} - \widehat{B}\widehat{A}$ is the commutator. We then take the expectation value of $\widehat{\psi}(\mathbf{x},t)$ and assume that higher-order moments are reducible to products of first moments, i.e., $\left\langle\widehat{\psi}^\dagger(\mathbf{x}_1,t)\widehat{\psi}^\dagger(\mathbf{x}_2,t)\ldots\widehat{\psi}(\mathbf{x}_n,t)\right\rangle = \left\langle\widehat{\psi}^\dagger(\mathbf{x}_1,t)\right\rangle\left\langle\widehat{\psi}^\dagger(\mathbf{x}_2,t)\right\rangle\ldots\left\langle\widehat{\psi}(\mathbf{x}_n,t)\right\rangle$, to arrive at the GPE.

The GPE is an example of an equation that falls under the umbrella of mean-field approximations. In this context, the mean-field approximation is equivalent to a description of the dynamics of a BEC by a classical Hamiltonian in an infinite-dimensional phase space. The phase space is spanned by the canonical classical fields $X(\mathbf{x}) = \sqrt{\frac{\hbar}{2}}[\psi(\mathbf{x}) + \psi^*(\mathbf{x})]$ and $P(\mathbf{x}) = -i\sqrt{\frac{\hbar}{2}}[\psi(\mathbf{x}) - \psi^*(\mathbf{x})]$. (Note that $\mathbf{x}$ indexes the degrees of freedom and is not a canonical coordinate.) They satisfy the canonical relations $\{X(\mathbf{x}), P(\mathbf{x}')\} = \delta(\mathbf{x} - \mathbf{x}')$, where the Poisson bracket $\{A, B\} = \int d\mathbf{x}\left(\frac{\delta A}{\delta X(\mathbf{x})}\frac{\delta B}{\delta P(\mathbf{x})} - \frac{\delta A}{\delta P(\mathbf{x})}\frac{\delta B}{\delta X(\mathbf{x})}\right)$ and A, B are functionals of $X(\mathbf{x})$ and $P(\mathbf{x})$. The classical Hamiltonian $\mathcal{H}_{\text{MB}}$ is obtained by replacing the continuous, quantum operator field $\widehat{\psi}(\mathbf{x},t)$ in Eq. 1.1 by the classical, c-number field $\psi(\mathbf{x},t)$. From the Hamilton's equations of motion for a phase-space point $X(\mathbf{x},t)$ and $P(\mathbf{x},t)$, we find that $i\hbar\partial_t\psi(\mathbf{x},t) = \delta\mathcal{H}_{\text{MB}}/\delta\psi^*(\mathbf{x},t)$, which yields the GPE. A solution of the GPE $\psi(\mathbf{x},t)$ represents a trajectory in the infinite-dimensional phase space.

One can envision that under certain circumstances, and I study these cases in

Chapter 4, a system can be approximately described by a few modes. We can then write $\widehat{\psi}(\mathbf{x}, t) \approx \sum_{i=1}^{N} \widehat{a}_i(t)\phi_i(\mathbf{x})$, where $\widehat{a}_i(t)$ is the annihilation operator of a mode with wave function $\phi_i(\mathbf{x})$. (For the systems we consider the number of modes N is at most three.) The mean-field approximation entails replacement of the annihilation operators $\widehat{a}_i(t)$ by c-numbers. Furthermore, the mean-field equations of motion are equivalent to Hamilton's equations in a finite-dimensional phase space.

1.1.3   The truncated Wigner approximation

The mean-field approximation for a BEC is equivalent to the motion of a single point in a phase space under the classical Hamilton's equations of motion. In the truncated Wigner approximation, the propagation of a Wigner distribution function, instead of a single phase-space point, is studied. In chapter 4, I study dynamical instability in few-mode systems where the mean-field equations of motion fail and quantum corrections become important. I analytically study the dynamics of systems within the TWA. Even the TWA deviates from the exact quantum dynamics when multiple classical trajectories connecting the start and end points contribute significantly to the propagation of the Wigner function. In chapter 5, I study corrections due to the interference of classical trajectories, which improve upon the TWA.

The phase-space formulation is one of three descriptions of quantum mechanics [12]; the other two being the Hilbert space and the path integral formulations. The equivalency between the Hilbert space and phase space formulations can be

established via the Wigner-Weyl transform, which is a mapping between operators in Hilbert space and functions in phase space. The Wigner function or distribution, a function of phase space coordinates, is the Wigner-Weyl transform of the density matrix. Due to the uncertainty principle, the Wigner function can not be sharply peaked and, thus, has a finite spread. It can, however, be negative. Therefore, it is not a probability but a so-called *quasiprobability* distribution.

Let me make the preceding discussion precise. The relation between the quantum evolution of a Wigner function and classical dynamics is most transparent for the case a single particle in d dimensions. The description for a bosonic system is then a straightforward generalization and is discussed in Chapter 5. The Wigner function for a quantum state with wave function $\psi(\mathbf{x})$ is

$$W(\mathbf{x}, \mathbf{p}) = \frac{1}{(2\pi\hbar)^d} \int d\mathbf{q} \, \psi^* \left(\mathbf{x} - \tfrac{1}{2}\mathbf{q}\right) \psi \left(\mathbf{x} + \tfrac{1}{2}\mathbf{q}\right) e^{-i\mathbf{p}\cdot\mathbf{q}/\hbar}, \qquad (1.3)$$

where positions $\mathbf{x}$ and $\mathbf{q}$ are in $\mathbb{R}^d$. Let the quantum Hamiltonian of the particle be $H_{1\mathrm{p}}(\widehat{\mathbf{x}}, \widehat{\mathbf{p}}) = \widehat{\mathbf{p}}^2/(2m) + V(\widehat{\mathbf{x}})$, where $\widehat{\mathbf{x}} = (\widehat{x}_1, \ldots, \widehat{x}_d)$ and $\widehat{\mathbf{p}} = (\widehat{p}_1, \ldots, \widehat{p}_d)$ are the canonical position and momentum operators that obey $[x_j, p_k] = i\hbar\delta_{jk}$ and m is the mass of the particle. Its Wigner function obeys the time evolution [13]

$$\frac{\partial W(\mathbf{x}, \mathbf{p}, t)}{\partial t} = -\frac{\mathbf{p}}{m} \cdot \frac{\partial W(\mathbf{x}, \mathbf{p}, t)}{\partial \mathbf{x}} + \frac{dV(\mathbf{x})}{d\mathbf{x}} \cdot \frac{\partial W(\mathbf{x}, \mathbf{p}, t)}{\partial \mathbf{p}}$$

$$+ \sum_{n=1}^{\infty} \hbar^n \mathcal{Q}_n(\mathbf{x}, \mathbf{p}), \qquad (1.4)$$

where, for example, $\mathcal{Q}_n(\mathbf{x}, \mathbf{p})$ for $d = 1$ are

$$\mathcal{Q}_n(x, p) = (-1)^n \frac{1}{2^{2n}(2n+1)!} \frac{d^{2n+1}V(x)}{dx^{2n+1}} \frac{\partial^{2n+1}W(x, p)}{\partial p^{2n+1}}. \qquad (1.5)$$

The coefficients $\mathcal{Q}_n(\mathbf{x}, \mathbf{p})$ in higher dimensions are a multinomial generalization of the above expression [12]. The first term on the right-hand side of Eq. 1.4 is the rate of change of the Wigner function due to the particle's momentum and the second term is due to the force experienced by the particle. Finally, the terms with non-zero powers of $\hbar$ are the quantum terms. When these quantum terms are ignored, the evolution of $W(\mathbf{x}, \mathbf{p}, t)$ is in accordance with the Hamilton's equations of motion with a classical Hamiltonian $\mathcal{H}_{1\mathrm{p}} = \mathbf{p}^2/(2m) + V(\mathbf{x})$. This approximation of truncating the evolution equation by ignoring the quantum terms is called the truncated Wigner approximation. Note that, the TWA becomes exact for the case when $V(\mathbf{x})$ is at most quadratic in $\mathbf{x}$. This is the case for a free particle and a particle in a harmonic potential.

1.2   Experimental techniques: Laser cooling and trapping

At atmospheric pressure, a Bose atomic gas will condense to a solid, or in the case of Helium to a liquid, before becoming quantum degenerate. In fact, alkali metals, which were (and still are) used for the creation of ultracold atomic BECs, are solids at room temperature. The way around is to work with a very dilute gas so that the three-body recombination rate, which leads to binding of atoms into molecules, is low. The typical density of an ultracold BEC is 10^{14} cm^{-3}, which implies that the BEC transition temperature is around 100 nK. Reaching such ultracold temperatures required decades of concerted experimental effort and the development of various cooling and trapping techniques. Nevertheless, an ultra-

cold BEC is metastable because of the finite three-body recombination rate. The lifetime, however, is of the order of seconds to minutes, which is typically sufficient to carry out experiments.

Alkali metal atoms are the workhorses for BEC experiments. They are easy to work with as they only have one outer-shell electron, making their spectroscopy simple. Moreover, the relevant atomic transitions are in the range of available lasers. The absence of a suitable laser for spin-polarized hydrogen, which was the initial candidate species for the realization of a BEC, was one of the issues which delayed the creation of its BEC.

We will briefly discuss some of the cooling and trapping techniques used in experiments with BECs. Here, we only discuss the basic principles, for more detailed reviews see [14–16]. Most techniques of cooling neutral atoms are based on the interaction of an atom with light. An atom in its electronic ground state is, in general, almost transparent to monochromatic light of arbitrary frequency. However, it scatters considerably when the light is near resonance with an atomic transition between the ground and an excited state. The excited state has a finite lifetime and decays to the ground state by spontaneous emission of a photon.

When a moving atom encounters a near-resonant counter-propagating laser that is red-detuned from an atomic transition (the laser frequency is less than the frequency of the atomic transition), then due to the Doppler effect the apparent frequency in the atom's frame of reference is blue shifted towards the transition. Then after absorbing a photon, the atom radiates it spontaneously in an arbitrary direction. This leads to a preferential loss of momentum as well as cooling in the

direction of the laser. This mechanism is called Doppler cooling and is used in the Zeeman slower, where a beam of hot atoms coming out of an oven is slowed and cooled down. To keep the laser near resonance as an atom slows down an inhomogeneous magnetic field is applied, which alters the atom transition frequency via the Zeeman effect. Doppler cooling is limited by the fact that the spontaneous emission of photons leads to a random walk of the momentum of an atom. The limiting temperature is $\hbar\Gamma/(2k_B)$, where Γ is the natural line width of the excited state. Using a Zeeman slower the temperature of an alkali gas can be reduced from hundreds of Kelvins to the Doppler cooling limit, which is on the order of millikelvins.

A Zeeman slower cannot spatially trap atoms. Hence, after passing through the slower, atoms are loaded in a magneto-optical trap (MOT). In a MOT, a combination of an inhomogeneous magnetic field and pairs of counter-propagating lasers in three orthogonal directions are used to trap the atoms. The center of the MOT is located where the magnetic field is zero. Now consider one of the pairs of lasers, which have the same frequency and intensity. The polarizations of the lasers are chosen such that the change in the magnetic quantum number of an atom, along the direction of the laser, after it absorbs a photon is ± 1, respectively. At the point where the magnetic field is zero, the forces of the two lasers on the atoms cancel. But as an atom moves away from this point, because of Zeeman effect, the absorption of photons from one of the laser reduces and the other increases. In effect, this leads to a net force towards the zero of the magnetic field, leading to the trapping of atoms.

The temperature of a gas in a MOT is still above the critical temperature. To

attain quantum degeneracy, the atoms are transferred to either a magnetic or an optical dipole trap. In a magnetic trap, an inhomogeneous magnetic field is used for trapping. The interaction energy of an atom in magnetic field $\mathbf{B}$, due to the linear Zeeman effect, is $-\boldsymbol{\mu}.\mathbf{B}$, where the magnetic moment $\boldsymbol{\mu}$ depends on the quantum state. Now a region of space, devoid of electric current, cannot have a maximum in the magnitude of the magnetic field. Thus, atoms can only be trapped in the minima of a magnetic field. Hence, the magnetic moment of the quantum state should be antiparallel to $\mathbf{B}$ and only low-field seeking states can be trapped. Alternatively, atoms are trapped in an optical dipole trap, which consists of focused lasers that are off-resonant and red-detuned to an atomic transition. Due to spatially-dependent AC Stark shift, i.e, the change in energy of a quantum state due to an oscillating electric field, the lasers create an attractive trapping potential.

To lower the temperature of the atoms in a magnetic or optical dipole trap, evaporative cooling is employed. In evaporative cooling, hot atoms that reside near the outer regions of the trap are ejected, and elastic collisions among the remaining atoms reduce the temperature of the trapped gas. In an optical dipole trap, this is done by lowering the depth of the potential. This procedure is difficult to carry out for a magnetic trap, where, instead, a radio-frequency "knife" is used. Because of the Zeeman effect, the transition frequency between the ground and an excited state is position dependent. A radio-frequency field that is resonant with this transition near the edge of the trap selectively flips the spin of an atom, which then escapes from the trap. Finally, after evaporative cooling, the atomic gas becomes cold and dense enough to condense to a BEC.

This brief introduction in no way justifies the complexity and richness of the experiments. Furthermore, the field is ever growing with new emerging techniques and refinement of existing technology.

1.3 Outline of the dissertation

The remainder of the dissertation is organized as follows. In Chapter 2, I study collisions of Bose-Einstein condensates near a Feshbach resonance. The results of this chapter have been published as *"Controlling the group velocity of colliding atomic Bose-Einstein condensates with Feshbach resonances"* in Physical Review A (PRA) [17]. In chapter 3, I describe my theoretical analysis of interferometric measurement in an atomic-SQUID. It is based on the paper *"Self-heterodyne detection of the in situ phase of an atomic superconducting quantum interference device"* published in PRA [18]. In chapter 4, based on the paper *"Phase-space mixing in dynamically unstable, integrable few-mode quantum systems"* published in PRA [19], I study dynamical instability in few-mode systems using the TWA. In the next chapter, I study corrections beyond the TWA. A paper based on its results is under preparation. Finally, I conclude in chapter 6.

Chapter 2:   Collision of Bose-Einstein condensates near a Feshbach resonance

2.1   Introduction

Over the last two decades, significant advances have been made to replicate linear and nonlinear optical phenomena with matter waves, creating the field of matter-wave optics. For example, atom lasers [4,5] are sources of coherent ultracold atoms generated by extracting atoms from a Bose-Einstein condensate (BEC). The coherence of BECs was demonstrated by interfering two condensates [20]. Atomic mirrors and beam splitters have also been realized [6]. Recently, the matter-wave equivalent of meta-materials (media with negative refractive index) has been proposed [21]. The analog of nonlinear four-wave mixing has been demonstrated using atom lasers [22,23]. In these experiments, three BECs with phase-matched relative momenta generated a fourth beam.

In this chapter, we present a proposal to slow a BEC while propagating through another BEC near a magnetic Feshbach resonance in analogy to slowing of light in dispersive media. Slowing of light occurs when the refractive index of a medium varies sharply with photon frequency. Using electromagnetically induced trans-

parency [24], slow light has been observed with a Bose-Einstein condensate [25, 26] and a hot Rb gas [27] acting as the medium.

Magnetic Feshbach resonances are a tool with which to manipulate the interaction between ultracold atoms [28]. They are used for creating ultracold molecules, molecular condensates, and in the BEC-BCS crossover in Fermi gases [29, 30]. Feshbach resonances play an essential role in condensing ^{133}Cs, ^{85}Rb, and ^{39}K [31–33]. Cooling ultracold atoms using Feshbach resonances has been proposed [34]. Collisions can also be tuned using optical Feshbach resonances [35–37], as their width can be dynamically varied with a laser. However, they tend to suffer from losses due to spontaneous emission.

The chapter is organized as follows. We first review the two-body physics of a Feshbach resonance in Sec. 2.2. Subsequently, in Sec. 2.3, we derive a generalized Gross-Pitaevskii equation (GPE) to describe the collision of two BECs. Then, in Sec. 2.4, we consider an experimental setup of a small BEC, called a laser BEC, traveling through a larger "medium" BEC. The names are chosen to draw analogy to a laser pulse travelling through the medium. We analyze this experimental proposal using the generalized GPE and derive the group velocity in a homogeneous medium. Then, we consider an inhomogeneous medium and estimate δ, i.e., the difference in distance traveled by the laser BEC in the presence and absence of an inhomogeneous medium. Finally, restrictions on an experimental realization are given.

2.2 Feshbach resonance

Collisions between ultracold atoms are dominated by s-wave scattering. The scattering amplitude $f(E)$ only depends on the relative collision energy, $E = \hbar^2 k^2/(2\mu)$, where k is the magnitude of the relative wave vector and μ is the reduced mass. Then, around an isolated magnetic Feshbach resonance [28, 38, 39]

$$f(E) = f_{\text{bg}}(E) - e^{2i\delta_{\text{bg}}} \frac{\hbar\Gamma(E)/(2k)}{E - E_{\text{res}} + i\hbar\Gamma(E)/2} . \tag{2.1}$$

The background scattering amplitude $f_{\text{bg}}(E) = e^{i\delta_{\text{bg}}} \sin(\delta_{\text{bg}})/k$, with phase shift δ_{bg}. To a good approximation, $f_{\text{bg}}(E) = -a_{\text{bg}}/(1 + ika_{\text{bg}})$, and $\delta_{\text{bg}} = -ka_{\text{bg}}$, where a_{bg} is the background scattering length. The resonance width $\Gamma(E) = 2ka_{\text{bg}}\Gamma_0$ in the threshold limit $k \to 0$. The energy-independent reduced width $\Gamma_0 = \mu_{\text{res}}\Delta/\hbar$, where μ_{res} is the difference between the magnetic moments of the resonance state and the asymptotically free atoms, and Δ is the magnetic width of the resonance. The resonance energy is $E_{\text{res}} = \mu_{\text{res}}(B - B_0)$, where B is the magnetic field and B_0 is the resonant field. The scattering amplitude $f(E)$ satisfies the optical theorem [38].

Figure 2.1 shows $f(E)$ near a Feshbach resonance as a function of collision energy E. The resonance occurs at a finite collision energy and $f(E)$ approaches $f_{\text{bg}}(E)$ away from E_{res}. The imaginary part of $f(E)$ is related to the total cross section $\sigma(E)$ and thus to the fraction of scattered atoms. In fact, $\sigma(E) = 4\pi \operatorname{Im} f(E)/k$ from the optical theorem [38]. On resonance, $\operatorname{Im}(f)$ is maximal and $\approx 1/k$. More importantly, there exists a collision energy at which $f(E) = 0$ due to an interference between the background and resonance scattering amplitudes. We call this collision
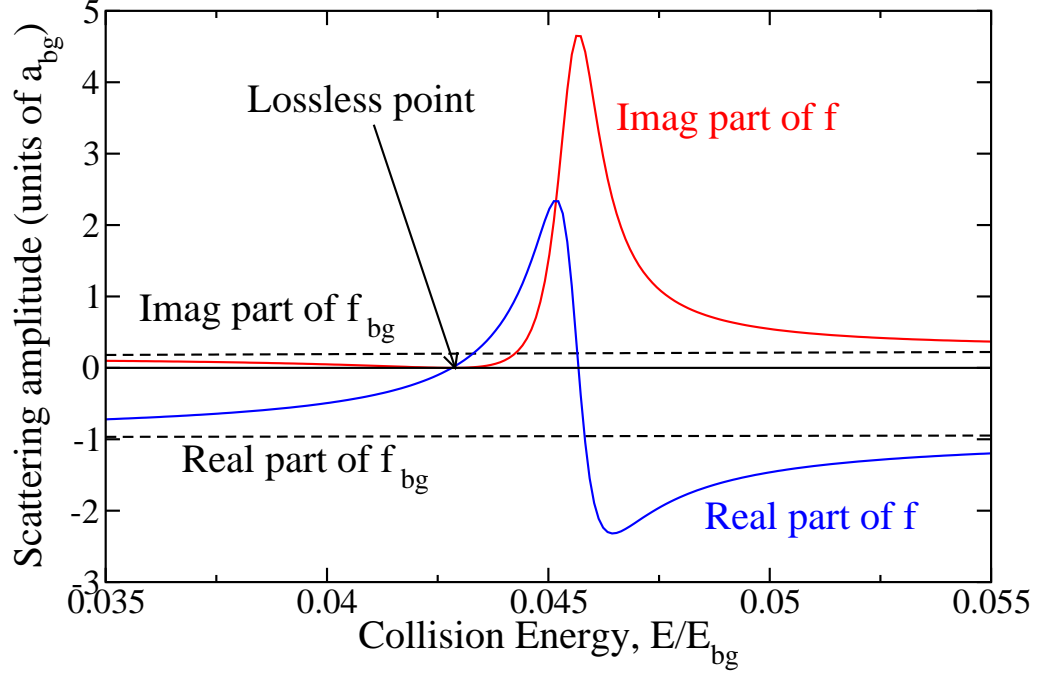
Figure 2.1: (Color online) Real and imaginary part of scattering amplitudes f and f_{bg} as a function of collision energy for a narrow Feshbach resonance. The x and y axes are scaled by the Wigner-threshold limit $E_{bg} = \hbar^2/(2\mu a_{bg}^2)$ and the background scattering length a_{bg}, respectively. Also shown is the lossless point where $f(E) = 0$. energy the *lossless point*, which to good approximation is $E_{res} - \hbar\Gamma_0$ for positive a_{bg}.

2.3 Collision of two BECs

We now describe the many-body physics of colliding BECs. We assume that the BECs contain the same atomic species and the relative velocity is much larger than the speed of sound in both condensates; hence, we can ignore collective excitations. The dynamics of the BECs is well described by the time evolution of the order parameter $\Psi(\mathbf{x}, t)$, i.e., the expectation value of the annihilation operator

$\hat{\Psi}(\mathbf{x}, t)$ in the Heisenberg picture. For a BEC at rest, its evolution is well described by the Gross-Pitaevskii equation (GPE), derived for an energy-independent and real scattering amplitude. Both assumptions are invalid near a Feshbach resonance at finite energy.

Our starting point is Eq. 38 of Ref. [40], obtained using a cumulant expansion. The equation includes the time and energy dependence of the two-body scattering and is

$$i\hbar\frac{\partial}{\partial t}\Psi(\mathbf{x}, t) = H_{1\mathrm{B}}\Psi(\mathbf{x}, t) + \int \prod_i d\mathbf{y}_i \int_{t_0}^{\infty} dt_1 \Psi(\mathbf{y}_1, t_1)\Psi(\mathbf{y}_2, t_1)\Psi^*(\mathbf{y}_3, t) \quad (2.2)$$

$$\times \langle \mathbf{x}, \mathbf{y}_3 | T_{2\mathrm{B}}(t, t_1) | \mathbf{y}_1, \mathbf{y}_2 \rangle ,$$

where t_0 is the initial time, $t > t_0$, $H_{1\mathrm{B}} = -\hbar^2 \nabla^2/(2m) + V(\mathbf{x})$ is the single-particle Hamiltonian, m is the atomic mass and $V(\mathbf{x})$ is the external potential. The operator $T_{2\mathrm{B}}$ is the two-body T matrix in the time domain and the integrals over $\mathbf{y}_i$, $i \in \{1, 2, 3\}$, are in coordinate space. Equation 2.2 was originally derived for single-channel scattering, but remains valid for multichannel resonances following Ref. [41], assuming that the order parameter of the molecular channel vanishes.

We call the two condensates a laser and a medium BEC in anticipation of the experimental proposal described in Sec. 2.4. The initial momentum distribution of the two BECs are nonoverlapping and we assume that they remain so when the BECs pass through each other. Hence, the wave function $\Psi(\mathbf{x}, t)$ is the sum of orthogonal wave functions of the laser and medium BECs, $\Psi_{\mathrm{L}}(\mathbf{x}, t)$ and $\Psi_{\mathrm{M}}(\mathbf{x}, t)$, respectively. Substituting the sum in Eq. 2.2 and keeping only the phase-matched

18

terms, we find the following equation for the laser BEC

$$i\hbar\frac{\partial}{\partial t}\Psi_{\mathrm{L}}(\mathbf{x},t) = \mathcal{L}_{\mathrm{L}}\Psi_{\mathrm{L}}(\mathbf{x},t) + 2\int\prod_i d\mathbf{y}_i\,\Psi_{\mathrm{M}}^*(\mathbf{y}_3,t)\int_{t_0}^{\infty}dt_1\,\langle\mathbf{x},\mathbf{y}_3|\,T_{2\mathrm{B}}\,(t,t_1)\,|\mathbf{y}_1,\mathbf{y}_2\rangle$$

$$\times\,\Psi_{\mathrm{L}}(\mathbf{y}_1,t_1)\Psi_{\mathrm{M}}(\mathbf{y}_2,t_1)\,,\tag{2.3}$$

where $\mathcal{L}_{\mathrm{L}} = H_{1\mathrm{B}} + g|\Psi_{\mathrm{L}}(\mathbf{x},t)|^2$ and g is the interaction strength of the laser BEC.
The second term on the right-hand side is nonlocal in both space and time. Without
this term, Eq. 2.3 reduces to the GPE. Note that, an equation similar to Eq. 2.3
holds for $\Psi_{\mathrm{M}}(\mathbf{x},t)$.

We approximate the integrands in Eq. 2.3 by power series in derivatives eval-
uated at $\mathbf{x}$ and t. First, we realize that $T_{2\mathrm{B}}(t,t_1)$ only depends on $t - t_1$ and
is peaked around $t - t_1 = 0$. (That is, the time scale of two-body scattering is
much shorter than the time scale of collision between the two BECs.) Assum-
ing that the wave functions vary slowly in time, the lower limit of the integral
over time can be extended to $-\infty$. Next, we note that $\int_{-\infty}^{\infty}d\tau h(\tau)g(t-\tau) =$
$\tilde{h}\left(i\partial/\partial t\right)g(t)$, where $\tilde{h}(z) = \int_{-\infty}^{\infty}dt\,e^{izt}h(t)$ is the Fourier transform of $h(t)$ and
$\tilde{h}(i\partial/\partial t) = \sum_n d^n\tilde{h}/dz^n\,|_{z=0}\,(i\partial/\partial t)^n/n!$. Then, with $h(\tau) = \langle.|\,T_{2\mathrm{B}}\,(\tau)\,|.\rangle$, the
second term on the right-hand side of Eq. 2.3 reduces to

$$2\int\prod_i d\mathbf{y}_i\,\Psi_{\mathrm{M}}^*(\mathbf{y}_3,t)\left\langle\mathbf{x},\mathbf{y}_3\middle|\,T_{2\mathrm{B}}\left(i\hbar\frac{\partial}{\partial t}\right)\middle|\mathbf{y}_1,\mathbf{y}_2\right\rangle\Psi_{\mathrm{L}}(\mathbf{y}_1,t)\Psi_{\mathrm{M}}(\mathbf{y}_2,t)\,,\tag{2.4}$$

where the T matrix $T_{2\mathrm{B}}(z)$ is now in the energy domain (dropping the $\sim$ superscript
for simplicity) and the time derivatives only act on $\Psi_{\mathrm{L}}(\mathbf{y}_1,t)\Psi_{\mathrm{M}}(\mathbf{y}_2,t)$.

The T matrix in coordinate space can be evaluated by transforming to the
momentum representation. For s-wave scattering, the dependence on the relative

19

momenta can be neglected. That is, to a good approximation, the T matrix in momentum representation is [40]

$$\langle \mathbf{k}_4, \mathbf{k}_3 | T_{2\mathrm{B}}(z) | \mathbf{k}_1, \mathbf{k}_2 \rangle = -\frac{\hbar^2}{4\pi^2 \mu} f\left(z - \frac{\hbar^2}{2M}(\mathbf{k}_1 + \mathbf{k}_2)^2\right) \delta(\mathbf{k}_4 + \mathbf{k}_3 - \mathbf{k}_2 - \mathbf{k}_1), \quad (2.5)$$

where the δ function reflects total momentum conservation, $f(E)$ is the scattering amplitude, and $M = 2m$. Near a Feshbach resonance, $f(E)$ is given by Eq. 2.1.

We insert the momentum representation of $T_{2\mathrm{B}}$ into Eq. 2.4 and note that the Taylor expansion of $\phi(\mathbf{y}, t)$ around position $\mathbf{x}$ can be formally written as $\phi(\mathbf{y}, t) = \exp[-i(\mathbf{y} - \mathbf{x}) \cdot i\nabla] \phi(\mathbf{x}, t)$. Then, the interaction term of Eq. 2.4 becomes

$$\frac{2}{(2\pi)^6} \left(-\frac{\hbar^2}{4\pi^2 \mu}\right) \iint \prod_{i,j} d\mathbf{y}_i d\mathbf{k}_j \, \delta(\mathbf{k}_4 + \mathbf{k}_3 - \mathbf{k}_2 - \mathbf{k}_1) \Psi_{\mathrm{M}}^*(\mathbf{y}_3, t) e^{i\mathcal{Q}}$$

$$\times f\left(i\hbar \frac{\partial}{\partial t} - \frac{\hbar^2}{2M}(\mathbf{k}_1 + \mathbf{k}_2)^2\right) \left[e^{-i(\mathbf{y}_1 - \mathbf{x}) \cdot i\nabla} \Psi_{\mathrm{L}}(\mathbf{x}, t)\right] \left[e^{-i(\mathbf{y}_2 - \mathbf{x}) \cdot i\nabla} \Psi_{\mathrm{M}}(\mathbf{x}, t)\right], \quad (2.6)$$

where $\mathcal{Q} = \mathbf{k}_4 \cdot \mathbf{x} + \mathbf{k}_3 \cdot \mathbf{y}_3 - \mathbf{k}_2 \cdot \mathbf{y}_2 - \mathbf{k}_1 \cdot \mathbf{y}_1$. Performing all integrations, we find

$$i\hbar \frac{\partial}{\partial t} \Psi_{\mathrm{L}}(\mathbf{x}, t) = \mathcal{L}_{\mathrm{L}} \Psi_{\mathrm{L}}(\mathbf{x}, t) - \frac{4\pi \hbar^2}{\mu} \Psi_{\mathrm{M}}^*(\mathbf{x}, t) f\left(i\hbar \frac{\partial}{\partial t} + \frac{\hbar^2}{2M} \nabla^2\right) \Psi_{\mathrm{L}}(\mathbf{x}, t) \Psi_{\mathrm{M}}(\mathbf{x}, t),$$

$$(2.7)$$

where, formally, $f(\hat{\mathcal{O}}) = \sum_{n=0}^{\infty} \frac{(\hat{\mathcal{O}} - x_0)^n}{n!} \frac{d^n f}{dx^n}\big|_{x=x_0}$ is the Taylor series of function $f(x)$ about a point x_0 and $\hat{\mathcal{O}}$ is an operator. Finally, the medium condensate obeys an equation similar to Eq. 2.7.

2.4 Experimental setup

We now present a proposal of slowing a condensate traveling through a large stationary BEC near a magnetic Feshbach resonance. Figure 2.2 shows a schematic
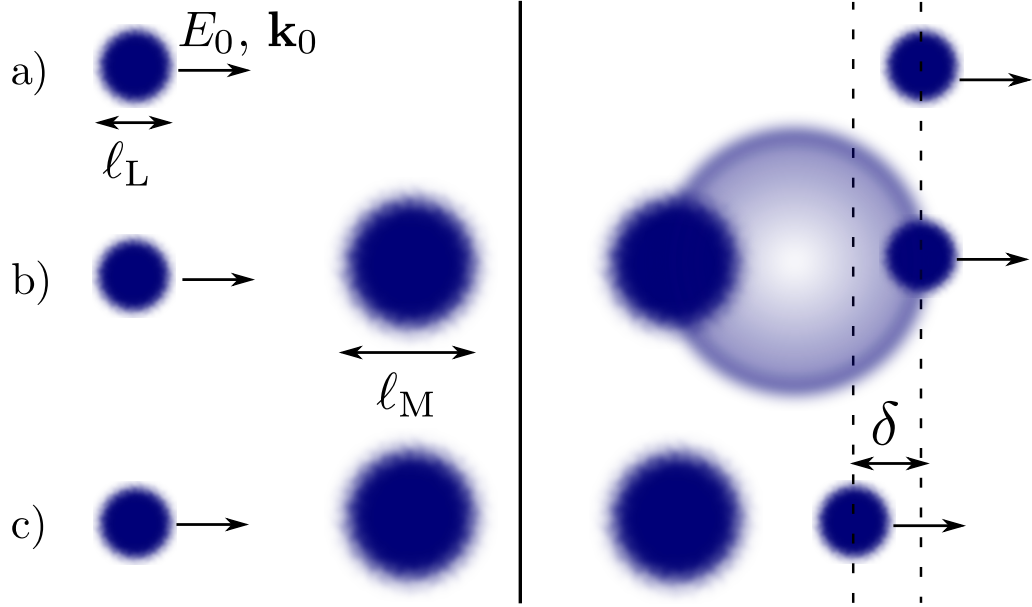
Figure 2.2: A schematic of a slow-atom experiment with colliding condensates. The left- and right-hand sides show images of the condensates before and after the collision, respectively. (a) The laser BEC moving in free space with kinetic energy E_0 and wave vector $\mathbf{k}_0$. (b), (c) Two cases of a laser BEC propagating through the medium BEC. (b) A case with large elastic-scattering losses indicated by the halo of scattered atoms. (c) The collision near a Feshbach resonance where there is negligible scattering loss. This occurs when the scattering amplitude is zero. The distance delay δ of the laser BEC is also indicated.

of this proposal. The laser BEC has a length ℓ_L and propagates with wave vector $\mathbf{k}_0$ of magnitude $k_0 \gg 1/\ell_L$. Its average velocity is $\mathbf{v}_0 = \hbar\mathbf{k}_0/m$ and the kinetic energy per particle is $E_0 = \hbar^2 k_0^2/(2m)$. It is incident on a stationary BEC of size ℓ_M, such that $\ell_L \ll \ell_M$ (in all spatial directions). Figures 2.2(b) and (c) show two distinct cases of collisions between condensates. In Fig. 2.2(b), elastic scattering out of the two condensates is significant. These losses have limited BEC collisions [42, 43] and four-wave mixing experiments [44, 45]. On the other hand, it allows detection of d-wave-shaped resonances in collisions between BECs [46] and thermal gases [47]. In Fig. 2.2(c), after carefully tuning the resonance energy, the collision occurs at the lossless point, which we defined in Sec. 2.2. The laser BEC then slows down.

We now apply the theory developed in Sec. 2.3 to our proposal. Since $\ell_L \ll \ell_M$ and the spread in the collision energy is much smaller than $\Gamma(E_0/2)$, it is sufficient to expand $f(z)$ in Eq. 2.7 to first order around $z = E_0/2$, i.e., the average relative collision energy, and the derivative of $\Psi_M(\mathbf{x}, t)$ can be neglected. The time evolution of the laser condensate is then given by

$$i\hbar \frac{\partial}{\partial t} \Psi_L(\mathbf{x}, t) = \left[-\frac{\hbar^2}{2m^*(\mathbf{x})} \nabla^2 + V_{\mathrm{mf}}(\mathbf{x}) + V_{\mathrm{deriv}}(\mathbf{x}) \right] \Psi_L(\mathbf{x}, t), \qquad (2.8)$$

where $m^*(\mathbf{x}) = m[1 + 2\alpha(\mathbf{x})]/[1 + \alpha(\mathbf{x})]$ is the position-dependent effective mass and

$$\alpha(\mathbf{x}) = \frac{4\pi\hbar^2}{m} |\Psi_M(\mathbf{x})|^2 \left. \frac{df(z)}{dz} \right|_{z=E_0/2}. \qquad (2.9)$$

The "mean-field" potential

$$V_{\mathrm{mf}}(\mathbf{x}) = \frac{V(\mathbf{x}) - (8\pi\hbar^2/m)|\Psi_M(\mathbf{x})|^2 f(E_0/2)}{1 + 2\alpha(\mathbf{x})}, \qquad (2.10)$$

which contains the external potential and a potential proportional to the scattering

22
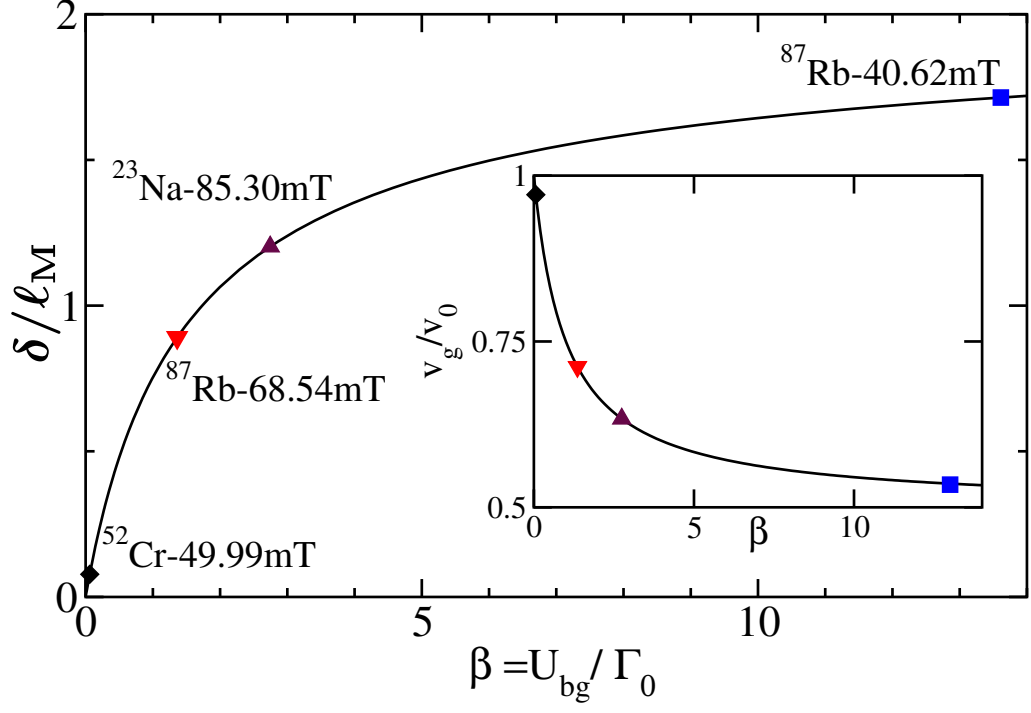
Figure 2.3: (Color online) Distance delay δ of the laser BEC normalized by the Thomas-Fermi radius ℓ_M of the medium BEC as a function of dimensionless parameter $\beta = U_{bg}/(\hbar\Gamma_0)$, where U_{bg} and Γ_0 are defined in the text. The delay for selected resonances assuming a peak number density of the medium of $n_M = 10^{15}\,\mathrm{cm}^{-3}$ is shown by colored markers. The inset shows the group velocity v_g of the laser BEC in a homogeneous medium BEC as a function of β. Here, v_0 is the free space velocity of the laser BEC. Markers indicate v_g for the same selected resonances and n_M as in the main figure.

amplitude and medium density. The latter contribution is analogous to the interaction potential in the GPE, except that the scattering amplitude is evaluated at $E_0/2$. Finally, the potential $V_{\mathrm{deriv}}(\mathbf{x}) = E_0\alpha(\mathbf{x})/[1 + 2\alpha(\mathbf{x})]$. The factor $1 + 2\alpha(\mathbf{x})$, appearing throughout, results from the $i\hbar\partial/\partial t$ argument of the scattering amplitude.

The operator acting on $\Psi_{\mathrm{L}}(\mathbf{x})$ on the right-hand side of Eq. 2.8 is not Hermitian as the scattering amplitude is complex valued. In fact, the non-Hermiticity leads to atom loss, shown in Fig. 2.2(b) as the halo. For a medium number density n_{M}, the loss rate out of the laser condensate is $n_{\mathrm{M}}v_0\sigma$. Consequently, at resonance, where $\sigma \approx 8\pi/(k_0/2)^2$, the fraction of atoms remaining in the laser condensate after the collision is $\approx \exp\left(-8\pi n_{\mathrm{M}}\ell_{\mathrm{M}}/(k_0/2)^2\right)$. For typical values of n_{M} and ℓ_{M}, almost all of the laser atoms are lost at resonance.

For our proposal, we need to minimize these losses. We can use the lossless point where $f(z) = 0$, indicated in Fig. 2.1, and the total cross section is zero. The effective mass and the potentials in Eq. 2.8 are then real, with $m^*(\mathbf{x}) > m$. Moreover, $df/dz = a_{\mathrm{bg}}/(\hbar\Gamma_0)$ and is always positive from the definition of $\Gamma(E)$.

At the lossless point, the simplest case to analyze is that of a homogeneous medium and $V(\mathbf{x}) = 0$. The potential $V_{\mathrm{mf}}(\mathbf{x})$ vanishes and the effective mass is uniform as well as real. Transforming Eq. 2.8 to momentum space, we find that the propagation or group velocity of the laser BEC is

$$\mathbf{v}_{\mathrm{g}}(\mathbf{k}_0)\Big|_{\mathrm{lossless}} = \frac{\hbar\mathbf{k}_0}{m^*} = \mathbf{v}_0\left[\frac{1 + \beta/2}{1 + \beta}\right], \tag{2.11}$$

where the dimensionless quantity $\beta = U_{\mathrm{bg}}/(\hbar\Gamma_0) > 0$ and $U_{\mathrm{bg}} = (8\pi\hbar^2/m)a_{\mathrm{bg}}n_{\mathrm{M}}$ is the background mean-field interaction energy. The inset of Fig. 2.3 shows the

24

group velocity as a function of β. As $\beta > 0$, the group velocity must decrease and approaches $\mathbf{v}_0/2$ when $\beta \to \infty$.

We now turn to propagation through an inhomogeneous medium, but still with $V(\mathbf{x}) = 0$. The assumption $\ell_{\mathrm{L}} \ll \ell_{\mathrm{M}}$ implies that the density variation of the medium orthogonal to the laser propagation direction is negligible and we only need to treat propagation along $\mathbf{k}_0$ passing through the center of the medium BEC.

For simplicity, the density profile of the untrapped medium is given by $|\Psi_{\mathrm{M}}(\mathbf{x})|^2 = n_{\mathrm{M}}(1 - x^2/\ell_{\mathrm{M}}^2)$, using the Thomas-Fermi approximation and neglecting the expansion of the medium. Here, n_{M} is the peak number density and ℓ_{M} is the Thomas-Fermi radius of the medium. It is worth noting that the condensates are stable as the scattering length at zero collision energy is positive. For relative collision energies close to $E_0/2$, the local de Broglie wavelength of the laser changes slowly over the medium condensate. In fact, at the lossless point, Eq. 2.8 reduces to free particle evolution. Hence, we can apply the Wentzel-Kramers-Brillouin (WKB) approximation to estimate δ. We find

$$\frac{\delta}{\ell_{\mathrm{M}}} = 2 \left(1 - \frac{\operatorname{arctanh}\left(\sqrt{\beta/(1+\beta)} \right)}{\sqrt{\beta(1+\beta)}} \right) , \tag{2.12}$$

and the dimensionless quantity $\beta = U_{\mathrm{bg}}/(\hbar\Gamma_0)$ is evaluated at the peak number density n_{M}. Figure 2.3 shows δ as a function of β. The maximum δ that can be attained by the laser is $2\ell_{\mathrm{M}}$ for $\beta \to \infty$.

There are several constraints on the realization of the proposal. First, we have $\ell_{\mathrm{L}} \ll \ell_{\mathrm{M}}$. Second, scattering is s-wave dominated, so that $k_0 a_{\mathrm{bg}} \ll 1$ or $E_0/2 \ll \hbar^2/(2\mu a_{\mathrm{bg}}^2) \equiv E_{\mathrm{bg}}$, i.e, the Wigner threshold limit. Third, by solving for

Im $f(z) = 0$ for positive a_{bg}, we find that the requirement $E_{\mathrm{res}} > \hbar\Gamma_0$ must hold. Fourth, the energy window around the lossless point, where Im f is small, is on the order of $\hbar\Gamma(E_{\mathrm{res}})$. Consequently, the spread in collision energy, $\Delta E_0 \approx \hbar^2 k_0/(2m\ell_{\mathrm{L}})$, must satisfy $\Delta E_0 \ll \hbar\Gamma(E_{\mathrm{res}})$. In other words, $\ell_{\mathrm{L}} \gg \hbar/(ma_{\mathrm{bg}}\Gamma_0) \equiv \ell_{\mathrm{L}}^{\mathrm{min}}$. Finally, we require resonances for which δ is comparable or larger than the size of the laser BEC. Since $\ell_{\mathrm{L}} \ll \ell_{\mathrm{M}}$, we have β is at least of the order of one.

Table 2.1 gives a non-exhaustive list of narrow resonances, which satisfy the constraints. For four of these resonances, the expected δ is shown in Fig. 2.3 assuming a peak density of $n_{\mathrm{M}} = 10^{15}$ cm^{-3}. If we assume $\ell_{\mathrm{L}}/\ell_{\mathrm{M}} \approx 0.1$, then δ ranges from $0.1\ell_{\mathrm{L}}$ to $20\ell_{\mathrm{L}}$ for the resonances in Table 2.1. For the selected density, the chromium resonance is only a marginal candidate for the experiments.

2.5   Conclusion

In conclusion, we have shown that magnetic Feshbach resonances can lead to slowing of a BEC as it propagates through a large medium BEC. The slowing is a consequence of the collision-energy dependence of the scattering amplitude near the resonance. Based on a generalized Gross-Pitaevskii equation, we predict a maximal reduction of the group velocity by a factor of two and suggest that the experiment be performed at a magnetic field where elastic scattering is zero. Such a field always exists near a Feshbach resonance. For finite-sized condensates, slowing can be observed by measuring the spatial delay of the laser BEC, and for narrow resonances, this signal is expected to be measurable.

Table 2.1: Resonance parameters, experimental constraints, and spatial delay for nine Feshbach resonances. The first five columns specify the Feshbach resonance. The columns are the atomic species, magnetic resonance position B_0, magnetic width Δ, reduced width Γ_0, and Wigner-threshold limit E_{bg}. The sixth column gives the minimum size ℓ_L^{min} of the laser BEC. The last column is the shift δ in units of the radius of the medium ℓ_M, assuming a peak medium density of $n_M = 10^{15}$ cm^{-3}. Parameters obtained from [28].

Atom	B_0	Δ	$\hbar\Gamma_0/k_B$	E_{bg}/k_B	ℓ_L^{min}	δ/ℓ_M
	(mT)	(mT)	(μK)	(μK)	(μm)	
^{23}Na	119.5	-0.14	14	1900	0.45	0.15
''	90.7	0.10	260	1900	0.025	0.0091
''	85.3	2.5×10^{-4}	0.64	1900	9.8	1.20
^{87}Rb	100.74	0.021	39	200	0.027	0.025
''	91.17	1.3×10^{-4}	0.24	200	4.4	1.25
''	68.54	6×10^{-4}	0.54	200	1.9	0.89
''	40.62	4×10^{-5}	0.054	200	19	1.7
''	0.913	1.5×10^{-3}	2.0	200	0.52	0.38
^{52}Cr	49.99	0.008	22	290	0.076	0.078

Chapter 3: Interferometric measurement of current-phase relationship of an atomic SQUID

3.1 Introduction

Atomtronics focuses on the creation of atomic analogs to electronic devices. Analogs to several electronic components, such as diodes and transistors, have been proposed [48], while several other circuit elements have been experimentally realized, including capacitors [49, 50] and spin transistors [51]. The atomic version of the rf-superconducting quantum interference device (SQUID) has been realized [52–54], and initial experiments towards the creation of a dc-SQUID have been performed [55, 56]. Both SQUID devices are formed using a toroidal Bose-Einstein condensate and contain one or more rotating weak links or barriers. Furthermore, creation of an atomic rf-SQUID in a ring-shaped lattice has been proposed [57, 58]. Theoretically persistent current states in (quasi-)one-dimensional toroidal geometry have been studied extensively [59–62]. Weak links, whether superconducting or atomic, are characterized by the relationship between the current through and the phase across the barrier [63]. Accurate measurement of this current-phase relationship in the atomic system is crucial for the characterization of atomtronic devices.

Measurement of the *in situ* phase of a condensate through interference is a common tool in modern cold-atom physics. Since the first interference between three-dimensional condensates was demonstrated in 1997 [64,65], several experiments have used interference to infer details about the *in situ* phase profile of condensates [66]. Vortices in condensates [67] and fluctuations brought on by the two-dimensional Berezinskii-Kosterlitz-Thouless phase transition [68] have also been detected interferometrically. Interference between two molecular BECs [69] and BECs on an atom chip have also been observed [70]. Recently, interference measurements have been extended to determine the persistent current state in a toroidal condensate [71,72]. Eckel *et al.* [72] also measured the current-phase relationship of a BEC in a toroidal trap with a rotating barrier, the atomic analog of an rf-SQUID.

In the experiment of Ref. [72], a single condensate was created in a simply connected trap and subsequently split into two condensates. One condensate was confined in a toroidally shaped "science" trap and the other condensate was confined in a concentric disk-shaped "reference" trap. We refer to these together as the "target" trap. A schematic and an *in situ* image of atoms in a target trap are shown Fig. 3.1. The science and reference traps were separated by more than 5 μm; thus atom tunneling between them is negligible and the condensates dephase rapidly because of imperfections in the splitting procedure. Hence, when the two condensates expand and interfere after turning off all trapping potentials, their relative phase is random, thus representing a self-heterodyne measurement [73]. Rotating weak links are only applied to the condensate in the science trap and the other condensate is a phase reference. The current through and the phase drop across the barrier were
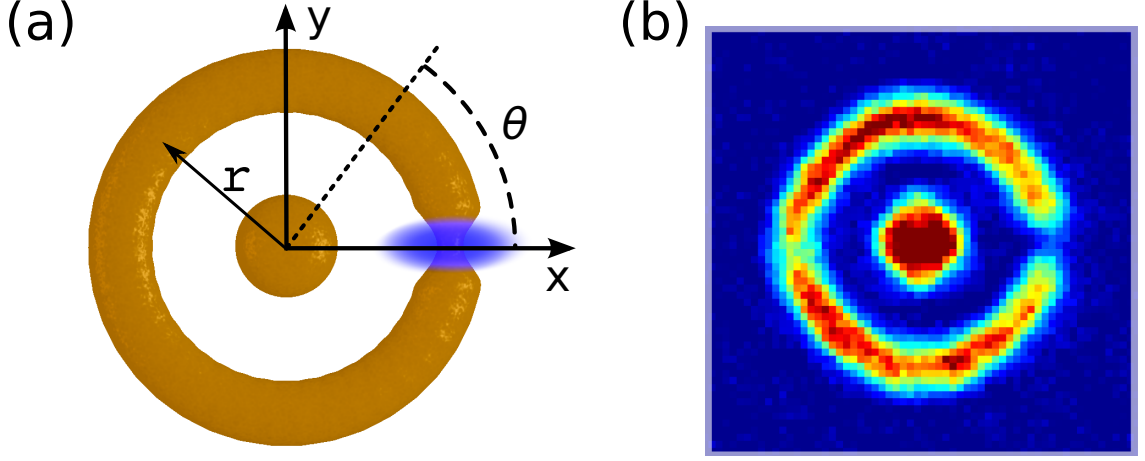
Figure 3.1: (Color online) (a) A schematic of atoms in a target trap. The inner disk and the outer ring are the reference and science condensates, respectively. A blue-detuned laser forms a rotating weak link and is shown by the blue (gray) ellipse. (b) An *in situ* image from the experiment of atoms in a target trap.

inferred from the spiral-shaped modulation in the density profile for short expansion times. The number of spiral arms determines the winding number of the persistent current state, while their chirality determines the direction of atom flow.

In this chapter, we study in detail the interference patterns that result from interfering a toroidal condensate with a reference condensate and verify the interferometric technique used in Ref. [72] to measure the current-phase relationship. We first analytically and numerically study a single-particle version of the atomic rf-SQUID in Sec. 3.2. We find that the experimentally observed spirals are a short time phenomenon and both the current through and the phase drop across the barrier follow from the geometry of the spirals. For longer expansion times, the spirals become modulated with concentric circles due to self-interference of the torus and

it becomes difficult to read out the *in situ* phase drop. In Sec. 3.3, we describe details of the experiments with sodium condensates in a target trap. In addition, this section describes the numerical techniques used to simulate the mean-field Gross-Pitaevskii equation, which quantifies the effects of atom-atom interactions on the expanding condensates. Estimates of bounds on expansion times, where spirals can be observed in the density profile, are also derived. Finally, in Sec. 3.4, a comparison of theoretical and experimental results validates the interferometric method for measurement of the current-phase relationship of an atom-SQUID.

3.2 Single-particle picture

We begin our study of the interference by deriving analytic expressions for the free expansion of a single atom of mass m released from a target-trap interferometer and give an intuitive explanation of the origin of the spirals in the interference pattern. To generate the interference, we assume that the wave function of our single particle is in a superposition of a wave localized in the reference and science regions, respectively.

3.2.1 Particle in a rotating torus

In order to solve for the wave functions, we first describe the target trap in cylindrical coordinates $\vec{x} = (r, \theta, z)$. The science and reference traps are assumed to be parabolic in the radial direction, and centered at r_S and the origin, respectively [see Fig. 3.1(a)]. The harmonic oscillator lengths are σ_S and σ_R, respectively. The

common transverse confinement is harmonic with oscillator length ℓ_z. We assume $\sigma_R \approx \sigma_S$ and $\sigma_S, \sigma_R, \ell_z \ll r_S$. In addition, the science trap has a barrier or weak link rotating at angular frequency Ω inducing atom flow. For simplicity, we model the barrier in the science trap as a Dirac delta function $V_b(\vec{x}, t) = U_0 w(r) \delta(\theta - \Omega t)$, with strength U_0, time t, and $w(r)$ being a window function which is 1 around the radial position of the science trap and 0 everywhere else.

In the frame rotating with the barrier, the atom is prepared in the time-independent state $\Psi_{\text{init}}(\vec{x}) = (\psi_R(\vec{x}) + \psi_S(\vec{x}))/\sqrt{2}$, where the $\psi_i(\vec{x}) = \eta_i(r)\varphi_i(\theta)\phi_z(z)$ are separable wave functions of the science $(i = S)$ and reference $(i = R)$ traps. Here, $\phi_z(z)$ is the unit-normalized 1D ground-state harmonic-oscillator wave function and $\eta_i(r) = e^{-(r-r_i)^2/(2\sigma_i^2)}/\mathcal{N}$ is the radial wave function, where $\mathcal{N}$ is a normalization constant. The overlap between the $\psi_i(\vec{x})$ is negligible.

The angular functions $\varphi_i(\theta)$ are $1/\sqrt{2\pi}$ for the reference trap and the ground state of the Schrödinger equation

$$\left[-\frac{d^2}{d\theta^2} + 2i\kappa\frac{d}{d\theta} + U\delta(\theta) \right] \varphi_S(\theta) = E\varphi_S(\theta) \tag{3.1}$$

for the toroidal trap with a rotating barrier. Here, $\kappa = \Omega/\Omega_0$, $U = U_0/\mathcal{E}_0$, $\Omega_0 = 2\mathcal{E}_0/\hbar$, and $\mathcal{E}_0 = \langle \hbar^2/(2mr^2) \rangle \approx \hbar^2/(2mr_S^2)$ is the natural energy scale of the science trap, where the brackets $\langle \cdot \rangle$ indicates an expectation value over r and z and $\hbar$ is the reduced Planck's constant. The function $\varphi_S(\theta)$ is periodic on $\theta \in [-\pi, \pi]$ and is a superposition of $\exp[i(\kappa \pm \sqrt{E + \kappa^2})\theta]$ with energy $E = -\kappa^2 + \epsilon(\kappa)$, where $\epsilon(\kappa)$ is periodic in κ with period one. Examples of the phase and magnitude of $\varphi_S(\theta)$ are shown in Fig. 3.2. For most κ, the phase of $\varphi_S(\theta)$ changes nearly linearly with

θ. Only for $\kappa \approx 1/2$ and, in fact, near any half-integer κ it changes rapidly near the barrier at $\theta = 0$. This rapid change around $\theta \in (-\theta_0, \theta_0)$ is accompanied by a decrease in density. The phase jump is $\pi(-\pi)$ for κ just above (below) $1/2$ and the density is 0 at $\theta = 0$ for $\kappa = 1/2$.

We define the phase drop across the barrier as $\gamma = 2\pi(n - s)$, where n is the winding number, which for the ground-state of the single-particle wave function is equal to the integer closest to κ, and the slope

$$s = \frac{d}{d\theta}\left\{\arg[\varphi_S(\theta)]\right\}\Big|_{\theta=-\pi}. \tag{3.2}$$

A graphical representation of γ for $\kappa = 0.51$ is shown in Fig. 3.2. In the rotating frame, the angular current

$$J(\kappa) = r_S \Omega_0 |\varphi_S(\theta)|^2 \left(\frac{d\arg[\varphi_S(\theta)]}{d\theta} - \kappa\right), \tag{3.3}$$

for any θ and we used the fact that $\langle 1/r \rangle = 1/r_S$.

3.2.2 Single-particle interference

After turning off the target trap, the atomic wave function, $\Psi(\vec{x}, t)$, freely expands and interferes. At time t after the release, it is imaged along the z axis leading to the observable $n(r, \theta, t) = \int_{-\infty}^{\infty} dz\, |\Psi(\vec{x}, t)|^2$, where $\Psi(\vec{x}, t = 0) = \Psi_{\text{init}}(\vec{x})$. During the expansion, the wave function of the torus and the disk remains separable in the z direction, i.e., $\psi_i(\vec{x}, t) = \chi_i(r, \theta, t)\phi_z(z, t)$. Thus, $n(r, \theta, t) = |\chi_R(r, \theta, t) + \chi_S(r, \theta, t)|^2$ as $\int dz |\phi_z(z, t)|^2 = 1$.

It is convenient to first follow the expansion with a numerical solution of the Schrödinger equation in the (r, θ) plane for κ near $1/2$. Figure 3.3 shows $n(r, \theta, t)$ for

33
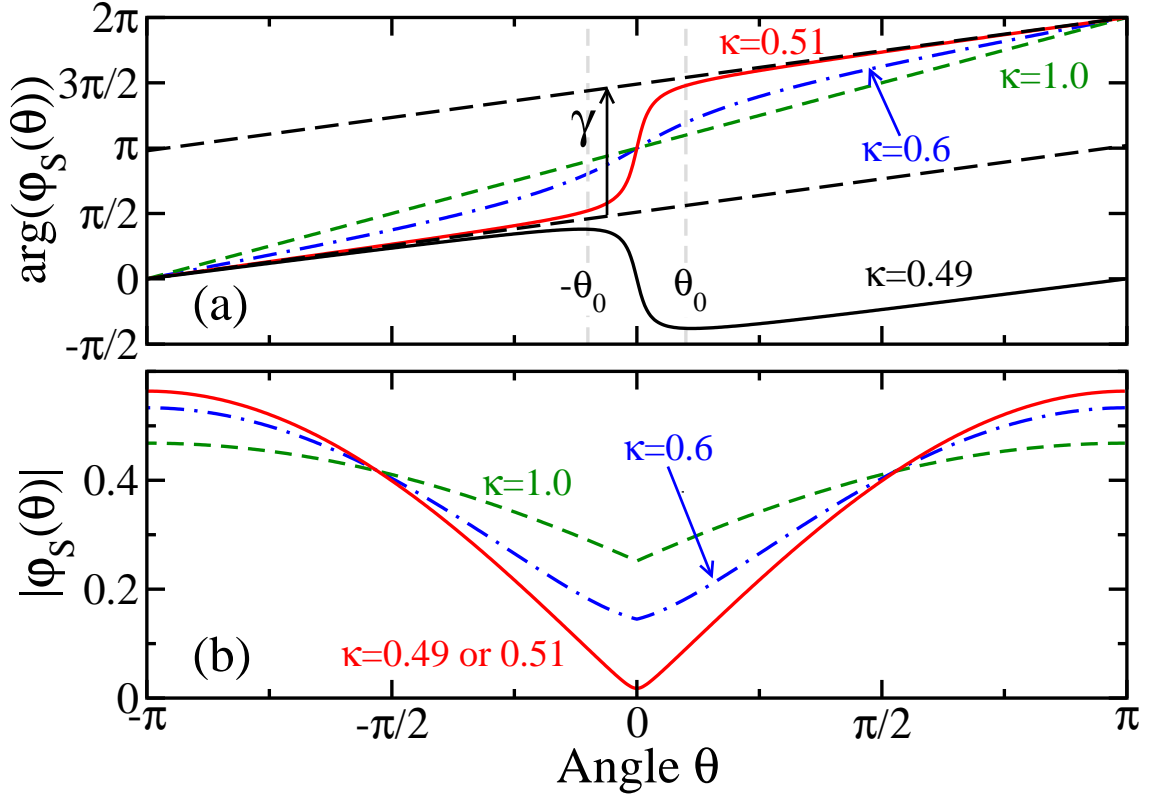
Figure 3.2: (Color online) Phase [panel (a)] and magnitude [panel (b)] of the single-particle ground-state angular wave function $\varphi_S(\theta)$ as a function of θ for various values of rotation rate κ. The wave function is calculated in the frame rotating with a delta-function potential of strength $U_0 = 1$ located at $\theta = 0$. For $\kappa \approx 1/2$, a sharp change in the phase occurs in the κ-dependent region $\theta \in (-\theta_0, \theta_0)$. The figure also shows the phase drop γ, defined in the text, for $\kappa = 0.51$.

two different expansion times. (Time propagation was carried out by switching to momentum space, applying appropriate time-dependent phase factors, and returning back to coordinate space.) We observe that as soon as the wave functions of the two traps overlap, the interference pattern consists of spirals. Later on, the self-interference of the science wave function yields circles superimposed on the spirals.

We confirm these interference patterns with an asymptotic expansion and study the associated time scales. The time evolution of the reference state is

$$\chi_R(r, \theta, t) = e^{-r^2/2\sigma_R^2(t)}/\mathcal{N}_1(t),\qquad(3.4)$$

where $\sigma_R^2(t) = \sigma_R^2 + i\hbar t/m$ and $\mathcal{N}_1(t)$ normalizes the wave function. Hence, for $t \gg m\sigma_R^2/\hbar$ the spatial extent of the reference wave function, $\sqrt{|\sigma_R^2(t)|}$, is proportional to the expansion time, corresponding to ballistic expansion. In contrast, the expanding science wave function is not analytically solvable. We can, however, derive an asymptotic series based on the pertinent time scales of the expansion of the science wave function. The shortest time scale is the ballistic time $\tau_B = m\sigma_S^2/\hbar$ determined by the initial radial width. In addition, as will become clear later, there are two position-dependent time scales: an intermediate time scale $\tau_C(r) = m\sigma_S(r + r_S)/\hbar$ and a long time scale $\tau_S(r) = mrr_S/\hbar$. We are interested in the expansion time interval $\tau_B \ll t \ll \tau_S(r)$. Figure 3.3 shows the density profile for two such times.

Formally, the expanding wave function $\chi_S(r, \theta, t)$ evolves as

$$\chi_S(r, \theta, t) = \int_0^\infty dr' \, r' \eta_S(r') \int_{-\pi}^\pi d\theta' \, G(r, \theta, r', \theta', t)\varphi_S(\theta'),\qquad(3.5)$$
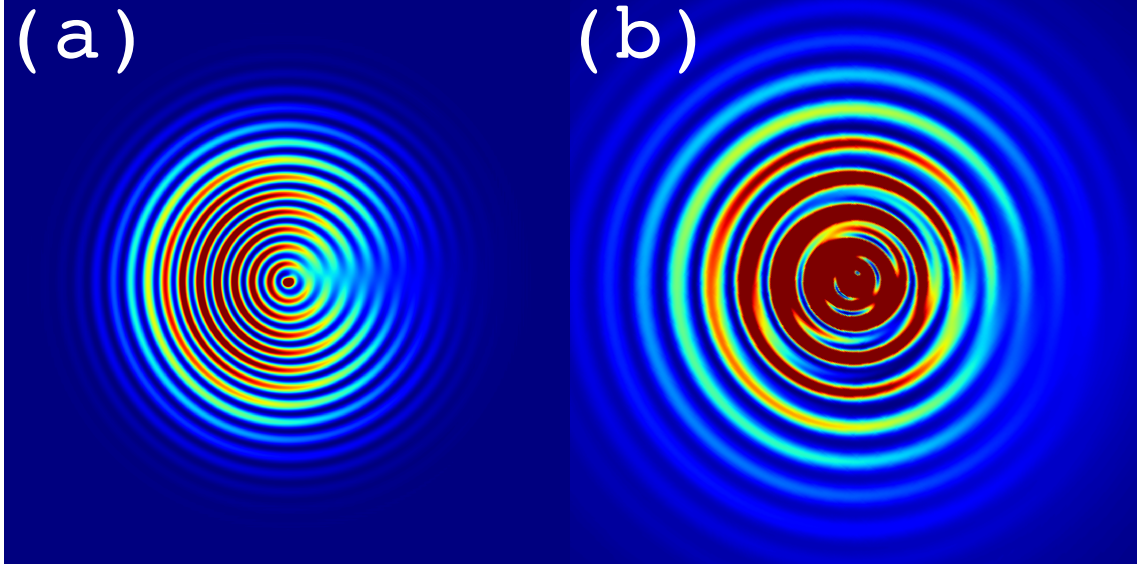
Figure 3.3: Numerical simulation of the integrated particle density $n(r, \theta, t)$ of a single particle, with winding number equal to 1, expanding in the rotating frame after release from a target trap. Panel (a) shows $n(r, \theta, t)$ with spirals at an early expansion time $t = 0.25\tau_C$, evaluated at $r = r_S$. Panel (b) shows a later time $t = 1.25\tau_C$, where the spirals are superimposed with circles due to self-interference of the toroidal wave function. The density near the center has been truncated for better contrast. The trap parameters are $\sigma_R = 0.025r_S$, $\sigma_S = 0.05r_S$, $U_0 = 1$, and $\kappa = 0.51$. The lengths of the sides in panels (a) and (b) correspond to $5.12r_S$ and $12.8r_S$, respectively. The parameters are chosen such that the overlap between the expanding science and reference wave functions is sufficient to show the spiral over a large range of radii.

where the free-particle Green's function [74] in two dimensions is

$$G(r, \theta, r', \theta', t) = \frac{m}{2\pi i \hbar t} \exp \left\{ \frac{im \left[r^2 + r'^2 - 2rr' \cos(\theta - \theta')\right]}{2\hbar t} \right\}. \qquad (3.6)$$

We note that the integral over r' is concentrated around $r' = r_S$. Consequently, the integral over θ' in Eq. 3.5 can be solved by noting that the phase on the right-hand side (RHS) of Eq. 3.6 oscillates rapidly for $t \ll mrr'/\hbar \approx \tau_S(r)$. Then, the method of steepest descent [75] gives an asymptotic series for the integral over θ' in powers of the small parameter $t/\tau_S(r)$. In fact, there are two stationary points located at $\theta' = \theta$ and $\theta' = \theta + \pi$, respectively. The remaining integral over r' is also solved using steepest descent for $\tau_B \ll t$ based on the small parameter σ_S/r_S. To leading order we find

$$\chi_S(r, \theta, t) = \frac{e^{-(r-r_S)^2/[2\sigma_S^2(t)]}\varphi_S(\theta) + e^{-(r+r_S)^2/[2\sigma_S^2(t)]}\varphi_S(\theta + \pi)}{\mathcal{N}_2(t)\sqrt{r}}, \qquad (3.7)$$

where the complex, time-dependent $\sigma_S^2(t) = \sigma_S^2(1 + it/\tau_B)$ is the square of the width of the expanding radial wave-packet and $1/\mathcal{N}_2(t)$ is a normalization factor. The wave function is a superposition of two expanding 1D Gaussians centered at r_S and $-r_S$ (except for the probability conserving factor $1/\sqrt{r}$). The asymptotic solution is valid for $\tau_B \ll t \ll \tau_S(r)$. This excludes the region near the origin, where $\tau_S(r)$ is small.

It is natural to ask whether the second term in Eq. 3.7 is important relative to the first term. Clearly, when $\sqrt{|\sigma_S^2(t)|} < r + r_S$ or equivalently $t < \tau_B(r + r_S)/\sigma_S = \tau_C(r)$ the second term is negligible. The interference of the first term with the reference wave function $\chi_R(r, \theta, t)$ in Eq. 3.7 leads to spirals in the density $n(r, \theta, t)$ as shown in Fig. 3.3(a). For $t \geq \tau_C(r)$ the second term cannot be ignored and

37

interferes with the first term. It leads to circles in addition to the spirals as shown in Fig. 3.3(b). An intuitive interpretation of $\tau_C(r)$ is that it corresponds to the time taken by signals from both antipodal points (r_S, θ) and $(r_S, \theta + \pi)$ of the initial $t = 0$ wave function of the torus to reach the observation point (r, θ) and interfere. This is the self-interference of the toroidal wave function.

3.2.3 Spirals

We are now in a position to quantify the spiral structure for $\tau_B \ll t \ll \tau_C$. We write $\chi_i(r, \theta, t) = \sqrt{n_i(r, \theta, t)} \exp[i\xi_i(r, \theta, t)]$, where $n_i(r, \theta, t)$ is the probability density and $\xi_i(r, \theta, t)$ is the phase. The integrated density becomes

$$n(r, \theta) = n_S(r, \theta) + n_R(r, \theta) + 2\sqrt{n_S(r, \theta) n_R(r, \theta)} \cos \xi(r, \theta),$$

where $\xi(r, \theta) = \xi_S(r, \theta) - \xi_R(r)$ and we suppress the time argument for notational simplicity. The last term on the RHS of this equation describes the interference of the wave functions in the two traps.

For the above time interval, the second term in Eq. 3.7 can be ignored, so that $n_R(r, \theta, t)$ is independent of θ, $n_S(r, \theta, t)$ is a separable function of r and θ, and $\xi(r, \theta) \approx \arg[\varphi_S(\theta)] - \hbar r r_S / (mt)$. (The argument $\arg[\phi_S(\theta)]$ is defined as a monotonic function of θ.) Then, spirals correspond to curves in the (r, θ) plane along which the phase $\xi(r, \theta)$ is constant. The densities $n_i(r, \theta)$ only lead to a slowly varying envelope in r and suppression of the signal near $\theta = 0$ that is most pronounced for a half-integer κ. Consequently, a spiral is described by the parametric curve $r(u) = (\xi_0 + \arg\{\varphi_S[\theta(u)]\}) \times \hbar t / (mr_S)$ and $\theta(u) = -\pi + u \mod 2\pi$, where ξ_0 is a

constant (typically chosen such that $n(r, \theta)$ is a local extremum) and u is the free parameter. In the absence of a rotating barrier but for a nonzero winding number n of the toroidal state, we find $\arg[\varphi_S(\theta)] = n\theta$ and the interference pattern has Archimedean spirals with $r(u) = (\xi_0 + nu) \times \hbar t/(mr_S)$ and $\theta(u) = -\pi + u \mod 2\pi$. These smooth spirals have been observed experimentally [71, 72].

A schematic of a spiral is shown in Fig. 3.4 at a single expansion time t for κ slightly greater than $1/2$, a case where $\varphi_S(\theta)$ has a sharp phase jump across the barrier near $\theta = 0$. For $|\theta| > \theta_0$ the spirals smoothly wind around the origin. In contrast, for $\theta \in (-\theta_0, \theta_0)$ there is a sharp, nearly discontinuous change in the spirals. For κ away from half-integer values, the spirals are smooth everywhere. The geometry of a spiral is completely determined by the phase $\xi(r, \theta)$ where the number of spiral arms is the winding number n. The densities $n_R(r, \theta)$ and $n_S(r, \theta)$ determine how many windings of a spiral are visible along the radial direction.

We characterize the discontinuity or jump of the spirals by lengths δ and Δ shown in Fig. 3.4. The quantity $\delta = 2\pi\hbar t/(mr_S)$ is the radial fringe spacing and measures the increment in r as $\xi(r, \theta)$ is increased by 2π at a fixed θ. Moreover, $\Delta = r_A(u + 2\pi) - r_A(u) = s \times 2\pi\hbar t/(mr_S)$, where we used the Archimedean spiral $r_A(u) = (\xi_0 + su) \times \hbar t/(mr_S)$ and $\theta_A(u) = -\pi + u \mod 2\pi$, and s is defined by Eq. 3.2. Intuitively, Δ is the radial distance covered by a spiral when it is smoothly continued across the barrier region. The two lengths depend on the dimensions of the torus and expansion time t.

The ratio $\Delta/\delta = s$ is independent of the radial wave function and expansion time. In fact, we can interpret Δ/δ as a measurement of the phase across the barrier

γ, since

$$\gamma = 2\pi(n - \Delta/\delta). \tag{3.8}$$

Moreover, it is a measurement of the angular current $J(\kappa)$, as the hydrodynamic equation, Eq. 3.3, at $\theta = -\pi$ gives

$$J(\kappa) = r_S \Omega_0 |\varphi_S(-\pi)|^2 \left(\Delta/\delta - \kappa\right). \tag{3.9}$$

For $t > \tau_C$ radial rings will get superimposed on the spirals due to the self-interference, making extraction of curves of constant $\xi(r,\theta)$ more difficult. Moreover, when $t \sim \tau_S(r)$, the derivatives of the initial angular wave function become important; finally, for $t \gg \tau_S(r)$, the probability distribution resembles the Fourier transform of the initial wave function, which has no spirals and the *in situ* phase cannot be read out.

3.3   Experimental atom SQUID and mean-field simulation

We now compare the single-particle analysis with the interference experiments and numerical simulations based on the Gross-Pitaevskii equation (GPE). The experimental setup is described in Sec. 3.3.1. Details of the numerical methods to simulate the GPE are given in Sec. 3.3.2, while Sec. 3.3.3 describes expansion time scales based on a self-similar expansion of a BEC from a target trap [76]. Section 3.4 compares the results and enables us to verify the extraction technique used in Ref. [72] for the phase drop across the barrier in terms of a measurement of Δ/δ.
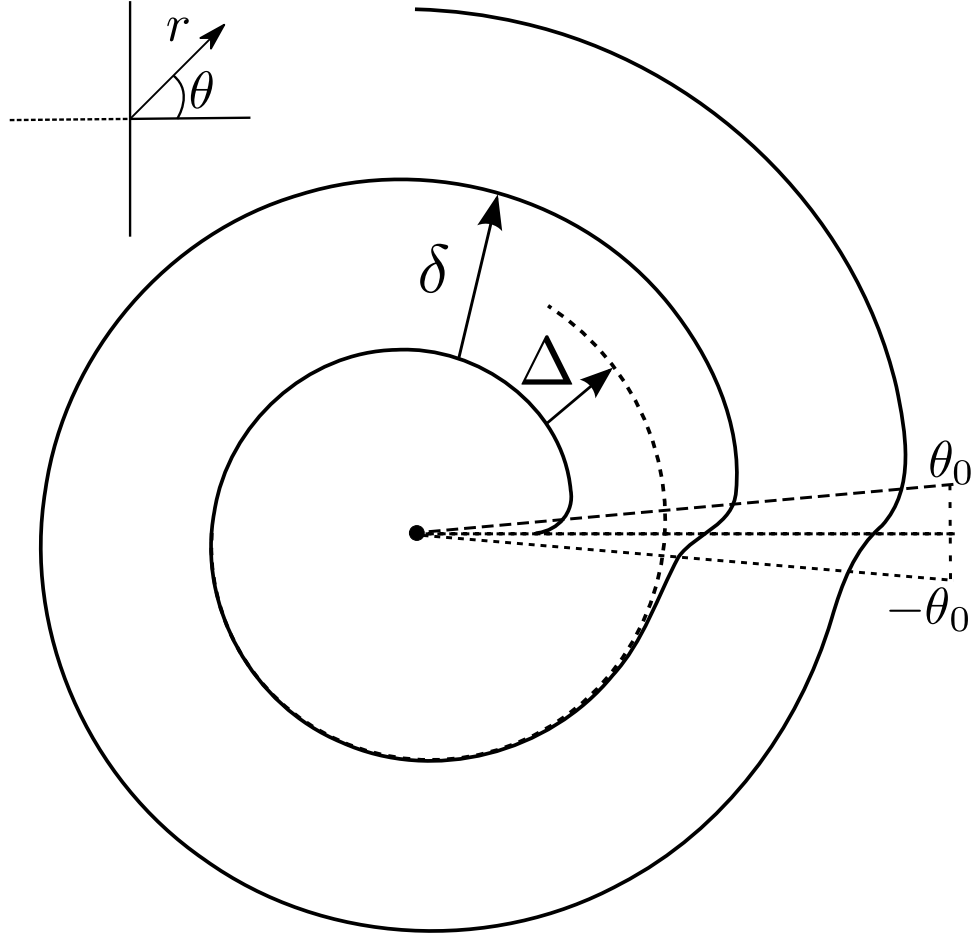
Figure 3.4: Schematic of a spiral-like contour (solid line) in the integrated density for κ slightly larger than $1/2$, so that the winding number $n = 1$. The contour has a constant phase $\xi(r, \theta) = \xi_0$. The phase of $\varphi_S(\theta)$ varies rapidly in the wedge $\theta \in (-\theta_0, \theta_0)$. In addition, an Archimedean spiral (dashed line) with the same initial angular velocity as the solid line is shown. Its parameters as well as the lengths δ and Δ are defined in the text.

(a)

Experiment

GPE

$\Delta/\delta = -0.0$ -0.2 -0.4 -0.6

130 μm

(b)

10 ms   15 ms   20 ms   25 ms

150 μm
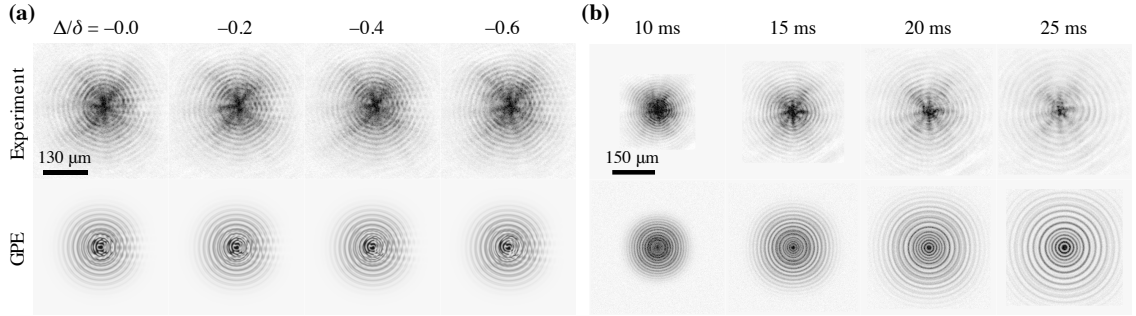
Figure 3.5: (a) Grayscale images of the interference pattern in the density profile after a 17-ms expansion time for four rotation rates of the barrier. The atom number density increases from blue to red with blue corresponding to zero density. The top and bottom rows show images from the experiment and GPE simulations with the same trapping potentials and atom number, respectively. The extracted Δ/δ for each rotation rate is shown above the images. The winding number is 0 for all images. (b) Images of experimental (top row) and GPE (bottom row) density profiles for four expansion times of a nonrotating condensate released from a target trap without a barrier.

3.3.1 Experimental setup

The interference experiments were conducted by the group of Gretchen Campbell at NIST [72]. In the experiments, a ^{23}Na BEC is created in a target trap with approximately 7×10^5 atoms and a chemical potential, $\mu/\hbar \approx 2\pi \times (2 \text{ kHz})$. Details of the creation of the trapping potential can be found in Refs. [54, 72]. The target trap has an external toroid with a radius of 22.4(4) μm and a radial trapping frequency of 240 Hz. Its central disk has a flat-bottomed potential and contains about 25% of the total atoms. The transverse trapping frequency of both traps is $\approx$600 Hz. This leads to a Bose condensate with a measured Thomas-Fermi radial width of about 6 μm in the toroid and a Thomas-Fermi radius of about 5 μm in the disk. The barrier potential has a Gaussian profile with a height less than the chemical potential of the atoms in the science trap. Its $1/e^2$ full width is $\approx$6 μm. Persistent current states are created by adiabatically ramping up the height of the barrier with a fixed rotation rate. The atom cloud is imaged along the transverse direction by absorption imaging, which measures the intensity of resonant light transmitted through the expanding gas.

3.3.2 Numerical simulation

Numerical GPE simulations of the experiments were carried out by our collaborator Mark Edwards. In the simulations, the initial wave function, $\Psi_{\text{GP}}(\vec{x})$, of the condensate in the target trap is found in a two-step process. First, the GPE is solved for the wave function of a BEC with a *stationary* weak link or barrier

but otherwise the same trapping potentials and atom number as in the experiment. Imaginary-time propagation and a two-dimensional effective Lagrangian variational method (2D LVM) [77, 78] are used, assuming a scattering length of $a = 2.8$ nm. The method is a variational technique whose trial wave function is the product of an arbitrary function in the (r, θ) plane and a Gaussian in the z direction with an (imaginary-)time-dependent width and a phase that is quadratic in z. This Ansatz leads to (a) a 2D effective GPE whose nonlinear coefficient contains the width of the Gaussian and (b) an evolution equation for the width that depends on the spatial integral of the fourth power of the absolute value of the solution of the effective GPE. This solution, $\Psi_{\text{Stat}}(\vec{x})$, is normalized such that $\int d^3\vec{x} |\Psi_{\text{Stat}}(\vec{x})|^2 = N$, the total atom number. In particular, the angular density profile of the science trap $\rho_{\text{Stat}}(\theta) = \int' r\,dr\,dz |\Psi_{\text{Stat}}(r, \theta, z)|^2$, where the radial integral only encompasses the science or the toroidal trap.

The second step is to add the rotation of the barrier by multiplying the stationary (and positive) $\Psi_{\text{Stat}}(\vec{x})$ with a spatially dependent phase that leaves the density profile unchanged, i.e., $\Psi_{\text{GP}}(\vec{x}) = \Psi_{\text{Stat}}(\vec{x}) e^{i\zeta(\vec{x})}$. The phase profile $\zeta(\vec{x})$ is 0 around and inside the central disk, and near the torus only depends on θ. For a given rotation rate κ and winding number n, it is found by simultaneously solving the hydrodynamic expression $J = r_S \Omega_0 \rho_{\text{Stat}}(\theta)(d\zeta(\theta)/d\theta - \kappa)$ and $\zeta(\pi) - \zeta(-\pi) = 2n\pi$. (Compare to Eq. 3.3 as well as see the Supplemental Material in Ref. [72]). The solution is similar in behavior to those shown in Fig. 3.2 and the phase drop follows from $\gamma = 2\pi(n - s)$, where $s = d\zeta(\theta)/d\theta \,|_{\theta = -\pi}$.

This phase-imprinting procedure is valid as long as the height of the barrier

is less than the chemical potential, the healing length $\ell = \sqrt{\hbar/(2m\mu)} \approx 0.5\,\mu$m is small compared to the width of the barrier ($\approx 6\,\mu$m), and the speed of the barrier is small compared to the speed of sound $c = \sqrt{\mu/m}$. These conditions are met in the experiment.

Finally, the expansion of a BEC released from a target-trap is simulated by solving the (real) time-dependent GPE using the same 2D-LVM method. The GPE solutions were only modified to include the effects of absorption imaging. The nonzero point-spread function of the imaging system is taken into account by convolving the simulated transmission with an Airy disk of the appropriate size.

3.3.3 Expansion time scales

References [76, 79] showed that a harmonically trapped and interacting Bose condensate expands at a much faster rate than a noninteracting gas of the same size. Here, we perform a similar analysis for expansion from a target trap. In fact, under the assumptions valid for phase imprinting in Sec. 3.3.2, it is sufficient to study expansion from a BEC in a toroidal trap without a barrier or rotation. We assume that the interactions are sufficiently strong that the Thomas-Fermi approximation holds along the r and z directions. The BEC wave function is then independent of θ and the harmonic confinement in the toroidal trap along the r and z directions leads to a BEC with a Thomas-Fermi radius, σ_{TF}, such that $\sigma_{\mathrm{TF}} \ll r_S$. Here, for simplicity we assume the same trap frequency along the two directions, i.e., $\omega_r = \omega_z \equiv \omega$.

Immediately, after the release of the toroidal trap the BEC expands rapidly in the r and z directions as the interaction energy gets converted to kinetic energy. This defines a ballistic time scale, $\tilde{\tau}_B$. (We use a tilde to denote time scales associated with expansion of the interacting BEC.) As $\sigma_{\mathrm{TF}} \ll r_S$, we can locally approximate an angular section of the torus as a 2D tube, which expands along its transverse directions. Such an elongated BEC undergoes a self-similar expansion [76, 79]. That is, in the hydrodynamic picture of the BEC and cylindrical coordinates, the density is $n(r, z, t) \approx n[r_S + (r - r_S)/\lambda(t), z/\lambda(t), t = 0]$ while the velocity field $\vec{v}(\vec{x}, t) = (v_r(r, t), 0, v_z(z, t))$, with $v_r(r, t) = (1 - \lambda(t)^{-2})(r - r_S)/t$ and $v_z(z, t) = (1 - \lambda(t)^{-2})z/t$. The scaling factor $\lambda(t) = \sqrt{1 + \omega^2 t^2}$, which implies $\tilde{\tau}_B = 1/\omega = m\sigma_S^2/\hbar$ and is the same as the single-particle ballistic time τ_B, even though the radial size of the BEC wave function $\sigma_{\mathrm{TF}} \gg \sigma_S$.

For $t \gg \tilde{\tau}_B$, the interaction energy has been converted to kinetic energy and the density profile has spirals, but the cloud is expanding more rapidly than the single-particle case. Hence, we expect that the time scale $\tilde{\tau}_C(r)$, where the spirals become modulated with circles due to the self-interference of the toroidal BEC, will be shorter than the equivalent single-particle time scale $\tau_C(r)$. We can derive $\tilde{\tau}_C$ following the intuitive understanding of signals from antipodal points (r_S, θ) and $(r_S, \theta + \pi)$ at $t = 0$ reaching (r, θ) at $t = \tilde{\tau}_C$. In other words, we require that the radial size of the toroidal BEC, $\lambda(\tilde{\tau}_C)\sigma_{\mathrm{TF}}$, is larger or equal to the distance between the observation point and the antipodal points, i.e., $r + r_S$ and $r - r_S$. Hence, $\tilde{\tau}_C \approx (r + r_S)/(\omega \sigma_{\mathrm{TF}}) = (\sigma_S/\sigma_{\mathrm{TF}})\tau_C$, which is smaller than τ_C.

3.4 Comparison of the experiment with theory

The experimental data and GPE simulations is compared in Fig. 3.5 by showing the dependence of the interference pattern on the rotation rate of the barrier and the expansion time. Figure 3.5(a) shows typical expanded clouds at 17-ms expansion time from the experiment and simulated GPE expansions for various rotation rates of the barrier leading to condensates with winding number $n = 0$. First, we see radial interference fringes at fixed θ and azimuthal interference fringes at fixed r similar to those in Fig. 3.4. The ratio Δ/δ from these experimental images is extracted following the procedure explained in Fig. 3.4. The phase drop across and the current through the barrier then follow from Eqs. 3.8 and 3.9, respectively. Near $\theta = 0$, where the barrier is located before release, the density profile has radial stripes, which are absent from the single-particle simulations and a consequence of interaction-induced expansion of atoms into the density depleted weak-link region. Last, starlike structures, which are due to residual azimuthal asymmetries in the toroidal potential, are visible.

Figure 3.5(b) shows expanding, rotationless clouds released from a trap without a barrier for various expansion times. For observation radii $r \geq 60$ μm and small expansion times $t \lesssim 20$ ms, the experimental data and GPE results show no evidence of self-interference of the toroidal BEC consistent with $t \leq \tilde{\tau}_C(r)$. For longer expansion times we observe self-interference. It is prominent near the cloud center, where radial fringes emerge with half the spacing of those at large radius.

In Fig. 3.5 the size, shape, and interference pattern of the clouds in the GPE

47
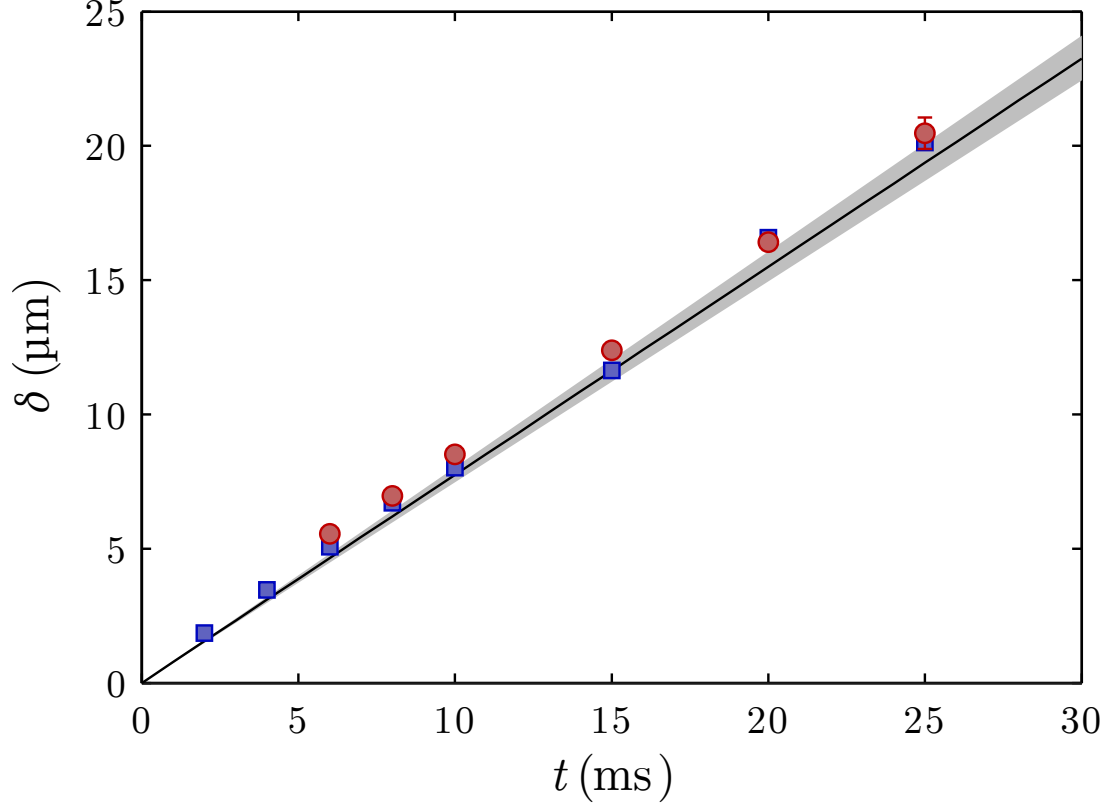
Figure 3.6: (Color online) Radial fringe spacing, δ, of the interference pattern as a function of time elapsed after the release of the target trap. The data are for a toroidal trap without a barrier and a BEC without winding. The experimental, GPE, and single-particle fringe spacings are shown by red dots with one-standard-deviation statistical error bars, blue squares, and a black line, respectively. The value of r_S has an uncertainty, which is shown by the shaded region around the black line.
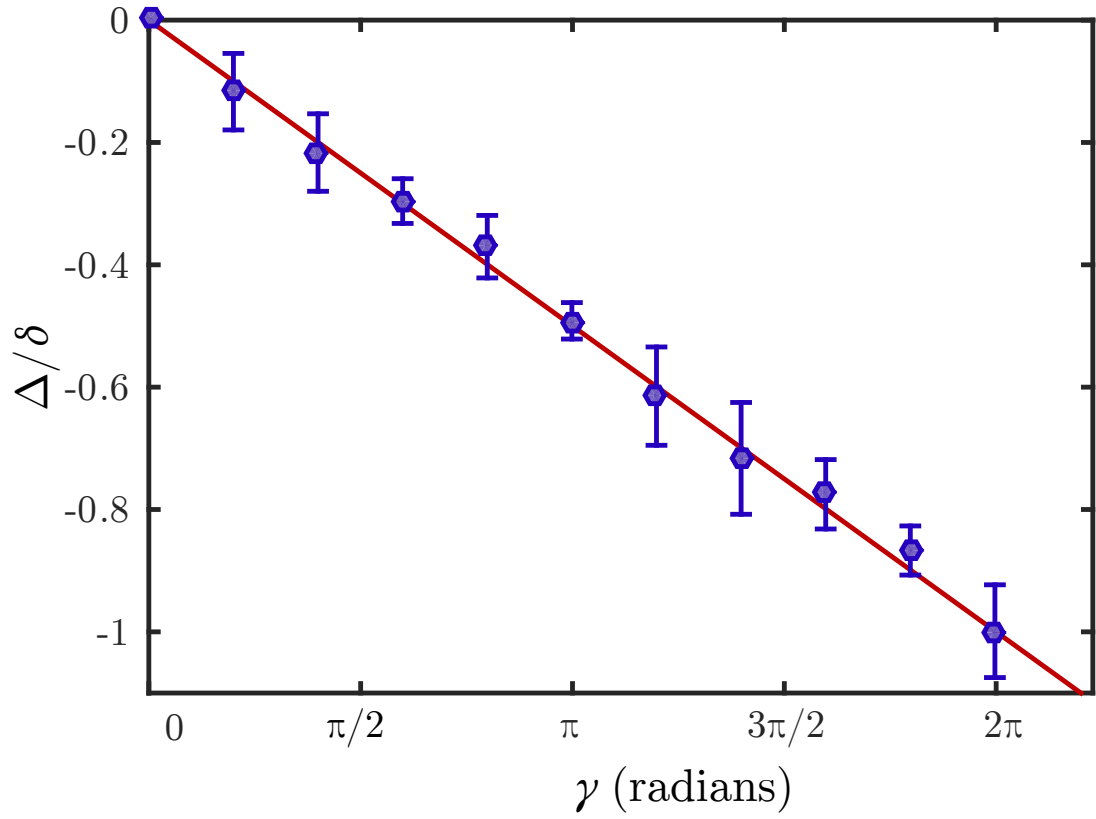
Figure 3.7: (Color online) The ratio Δ/δ as a function of *in situ* phase-drop γ across the rotating barrier from the GPE simulations of Fig. 3.5(a) (blue dots) and the single-particle prediction (solid line). Error bars are one-standard-deviation uncertainties from the fit to the density profile.

simulations agree well with those of the experiment. The agreement is made quantitative in Fig. 3.6 for the target trap without a barrier and a BEC without winding ($n = 0$). The figure shows the radial fringe spacing, δ, from the experimental data, GPE simulations, and the single-particle expression $\delta = 2\pi\hbar t/(mr_S)$ as functions of expansion time. The three cases are in excellent agreement, indicating that this fringe spacing is determined by the geometry of the system, i.e., the radius of the torus.

Figure 3.7 shows the extracted Δ/δ as a function of the imprinted phase drop γ across the barrier for the GPE simulations in Fig. 3.5(a). The result agrees within the uncertainties with the single-particle prediction, which indicates that interactions do not change the phase drop over the barrier region even though the angular density profile is distorted during the expansion. In other words, an extraction of the phase drop from a measurement of Δ/δ is valid even when the GPE and experiment have radial stripes for small θ near the weak link. The latter are absent from the single-particle interference pattern.

3.5   Conclusion

We have theoretically investigated an experiment that measures the phase drop in an atomic-SQUID. The atomic-SQUID consists of a BEC in a toroidal trap with a rotating barrier. The phase drop across the barrier is measured by interference with a reference disk BEC after release from the trapping potentials. We have studied the single-particle case and found that the structure of the interference pattern depends

on the expansion time after release. For short times, it consists of spirals, which have the same number of arms as the winding number of the toroidal wave function. The phase along a spiral is the same as the *in situ* phase of the angular wave function. Moreover, we find that the phase drop across the barrier and the current through it determine the geometry of spirals. For longer times, the spirals get superimposed by circles making phase readout difficult.

The conclusions from the single-particle model are confirmed by experiments with Bose condensed sodium atoms and numerical simulations based on the Gross-Pitaevskii equation even though interatomic interactions speed up the expansion, thereby shortening the associated time scales. In particular, one feature that is not changed is the fringe spacings of the interference pattern.

Most importantly, we have confirmed that the phase drops across the barrier as measured by the experiment agree with those of our single-particle model and mean-field simulations and accurately reflect the *in situ* value. This confirmation opens up the possibility of using this technique for measuring the current-phase relationship of, for example, excitations or weak links in degenerate, superfluid Fermi gases.

Chapter 4: Dynamics of dynamically unstable, bosonic few-mode quantum systems

4.1 Introduction

The advent of precise experimental control in ultracold atomic systems has motivated theoretical study in non-equilibrium dynamics in isolated quantum systems [80]. For generic Hamiltonian systems, the expectation value of a local observable at long times after a quench, a sudden change in a control parameter, is described by a Gibbs ensemble [81,82]. However, for integrable systems, a special class of Hamiltonian systems, the long-time behavior is instead believed to be described by a generalized Gibbs ensemble [82]. This important role of integrability on the time dynamics has been demonstrated experimentally [83,84]. Integrable systems are of much theoretical interest as they are amenable to exact analytic treatment. A classical integrable system can be solved using action-angle variables [85], while a quantum integrable system is solvable by the Bethe ansatz [86].

A mean-field approximation can be applied to a bosonic system with a macroscopically occupied mode. The time dynamics of the system is then governed by a classical Hamiltonian and described by classical trajectories in its phase space. For

a weakly interacting Bose-Einstein condensate (BEC), this classical trajectory is a solution of the time-dependent Gross-Pitaevskii equation for the order parameter with continuous spatial degrees of freedom [3]. In certain cases, it is sufficient to describe a bosonic system with just a few degrees of freedom. Some examples are a BEC in a double-well potential [87], a spin-1 spinor BEC within the single-mode approximation (SMA) [88, 89], and a few-site Bose-Hubbard model with a large occupation per site [90–92].

A bosonic system becomes dynamically unstable when it is prepared by a quench at a saddle point in its phase space. Dynamical instabilities have been predicted for vortices in trapped BECs [93–95], superfluid flow of BECs in optical lattices [96, 97], and BECs in cavities [98]. These predictions have been experimentally observed [99–103]. The instability is also used as an experimental route for the generation of squeezed states [7, 104–106]. A mean-field description is then insufficient and quantum fluctuations need to be included. Quantum corrections can be (partially) included by using the truncated Wigner approximation (TWA) [107–109], which models the dynamics of the Wigner distribution in the phase space. The TWA has been used to numerically study the effects of thermal fluctuations on a BEC [107], quenches in spinor condensates [110, 111], thermalization in chaotic systems [112, 113], and superfluid flow [114].

In this chapter, we analytically study the time dynamics of two integrable few-mode quantum systems within the truncated Wigner approximation after a quench of a parameter that makes the systems dynamically unstable. The chapter is set up as follows. We introduce dynamical instability in bosonic systems in Sec. 4.2

and TWA in Sec. 4.3. We define the integrability of classical Hamiltonians, which govern the mean-field limit of these systems, and introduce action-angle coordinates in Sec. 4.4. Section 4.5 introduces the concept of mixing in phase space due to time evolution and describes how this mixing leads to relaxation of an observable to a steady-state value. Using the pendulum as an illustrative example, we stress the role of separatrices in Sec. 4.6, derive general results for long-time expectation value of an observable in Sec. 4.7, and the time dynamics of relaxation of this expectation value in Sec. 4.8. We apply these results to the case of a condensate in a double-well potential (the double-well system) in Sec. 4.9 and a spin-1 BEC described by a single spatial mode in Sec. 4.10. We find that the deviation of the long-time expectation value from the classical value and the time scale of relaxation depends logarithmically rather than algebraically on the atom number. Finally, we conclude in Sec. 4.11.

4.2   Dynamical instability

The mean-field equations of motion of an isolated quantum bosonic system are equivalent to Hamilton's equations of motion of a classical system. The mean-field ground state is a stable equilibrium phase-space point, where the classical Hamiltonian has a minimum. On the other hand, a dynamically unstable state corresponds to a saddle point of this Hamiltonian. Such an unstable state can be prepared by starting from a minimum of the initial Hamiltonian and then quenching a system parameter to change this point to a saddle point of the final Hamiltonian.

As an example, consider the quantum oscillator $H_0 = (\hat{p}^2 + \hat{x}^2)/2$, where $\hat{x}$ and $\hat{p}$ are the canonical position and momentum operators, respectively. Here, we have set $\hbar$ and the natural frequency of the oscillator to one. Its mean-field ground state is the phase-space point $(x_c, p_c) = (0, 0)$, where $x_c = \langle\hat{x}\rangle$, $p_c = \langle\hat{p}\rangle$, and $\langle\ldots\rangle$ is the average over a quantum state. We make the state dynamically unstable by suddenly changing to the Hamiltonian $H_1 = (\hat{p}^2 - \hat{x}^2)/2$. Under the mean-field equations of motion, a dynamically unstable point is stationary. Thus, $x_c(t) = 0$ and $p_c(t) = 0$ hold for all times. In contrast, quantum evolution under H_1 leads to exponential growth in the unstable mode [3]. In fact, following the language of quantum optics, $H_1 \propto \hat{a}\hat{a} + \hat{a}^\dagger\hat{a}^\dagger$ leads to single-mode squeezing, where $\hat{a}(\hat{a}^\dagger) = (\hat{x} \pm i\hat{p})/\sqrt{2}$ is the annihilation (creation) operator of the mode.

4.3   The truncated Wigner approximation

The time evolution of a dynamically unstable system can be studied using the truncated Wigner approximation (TWA) [107]. It incorporates the leading order quantum corrections to the mean-field equations of motion [115]. In the TWA, a Wigner distribution function $W(\mathbf{x}, \mathbf{p}, t)$ time evolves under classical Hamilton's equations, in contrast to the mean-field approximation where the evolution of a single phase-space point $(\mathbf{x}(t), \mathbf{p}(t))$ is studied. Here, $\mathbf{x} = (x_1, \ldots, x_d)$ and $\mathbf{p} = (p_1, \ldots, p_n)$ are canonical position and momentum coordinates for a classical mean-field Hamiltonian system with d degrees of freedom. The initial distribution, $W_0(\mathbf{x}, \mathbf{p})$, is the Weyl-Wigner transform [13] of the prequench quantum ground state or any approx-

imation thereof.

For an observable $\mathcal{O}(\mathbf{x}, \mathbf{p})$, we define its evolution $\mathcal{O}(t) \equiv \mathcal{O}(\mathbf{x}(t), \mathbf{p}(t))$ along a trajectory $(\mathbf{x}(t), \mathbf{p}(t))$ with initial conditions $(\mathbf{x}_0, \mathbf{p}_0)$. The expectation value of $\mathcal{O}(t)$ over all trajectories is

$$
\begin{aligned}
\langle \mathcal{O}(t) \rangle &= \int_\Omega d\mathbf{x} d\mathbf{p} \, \mathcal{O}(\mathbf{x}, \mathbf{p}) W(\mathbf{x}, \mathbf{p}, t) \\
&= \int_\Omega d\mathbf{x}_0 d\mathbf{p}_0 \, \mathcal{O}(t) W_0(\mathbf{x}_0, \mathbf{p}_0),
\end{aligned}
\tag{4.1}
$$

with measures $d\mathbf{x} = dx_1 \cdots dx_n$, $d\mathbf{p} = dp_1 \cdots dp_n$ and the integral is over all phase space Ω. The distribution satisfies $\int_\Omega d\mathbf{x} d\mathbf{p} \, W(\mathbf{x}, \mathbf{p}, t) = 1$ for all t in accordance with Liouville's theorem [85].

4.4 Classical integrable systems

In classical mechanics, a Hamiltonian system with d degrees of freedom is integrable if there exist d mutually commuting (with respect to the Poisson bracket) conserved quantities [85]. Then a trajectory in the $2d$ dimensional phase-space lies on a d-dimensional torus. For an integrable system, the coordinates $(\mathbf{x}, \mathbf{p})$ can be transformed to canonical coordinates called actions $\mathbf{I} = (I_1, \ldots, I_d)$ and angles $\boldsymbol{\varphi} = (\varphi_1, \ldots, \varphi_d)$, such that Hamiltonian H is independent of $\boldsymbol{\varphi}$. Crucially, $(\mathbf{I}, \boldsymbol{\varphi})$ and $(\mathbf{I}, \boldsymbol{\varphi} + 2\pi \mathbf{m})$ correspond to the same phase-space point, where $\mathbf{m} = (m_1, \ldots, m_d)$ is a vector of integers. In these coordinates, the Hamilton's equations are

$$
\dot{I}_i = -\frac{\partial H(\mathbf{I})}{\partial \varphi_i} = 0, \quad \dot{\varphi}_i = \frac{\partial H(\mathbf{I})}{\partial I_i} \equiv \omega_i(\mathbf{I}),
\tag{4.2}
$$

for all $i \in \{1, \ldots, d\}$. The frequencies $\omega_i(\mathbf{I})$ only depend on $\mathbf{I}$. Hence, the actions are conserved quantities and the time evolution of the angles has the simple form

$$\boldsymbol{\varphi}(t) = \boldsymbol{\omega}(\mathbf{I})t + \boldsymbol{\varphi}_0, \tag{4.3}$$

where $\boldsymbol{\omega}(\mathbf{I}) = [\omega_1(\mathbf{I}), \ldots, \omega_d(\mathbf{I})]$ and $\boldsymbol{\varphi}(0) = \boldsymbol{\varphi}_0$.

For our Hamiltonian systems, action-angle coordinates are not globally defined. Instead, they are defined on disjoint regions of Ω by maps from each such region R to $\mathcal{I}_R \otimes \mathcal{J}$, where $\mathcal{I}_R \subset \mathbb{R}^d$ and $\mathcal{J} = [0, 2\pi]^{\otimes d}$ are the spaces spanned by the actions and angles, respectively. We then construct distribution functions $f_R(\mathbf{I}, \boldsymbol{\varphi}, t) = (2\pi)^d F\left(\mathbf{x}(\mathbf{I}, \boldsymbol{\varphi}), \mathbf{p}(\mathbf{I}, \boldsymbol{\varphi}), t\right)$ for $(\mathbf{x}, \mathbf{p}) \in R$ with normalization

$$\sum_R \int_{\mathcal{I}_R} d\mathbf{I} \int_{\mathcal{J}} \frac{d\boldsymbol{\varphi}}{(2\pi)^d} f_R(\mathbf{I}, \boldsymbol{\varphi}, t) = 1. \tag{4.4}$$

The latter follows from the fact that the Jacobian determinant of a canonical transformation is one. The distribution $f_R(\mathbf{I}, \boldsymbol{\varphi}, t)$ is periodic in $\boldsymbol{\varphi}$ and evolves as $f_R(\mathbf{I}, \boldsymbol{\varphi}, t) = f_{0,R}(\mathbf{I}, \boldsymbol{\varphi} - \boldsymbol{\omega}t)$, where $f_{0,R}(\mathbf{I}, \boldsymbol{\varphi}) = f_R(\mathbf{I}, \boldsymbol{\varphi}, 0)$ is the initial distribution. Moreover, Eq. 4.1 becomes

$$\langle \mathcal{O}(t) \rangle = \sum_R \int_{\mathcal{I}_R} d\mathbf{I} \int_{\mathcal{J}} \frac{d\boldsymbol{\varphi}}{(2\pi)^d} f_R(\mathbf{I}, \boldsymbol{\varphi}, t) \mathcal{O}_R(\mathbf{I}, \boldsymbol{\varphi}) \tag{4.5}$$

$$= \sum_R \int_{\mathcal{I}_R} d\mathbf{I} \int_{\mathcal{J}} \frac{d\boldsymbol{\varphi}_0}{(2\pi)^d} f_{0,R}(\mathbf{I}, \boldsymbol{\varphi}_0) \mathcal{O}_R(\mathbf{I}, \boldsymbol{\varphi}(t)), \tag{4.6}$$

where $\mathcal{O}_R(\mathbf{I}, \boldsymbol{\varphi})$ is the functional form of the observable in region R.

4.5   Phase-space mixing

A distribution function that is initially localized around a phase-space point typically stretches, tangles, and disperses over the accessible phase space. This

mixing in phase space has been studied in plasma physics [116] and astrophysics [117]. We illustrate this concept using a nonlinear oscillator. It is an integrable system with a Hamiltonian $H = Ur^4/8$, where $r^2 = p^2 + x^2$. In this case, the action-angle coordinates are globally defined. The action I is a function of r and the angle φ is the polar angle in the (x, p) plane. Points with different r rotate around the origin at different frequencies $\omega(I)$ and the distribution function stretches as shown Fig 4.1. Eventually, the distribution spreads uniformly and mixes in the compact coordinate φ, while remaining localized in r and I.

For a general integrable system, the frequencies $\boldsymbol{\omega}(\mathbf{I})$ depend nontrivially on $\mathbf{I}$. Hence, the distribution will eventually mix in $\boldsymbol{\varphi}$. It is important to realize that as the distribution function mixes in phase space fine-scale structures must develop in order to conserve the phase-space volume as required by Liouville's theorem. For the nonlinear oscillator, evolution leads to tightly wound spirals as shown in the third panel of Fig. 4.1.

Phase-space mixing simplifies the evaluation of the long-time expectation value of an observable. Experimentally-accessible observables are typically smooth functions of the phase-space coordinates. Then the distribution function with its fine-scale structures can be coarsened, i.e., in Eq. 4.5 we can replace $f_R(\mathbf{I}, \boldsymbol{\varphi}, t)$ by the time-independent distribution [118, §1]

$$\bar{f}_R(\mathbf{I}) \equiv \int_{\mathcal{J}} \frac{d\boldsymbol{\varphi}}{(2\pi)^d} f_R(\mathbf{I}, \boldsymbol{\varphi}, t) = \int_{\mathcal{J}} \frac{d\boldsymbol{\varphi}}{(2\pi)^d} f_{0,R}(\mathbf{I}, \boldsymbol{\varphi}). \tag{4.7}$$

Consequently, the expectation value at long times becomes

$$\lim_{t \to \infty} \langle \mathcal{O}(t) \rangle = \sum_R \int_{\mathcal{I}} d\mathbf{I}\, \bar{f}_R(\mathbf{I}) \int_{\mathcal{J}} \frac{d\boldsymbol{\varphi}}{(2\pi)^d} \mathcal{O}_R(\mathbf{I}, \boldsymbol{\varphi}). \tag{4.8}$$
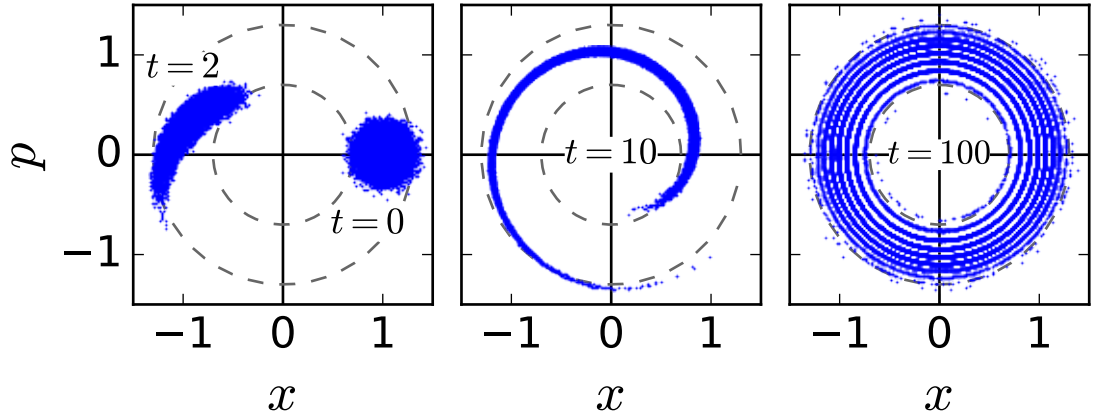
Figure 4.1: Phase-space mixing for an nonlinear oscillator with $U = 8$. Panels show the distribution $W(x, p, t)$ in phase-space (x, p) at times $t = 0, 2, 10$ and 100. Initially $W(x, p, t = 0)$ is a 2D Gaussian with standard deviation $\sigma = 0.1$ localized around $(x, p) = (1, 0)$. Approximately 99.7% of the points lie within the two dashed circles.

Thus, the long-time expectation value of an observable is given by the average over the accessible phase space weighted by $\bar{f}_R(\mathbf{I})$.

4.6 Dynamics near a separatrix

The description of the time evolution of the initially-localized Wigner distribution following dynamical instability for our double-well and spin-1 boson systems with a four- and six-dimensional phase space, respectively, must include a study of separatrices. As we will show in Secs. 4.9 and 4.10, their dynamics is controlled by a two-dimensional subspace Ω_{2D} spanned by canonical coordinates x_1 and p_1. This subspace contains a single saddle point that is connected to itself by one or more trajectories, known as separatrices. In fact, there are two separatrices and one separatrix for the double-well and spin-1 Bose system, respectively. The frequency $\omega_1(\mathbf{I})$ associated with a trajectory in Ω_{2D} goes to zero as its starting point approaches the saddle point. In fact, near the saddle point ω_1 varies sharply with $\mathbf{I}$, which leads to phase-space mixing in Ω_{2D}. The other frequencies ω_i for $i \neq 1$ are slowly varying near the saddle point and the distribution along the corresponding angles remains localized over the time scale for phase-space mixing in Ω_{2D}. In this and the next section, we discuss general features of trajectories and observables in the phase-space region near a separatrix. We develop this discussion using a simple pendulum, an integrable system with a two-dimensional phase space containing a single saddle point and two separatrices [119, §22.19].

The Hamiltonian of a simple pendulum is

$$H_{\text{pend}} = \frac{p^2}{2} + 1 - \cos\theta, \tag{4.9}$$

where p is the momentum, $\theta \in [-\pi, \pi]$ is the angular position and $\theta = \pm\pi$ are identical (we have set the pendulum's length and acceleration due to gravity to one). The point $(\theta, p) = (0, 0)$ corresponds to the stable equilibrium, while $(\theta, p) = (\pi, 0)$ is its sole saddle point and corresponds to a stationary upright pendulum. Around the saddle point $H_{\text{pend}} \sim 2 + (p^2 - x^2)/2$, where $x = (\theta - \pi) \bmod 2\pi$.

Figure 4.2 shows the equal-energy contours in the phase space of the pendulum. Two separatrices, $S+$ and $S-$, divide the phase space into three regions, denoted by A, B and C, with two distinct kinds of periodic motions: libration and rotation. Libration, confined to region B, is an oscillation where θ is bounded and does not pass the inverted position, $\theta = \pi$. Its time period is $T_{\text{lib}} = 4K(k)$, where $K(k)$ is the elliptic integral of the first kind [119], the modulus $k = \sqrt{\mathcal{E}/2}$ and $\mathcal{E}$ is the energy. Rotation is an unbounded motion in regions A or C, where the pendulum passes the inverted position. Its time period is $T_{\text{rot}} = 2kK(k)$, where $k = \sqrt{2/\mathcal{E}}$. Explicit expressions of libration and rotation motion are given in Appendix A.1.

On the separatrices the period is infinite and, hence, the action-angle coordinates (I_1, φ_1) are not defined. Thus, a saddle point precludes the existence of global action-angle coordinates. They are, however, defined separately in each of the three regions. Although, the explicit form of I_1 and φ_1 in terms of p and θ is known [120], it is not required for our analysis. We will need the location where φ_1 is zero along an equal-energy contour. We define it to be a point near the saddle point where $|p|$

is minimal. This condition is unique for regions A and C. In region B there are two such points and we choose the point where $\theta < 0$. As the travel time between the two points is a half the period, $\varphi_1 = \pi$ for the other point. Our choice of $\varphi_1 = 0$ is shown in Fig. 4.2 as dashed-dotted lines originating from the saddle point.

We remark on the properties of solutions on the separatrix, which will be useful later. The two solutions that vary significantly only around $t = 0$ and for which $\theta(t = 0) = 0$ are given by

$$\theta_{S\pm}(t) = \pm 2\arcsin(\tanh t), \quad p_{S\pm}(t) = \pm 2\operatorname{sech}(t). \tag{4.10}$$

Note that $p_{S\pm}(t)$ is well approximated by a bump function (also known as a test function [121]) that is nonzero in a finite domain, called the support, and vanishes outside its support. Moreover, an observable $\mathcal{O}(t)$ on the separatrix is (well approximated) by a constant plus a bump function, as long as it is smooth in both p and θ and periodic in θ.

Trajectories $(\theta(t), p(t))$ that start near one of the separatrices spend most of their time (within a period) near the saddle point as shown with two examples in Fig. 4.3. Changes in $\theta(t)$ and $p(t)$ from their saddle-point value are to good approximation equal to corresponding changes along trajectories on one or more of the separatrices. For example, for the rotation trajectory in Fig. 4.3 the momentum is $p_A(t) = p_{S+}(t - T_{\mathrm{rot}}/2)$ for $t \in [0, T_{\mathrm{rot}})$, while for the libration trajectory in Fig. 4.3 the momentum is $p_B(t) = p_{S+}(t - T_{\mathrm{lib}}/4) + p_{S-}(t - 3T_{\mathrm{lib}}/4)$ for $t \in [0, T_{\mathrm{lib}})$. In fact, the momentum along any trajectory starting near the saddle point in region $R = A$,

B or C, respectively, can be written as

$$p_R(t) \sim \sum_{n=-\infty}^{\infty} \left[\sum_{s=\{S\pm\}} \chi_R(s) \, p_s \left(t - t_{0,R}(s) - nT_R \right) \right], \qquad (4.11)$$

where the sum over n defines the momentum for all t (rather than a single period) and indicator functions $\chi_R(s)$ are either zero or one. For the pendulum, $\chi_A(S+)$, $\chi_B(S+)$, $\chi_B(S-)$ and $\chi_C(S-)$ are one; others are zero. The time shift $t_{0,R}(s) \in [0, T_R)$ and period T_R are determined by the starting point, where $T_R = T_{\text{rot}}$ and T_{lib} for $R = A, C$ and $R = B$, respectively. Thus, $p_R(t)$ is a sum over periodically occurring, nonoverlapping bump functions whose support is much smaller than the time period.

The asymptotic symbol $\sim$ in Eq. 4.11 and elsewhere in this chapter implies that either the trajectories start close to the saddle point or the averages are over a Wigner distribution that is initially localized around the saddle-point and whose initial width goes to zero. We also reserve the word asymptotic for these two cases, unless otherwise stated.

4.7 Long-time expectation value

We now derive the long-time expectation value of observables $\langle \mathcal{O}(t) \rangle$ that are smooth functions of the canonical coordinates $(\mathbf{x}, \mathbf{p})$ and depend only on the single action-angle coordinate φ_1 of the subspace Ω_{2D} in which the system undergoes phase-space mixing. For periodic coordinates, like angle θ of the pendulum, we restrict the observables to be periodic in θ. These constraints are not severe as many physically interesting observables have these properties.
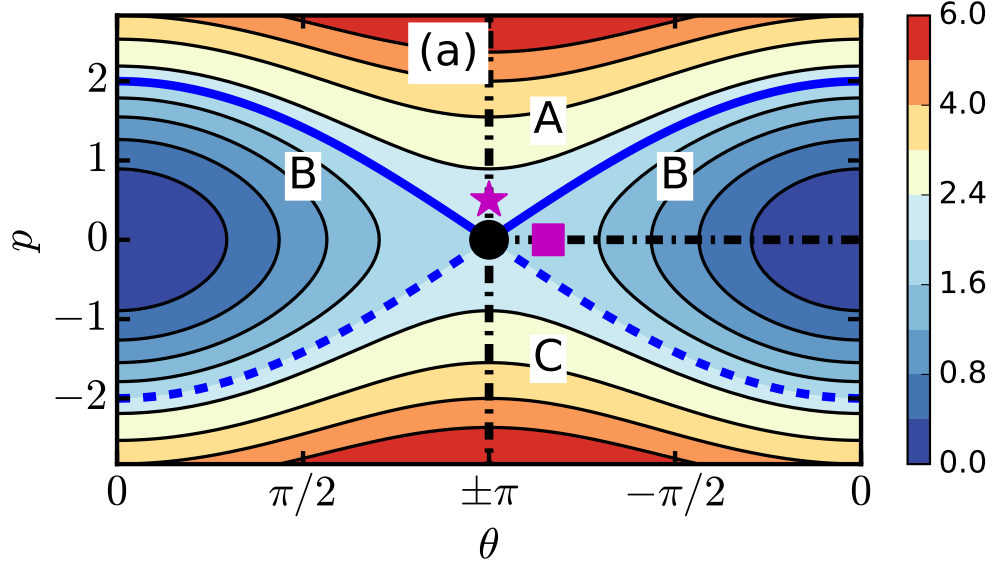
Figure 4.2: Equal-energy contours in the phase space (θ, p) of a simple pendulum. The phase-space is a cylinder as the lines $\theta = -\pi$ and π are equivalent. The saddle point is at $(\theta, p) = (\pi, 0)$. Separatrices are thick solid blue $(S+)$ and thick dashed blue $(S-)$ lines, which divide the phase space into libration (A and C) and rotating (B) regions. For each region, the thick dashed-dotted black line defines action-angle coordinate $\varphi_1 = 0$. The color map is nonlinear in order to better visualize the equal-energy contours.
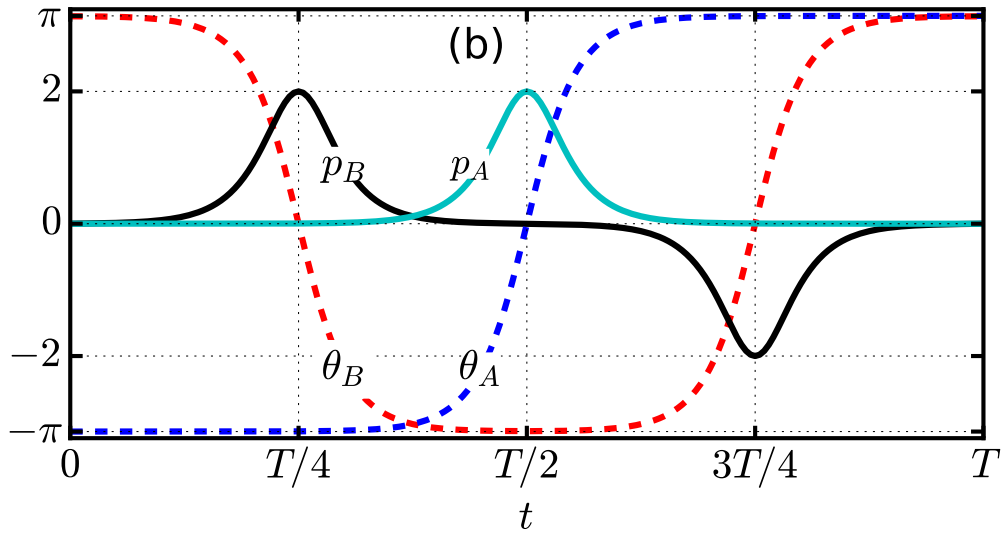
Figure 4.3: Trajectories starting near the saddle point of a pendulum as a function of time t for a single period T. Both a rotational $(\theta_A(t), p_A(t))$ and a librational $(\theta_B(t), p_B(t))$ trajectory are shown. The rotational trajectory lies in region A and starts from phase-space point denoted by a star in Fig. 4.2. The librational trajectory lies in region B and starts from the square in Fig. 4.2.

The first step is to write the asymptotic form of observable $\mathcal{O}_R(t)$ in region R, along a trajectory that comes close to the saddle point, in terms of its value along the separatrix trajectories $(x_{1,s}(t), p_{1,s}(t))$ in subspace Ω_{2D}. Here, s labels separatrices. (For the pendulum, $s \in \{S+, S-\}$.) We define $\mathcal{O}_s(t) = \mathcal{O}(x_{1,s}(t), p_{1,s}(t))$ and realize that $\mathcal{O}_s(t) = \mathcal{O}_{\text{sp}} + \mathcal{D}_s(t)$, where $\mathcal{O}_{\text{sp}}$ is the value of the observable at the saddle point and $\mathcal{D}_s(t)$ is a bump function localized around $t = 0$. Similarly, we decompose $\mathcal{O}_R(t) = \mathcal{O}_{\text{sp}} + \mathcal{D}_R(t)$, where $\mathcal{D}_R(t)$ is a series of periodically occurring, non-overlapping bump functions. Then, similar to Eq. 4.11, we write

$$\mathcal{O}_R(t) \sim \mathcal{O}_{\text{sp}} + \sum_{n=-\infty}^{\infty} \sum_s \chi_R(s) \mathcal{D}_s(t - t_{0,R}(s) - nT_R). \qquad (4.12)$$

The indicator functions $\chi_R(s)$ are system dependent and the sum s is over one or more separatrices.

To compute the long-time limit of $\langle \mathcal{O}(t) \rangle$ using Eq. 4.8, we need to evaluate the integral over angle φ_1. (Those over φ_j for $j > 1$ evaluate to unity for allowed observables.) We transform this integral to one over time by choosing a reference trajectory that starts near the saddle point with $\varphi_1(0) = 0$. For the pendulum, two such trajectories are shown in Fig. 4.3. Then, $\varphi_1(t) = \omega_1 t$ and

$$\int_0^{2\pi} \frac{d\varphi_1}{2\pi} \mathcal{O}_R(\mathbf{I}, \varphi_1) \sim \mathcal{O}_{\text{sp}} + \sum_s \chi_R(s) \frac{\omega_1(\mathbf{I})}{2\pi} \sum_{n=-\infty}^{\infty} \int_0^{T_R} dt\, \mathcal{D}_s(t - t_{0,R}(s) - nT_R).$$

$$(4.13)$$

For $n = 0$, the integrand $\mathcal{D}_s[t - t_{0,R}(s)]$ is localized around $t = t_{0,R}(s) \in (0, T_R)$. Its support is enclosed by the integration bounds $t = 0$ and T_R as the reference trajectory is near the saddle point at these times. For $n \neq 0$, there is no overlap between the support and the integration interval; hence, the integral is zero. We

extend the integration limits of t to $(-\infty, \infty)$ for the surviving $n = 0$ term and find

$$\int_0^{2\pi} \frac{d\varphi_1}{2\pi} \mathcal{O}_R(\mathbf{I}, \varphi_1) \sim \mathcal{O}_{\mathrm{sp}} + \sum_s \chi_R(s) \frac{\omega_1(\mathbf{I})}{2\pi} \int_{-\infty}^{\infty} dt \, \mathcal{D}_s(t). \tag{4.14}$$

Substituting this expression in Eq. 4.8, the long-time average becomes

$$\lim_{t \to \infty} \langle \mathcal{O}(t) \rangle \sim \mathcal{O}_{\mathrm{sp}} + \sum_R \frac{\langle \omega_1 \rangle_R}{2\pi} \left[\sum_s \chi_R(s) \int_{-\infty}^{\infty} dt \, \mathcal{D}_s(t) \right], \tag{4.15}$$

where the average frequency $\langle \omega_1 \rangle_R = \int_R d\mathbf{I} \, \bar{f}_R(\mathbf{I}) \, \omega_1(\mathbf{I})$ and the expression in the square brackets is independent of the distribution. Equation 4.15 is an important result of this chapter and relates the long-time expectation value of an observable to the mean frequency. The quantity $\mathcal{O}_{\mathrm{sp}}$ is the classical value of the observable and the second term is the quantum correction within the TWA.

For the pendulum, we assume the initial Gaussian distribution

$$W_0(\theta, p) = \frac{1}{2\pi d^2} e^{-(x^2 + p^2)/(2d^2)}, \tag{4.16}$$

where $x = (\theta - \pi) \mod 2\pi$. It is centered around the saddle point, analogous to the Wigner distribution of a mean-field state, where the width $d \ll 1$ [1]. Both H_{pend} and $W_0(\theta, p)$ are invariant under the transformations $p \to -p$ and $\theta \to -\theta$. Thus, the time-evolved distribution function is also invariant and observables $\mathcal{O}(\theta, p)$ that are odd functions of either θ or p have a vanishing expectation value at all times. In contrast, observables that are even functions in both θ and p can have non-vanishing expectation value.

---

[1] The quantum Hamiltonian of a pendulum in the θ basis is $-(\hbar^2/2)\partial_\theta^2 + 1 - \cos\theta$. The ground state is (approximately) a coherent (Gaussian) state around $\theta = 0$ with width $d = \sqrt{\hbar/2}$. When the sign of the potential $\cos\theta$ is suddenly changed, the state becomes dynamically unstable with the initial Wigner distribution as in Eq. 4.16.

As an illustration, consider $\mathcal{O}(\theta, p) = p^2$. Its functional form along the two separatrix solutions in Eq. 4.10 is the same, i.e., $[p_{\mathrm{S}+}(t)]^2 = [p_{\mathrm{S}-}(t)]^2$ and, using the indicator functions $\chi_R(s)$ for the pendulum, we find

$$\lim_{t \to \infty} \langle p^2(t) \rangle \sim \frac{\langle \omega_1 \rangle_A + \langle 2\,\omega_1 \rangle_B + \langle \omega_1 \rangle_C}{2\pi} \int_{-\infty}^{\infty} dt\, p_{\mathrm{S}+}^2(t). \tag{4.17}$$

Next, we realize that

$$\lim_{t \to \infty} \langle p^2(t) \rangle \sim \frac{\langle \varpi \rangle}{2\pi} \int_{-\infty}^{\infty} dt\, p_{\mathrm{S}+}^2(t) = \frac{8\,\langle \varpi \rangle}{2\pi}, \tag{4.18}$$

where we have used Eq. 4.10 to evaluate the time integral and defined the "auxiliary frequency" ϖ to be ω_1 in region A, C and $2\omega_1$ in region B with average $\langle \varpi \rangle = \langle \omega_1 \rangle_A + \langle 2\,\omega_1 \rangle_B + \langle \omega_1 \rangle_C$. From the definition of $\bar{f}_{0,R}(I_1)$, we also find that

$$\langle \varpi \rangle \equiv \int_0^{\infty} d\varpi\, \varpi \mathcal{F}(\varpi), \tag{4.19}$$

where the unit-normalized distribution function

$$\begin{aligned}
\mathcal{F}(z) &= \sum_R \int dI_1 \int_0^{2\pi} \frac{d\varphi_1}{2\pi} f_{0,R}(I_1, \varphi_1)\, \delta(z - \varpi(I_1)) \\
&= \int_{\Omega} d\theta dp\, W_0(\theta, p)\, \delta(z - \varpi(\theta, p))
\end{aligned} \tag{4.20}$$

and $\delta(z)$ is the Dirac delta function. The second equality shows that the explicit relationship between (I_1, φ_1) and (θ, p) is not required for the analysis.

As shown in Appendix A.1.1, the distribution $\mathcal{F}(\varpi)$ is well approximated by a Gaussian when the width d of the initial distribution $W_0(\theta, p)$ approaches zero. In fact, the location of its peak value is

$$\mu \equiv \langle \varpi \rangle \sim \frac{2\pi}{\ln[32/(\varkappa d^2)]} \ll 1 \tag{4.21}$$

and its width is

$$\sigma \sim \frac{\mu^2}{2\pi\sqrt{1-\varkappa^2}} \ll \mu, \tag{4.22}$$

where $\varkappa = 0.595\cdots$. Thus, the quantum correction to the long-time expectation value of $p^2(t)$ is $1/O(\ln|d|)$.

4.8 Time dynamics of relaxation

In this section, we study the relaxation of an observable to its long-time expectation value. Observables again depend on only a single angle φ_1 and are periodic in φ_1. We can then write an observable in region R as a Fourier series

$$\mathcal{O}_R(\mathbf{I}, \varphi_1) = \sum_{m=-\infty}^{\infty} \Theta_R(\mathbf{I}; m)e^{im\varphi_1}, \tag{4.23}$$

with

$$\Theta_R(\mathbf{I}; m) = \int_0^{2\pi} \frac{d\varphi_1}{2\pi} \mathcal{O}_R(\mathbf{I}, \varphi_1)\, e^{-im\varphi_1}. \tag{4.24}$$

Now, as in Sec. 4.7, we transform the integral over φ_1 into one over time by choosing a reference trajectory with $\varphi_1(0) = 0$ and insert $\varphi_1(t) = \omega_1(\mathbf{I})t$. Using Eq. 4.12, we find

$$\Theta_R(\mathbf{I}; m) \sim \mathcal{O}_{\mathrm{sp}}\,\delta_{m0} + \sum_s \chi_R(s)e^{-im\alpha_R(s)} \times \tag{4.25}$$

$$\sum_{n=-\infty}^{\infty} \int_{-t_{0,R}(s)}^{T_R-t_{0,R}(s)} \frac{d\tau}{2\pi}\, \omega_1 \mathcal{D}_s(\tau - nT_R)e^{-im\omega_1\tau},$$

where δ_{ij} is the Kronecker delta, $\alpha_R(s) = \omega_1 t_{0,R}(s)$, the integration variable $\tau = t - t_{0,R}(s)$, and we have suppressed the dependence of ω_1 and T_R on $\mathbf{I}$. Only the

$n = 0$ term contributes and

$$\Theta_R(\mathbf{I}; m) \sim \mathcal{O}_{\text{sp}}\, \delta_{m0} + \sum_s \chi_R(s) e^{-im\alpha_R(s)} \omega_1 \mathfrak{D}_s(m\omega_1), \qquad (4.26)$$

where the Fourier transform $\mathfrak{D}_s(x) = \int_{-\infty}^{\infty} dt/(2\pi)\, \mathcal{D}_s(t) e^{-ixt}$. Substituting this expression into Eq. 4.23 and using $\mathcal{O}_R(t) \equiv \mathcal{O}_R(\mathbf{I}, \varphi_1(t))$, Eq. 4.6 becomes

$$\langle \mathcal{O}(t) \rangle \sim \mathcal{O}_{\text{sp}} + \sum_{m=-\infty}^{\infty} \sum_{R,s} \chi_R(s) e^{-im\alpha_R(s)} \left\langle \omega_1 \mathfrak{D}_s \left(m\omega_1 \right) e^{im[\omega_1 t + \varphi_1(0)]} \right\rangle_R, \qquad (4.27)$$

where $\langle \ldots \rangle_R$ is the average over $f_{0,R}(\mathbf{I}, \boldsymbol{\varphi})$, the initial distribution restricted to region R. We realize that at long times all Fourier terms except the $m = 0$ term must go to zero in order to recover Eq. 4.15.

We now specialize to the pendulum system. The phases $\alpha_R(s)$ are $\alpha_A(S+) = \alpha_C(S-) = \pi$, $\alpha_B(S-) = \pi/2$ and $\alpha_B(S+) = 3\pi/2$ when $\chi_R(s)$ is nonzero and, as shown in Appendix A.1.2, we have

$$\langle \mathcal{O}(t) \rangle \sim \mathcal{O}_{\text{sp}} + \sum_{m=-\infty}^{\infty} (-1)^m \int_0^{\infty} d\varpi\, \mathcal{F}(\varpi) \varpi \mathfrak{D}_{S+}(m\varpi) e^{im\varpi t}, \qquad (4.28)$$

where, as in Sec. 4.7, the auxiliary frequency ϖ is ω_1 in regions A, C and $2\omega_1$ in region B. The distribution $\mathcal{F}(\varpi)$ is well approximated by a Gaussian with mean and width given in Eqs. 4.21 and 4.22, respectively. The factor $\varpi \mathfrak{D}_{S+}(m\varpi)$ is slowly varying across the width of $\mathcal{F}(\varpi)$. Carrying out the integral over ϖ in Eq. 4.28 (after extending the lower limit of the integral to $-\infty$) gives

$$\langle \mathcal{O}(t) \rangle \sim \mathcal{O}_{\text{sp}} + \sum_{m=-\infty}^{\infty} (-1)^m \mu\, \mathfrak{D}_{S+}(m\mu) e^{im\mu t - m^2 \sigma^2 t^2/2}. \qquad (4.29)$$

Specifically, for $\mathcal{O}(\theta, p) = p^2$, we have

$$\langle p^2(t) \rangle \sim \frac{4\mu}{\pi} + \sum_{m=1}^{\infty} (-1)^m \frac{4m\mu^2 \cos(m\mu t)}{\sinh(\pi m\mu/2)} e^{-m^2 \sigma^2 t^2/2}, \qquad (4.30)$$

and the time evolution is a sum of oscillatory functions with damping that is Gaussian in time. The oscillation frequency of each term increases linearly with m, while simultaneously its damping time, $1/(m\sigma)$, decreases.

4.9   Condensate in a double-well potential

A Bose-Einstein condensate in a weakly coupled double-well potential displays Josephson oscillations and macroscopic self-trapping [87, 122–125]. These phenomena are adequately described by a mean-field approximation. Moreover, dynamical instabilities, where quantum effects become important, have also been studied [126–128].

A BEC in a symmetric double-well potential is well described by assuming that only two modes $\Psi_1(\vec{r})$ and $\Psi_2(\vec{r})$ are occupied, one for each well. In the mean-field description, the time-dependent order parameter or condensate wavefunction is $\psi_1(t)\Psi_1(\vec{r}) + \psi_2(t)\Psi_2(\vec{r})$ with complex-valued amplitudes $\psi_j(t)$. The real and imaginary parts of $\psi_j(t)$ form two pairs of canonical coordinates. Hence, the system has a four-dimensional phase space. Its classical Hamiltonian is

$$H_{\mathrm{dw}} = -J(\psi_1\psi_2^* + \psi_1^*\psi_2) + \frac{U}{2}(|\psi_1|^4 + |\psi_2|^4), \tag{4.31}$$

where U and $J > 0$ are the on-site interaction and tunneling energies, respectively [87]. The total number of atoms $N = |\psi_1|^2 + |\psi_2|^2$ and energy $\mathcal{E}$ are conserved, making the system integrable. We note that the underlying quantum Hamiltonian is solvable by the Bethe ansatz [129].

Following the literature, it is convenient to introduce $\psi_j(t) = \sqrt{N_j(t)}e^{i\theta_j(t)}$,

71
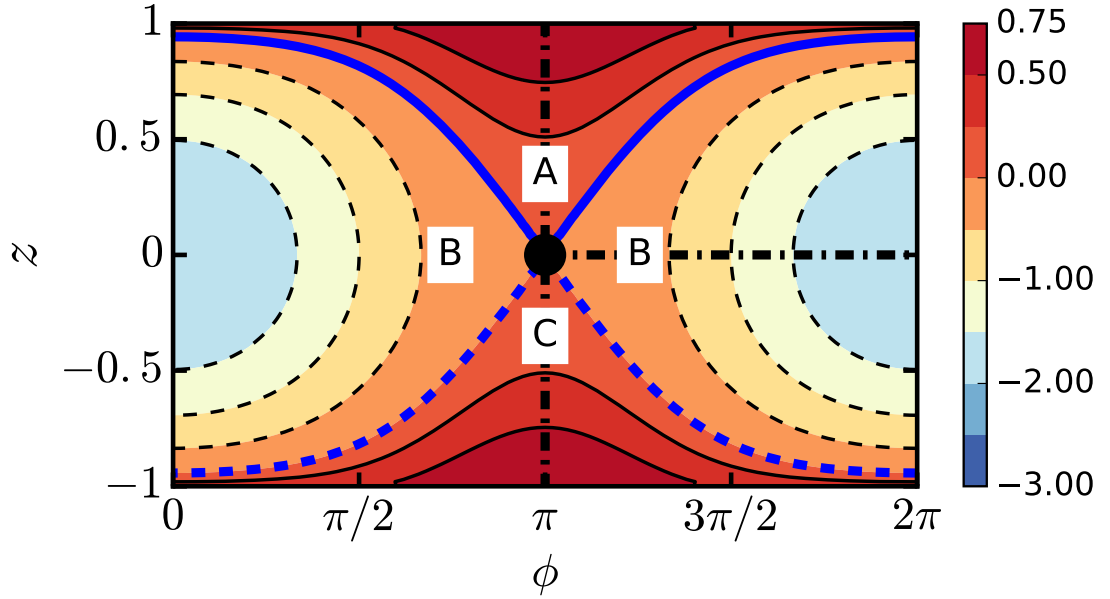
Figure 4.4: Equal-energy contours in the phase space (ϕ, z) of a condensate in a double-well potential for $\Lambda = 3$. The phase space is equivalent to a sphere, where the lines $z = 1$ and $z = -1$ correspond to the north and south pole, respectively. Moreover, $(0, z)$ and $(2\pi, z)$ are equivalent. Separatrices thick solid blue line $(S+)$ and thick dashed blue line $(S-)$ intersect at the saddle point shown by a solid circle. They divide the phase space into regions A, B and C. For each region, the thick dashed-dotted black line defines the action-angle coordinate $\varphi_1 = 0$. The color map is nonlinear in order to better visualize the equal-energy contours.
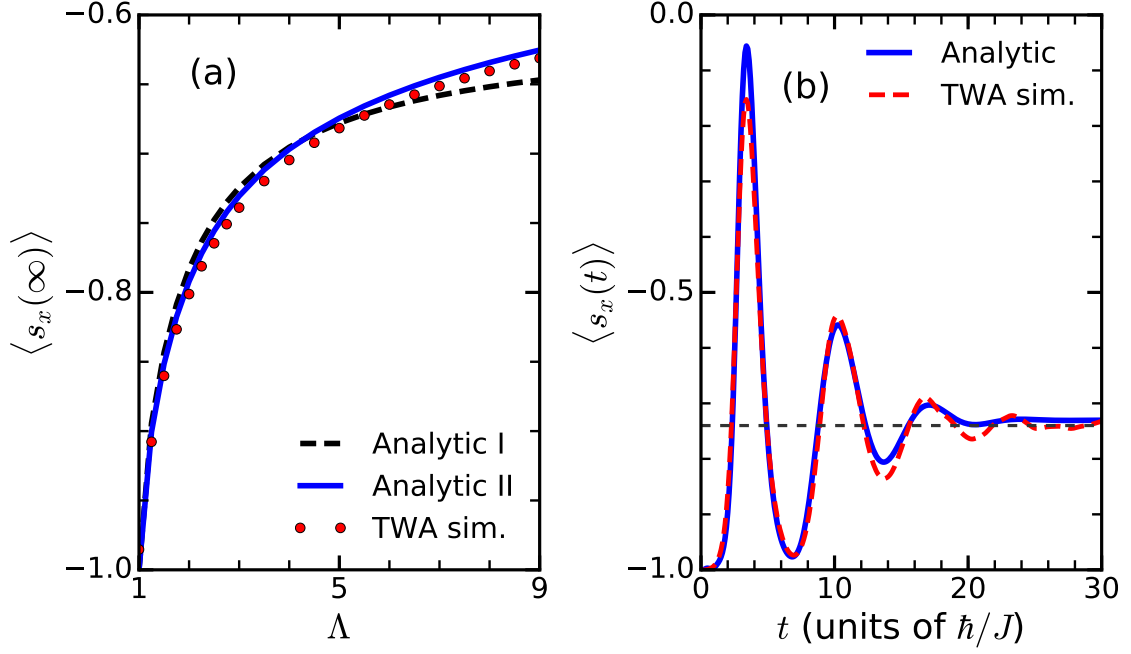
Figure 4.5: Long-time expectation values and time dynamics within the TWA of a Bose-Einstein condensate in a double-well potential following a quench to a dynamically unstable point. Panel (a) shows the long-time expectation value of an observable s_x as defined in the text. The dotted black and solid blue lines show the analytic result of Eq. 4.35 with mean $\mu \equiv \langle \varpi \rangle$ given by Eq. A.34 and with μ obtained by numerically sampling the initial Wigner distribution, respectively. The red circles are values obtained by numerical TWA simulations. Panel (b) shows the time dynamics of $\langle s_x(t) \rangle$ for $\Lambda = 3$. The solid blue line is $\langle s_x(t) \rangle$ in Eq. 4.36 with μ and width σ obtained by numerically sampling from the initial Wigner distribution. The red dashed line is found from numerical TWA simulations. For both panels, the number of particles $N = 1000$.

where N_j is the number of atoms in and θ_j is the phase of the condensate in the j-th well [87]. We can then express Eq. 4.31 in terms of the fractional population difference $z = (N_1 - N_2)/N$ and phase difference $\phi = \theta_1 - \theta_2$, where $\phi \in [0, 2\pi]$ and $\phi = 0, 2\pi$ are identical. In fact, we have $H_{\mathrm{dw}} = NJ \times h_{\mathrm{dw}}(\phi, z)$, where $h_{\mathrm{dw}}(\phi, z)$ is the "single-atom" Hamiltonian that depends on the effective N-dependent coupling strength $\Lambda = UN/(2J)$ and is given by

$$h_{\mathrm{dw}}(\phi, z) = \frac{\Lambda z^2}{2} - \sqrt{1 - z^2} \cos \phi. \tag{4.32}$$

The Hamiltonian $h_{\mathrm{dw}}(\phi, z)$ has a single minimum located at $(\phi, z) = (0, 0)$ for $\Lambda > 0$. For $\Lambda > 1$, the Hamiltonian has a saddle point located at $(\phi, z) = (\pi, 0)$. Near the saddle point, $h_{\mathrm{dw}}(\phi, z) \sim 1 + [(\Lambda - 1)z^2 - (\phi - \pi)^2]/2$. Figure 4.4 shows equal-energy contours of $h_{\mathrm{dw}}(\phi, z)$ in the two-dimensional phase space (ϕ, z) for $\Lambda > 1$. Two separatrices $S+$ and $S-$ divide the phase space into regions A, B, and C. Similar to the pendulum, in regions A and C the motion is rotational while in region B it is librational. Explicit expressions for rotation and libration trajectories are given in Appendix A.2. On each separatrix, we consider a trajectory $(\phi_s(t), z_s(t))$ that only varies significantly around $t = 0$ and for which $|z(t)|$ has a maximum at $t = 0$. Along these trajectories

$$z_{S\pm}(t) = \pm \frac{2\sqrt{\Lambda - 1}}{\Lambda} \operatorname{sech}\left(\sqrt{\Lambda - 1}\, t\right). \tag{4.33}$$

The corresponding $\phi_{S\pm}(t)$ can be calculated by solving $h_{\mathrm{dw}}(\phi_{S\pm}(t), z_\pm(t)) = 1$.

We now consider the dynamics of a (zero-temperature) condensate with N atoms prepared at the saddle point within the TWA. We assume that the initial

state is $(\psi_1, \psi_2) = (\sqrt{N/2}, -\sqrt{N/2})$ with corresponding Wigner distribution

$$W_0(\psi_i, \psi_i^*) = \frac{4}{\pi^2} e^{-2|\psi_1 - \sqrt{N/2}|^2 - 2|\psi_2 + \sqrt{N/2}|^2}, \tag{4.34}$$

where $i \in \{1, 2\}$ and the probability measure is $\prod_i d\psi_i^* \, d\psi_i$. The distribution $W_0(\psi_i, \psi_i^*)$ corresponds to the Wigner transform of a product of coherent states, one in each of the two modes with mean atom number $N/2$ and a relative phase of π.

Observables have a natural interpretation as spin operators when we represent the phase-space (ϕ, z) as a sphere with polar angle $\vartheta = \arccos(z)$ and azimuthal angle ϕ. Hence, observable z corresponds to s_z, the z component of the unit "spin" $\vec{s}$. The other spin components are $s_x = \sin \vartheta \cos \phi = \sqrt{1 - z^2} \cos \phi$ and $s_y = \sin \vartheta \sin \phi = \sqrt{1 - z^2} \sin \phi$. As in the pendulum case, observables that are odd functions of ϕ or z have vanishing expectation values for all times. Thus, $\langle s_z(t) \rangle = \langle s_y(t) \rangle = 0$, but $\langle s_x(t) \rangle$ is non-vanishing. Using Eq. 4.32, we find that $s_x = \Lambda z^2/2 - 1$ on the separatrices.

Now we evaluate the long-time limit and time dynamics of $\langle s_x(t) \rangle$. The indicator functions $\chi_R(s)$ are $\chi_A(S+) = 1$, $\chi_B(S+) = 1$, $\chi_B(S-) = 1$, $\chi_C(S+) = 1$ and zero otherwise. Then using Eqs. 4.15, 4.33 and following the derivation in Sec. 4.7 we find

$$\lim_{t \to \infty} \langle s_x(t) \rangle \equiv \langle s_x(\infty) \rangle \sim -1 + \frac{2\sqrt{\Lambda - 1}}{\pi \Lambda} \langle \varpi \rangle, \tag{4.35}$$

where the auxiliary frequency ϖ is ω_1 in regions A, C and $2\omega_1$ in region B. The time evolution of $\langle s_x(t) \rangle$ is found by repeating the steps in Sec. 4.8. Details are given in Appendix A.2, where we find that the asymptotic expression of $\langle s_x(t) \rangle$ is again

given by Eq. 4.28, with a distribution function $\mathcal{F}(\varpi)$ that is a well approximated by a narrow Gaussian with mean $\mu = \langle \varpi \rangle$ and width $\sigma \ll \mu$ that depend on Λ and N. Then, Eq. 4.29 holds and

$$\langle s_x(t) \rangle \sim \langle s_x(\infty) \rangle + \sum_{m=1}^{\infty} (-1)^m \frac{2m\mu^2 \cos(m\mu t)}{\Lambda \sinh[m\mu\pi/(2\sqrt{\Lambda - 1})]} e^{-m^2\sigma^2 t^2/2}. \qquad (4.36)$$

It is important to note that, as shown in Appendix A.2.1, for large N the mean μ is $O(1/\ln N)$ and the width is $O[1/(\ln N)^2]$. Thus, the quantum correction to the long-time value of $\langle s_x(t) \rangle$ is $O(1/\ln N)$. Quantitative analytical expressions for μ and σ have only been found for $\Lambda - 1 \ll 1$.

Figures 4.5(a) and (b) show the long-time expectation value Eq. 4.35 as a function of Λ and Eq. 4.36 as a function of time, respectively. In addition, the figures show good agreement with numerical TWA results. In the numerical implementation of TWA, we sample from the initial distribution $W_0(\psi_i, \psi_i^*)$, propagate the classical equations of motion, and compute the expectation value of an observable by averaging over the sample.

4.10 Spinor BEC within the single-mode approximation

A trapped spin-1 (spinor) Bose-Einstein condensate is well described by a single spatial mode for its three magnetic sublevels [88, 89, 130]. This single-mode approximation (SMA) is valid when the spin healing length, the length scale over which the spin populations of the condensate can change significantly, is larger than the condensate size. The mean-field theory within SMA has turned out to adequately describe atomic spinor experiments with strong spatial confinement [131–

134]. Quenches to dynamical instability, where quantum effects need to be treated, have also been studied experimentally [106, 135].

The mean-field wavefunction of the spinor BEC in the SMA is the vector $\vec{\Psi}(\vec{r}, t) = (\psi_{-1}(t), \psi_0(t), \psi_{+1}(t))^T \Phi(\vec{r})$, where $\psi_j(t)$ is the complex amplitude of the j-th magnetic sublevel along the external magnetic field and $\Phi(\vec{r})$ is the time-independent unit-normalized spatial mode. The phase space spanned by the $\psi_j(t)$ has six dimensions and the system has three mutually commuting conserved quantities, namely energy, total atom number $N = \sum_j |\psi_j(t)|^2$, and magnetization $M = \sum_j j|\psi_j(t)|^2$. Thus, the system is integrable. We note that the underlying quantum few-mode Hamiltonian is solvable by the Bethe ansatz [136, 137].

It is convenient to write $\psi_j(t) = \sqrt{N_j(t)}e^{i\theta_j(t)}$, where N_j and θ_j are the number of atoms in and the condensate phase of sublevel j, respectively. Non-trivial dynamics of the spinor system occurs in a reduced two-dimensional space Ω_{2D} with coordinates ϕ and ρ_0, for a fixed N and M. Here, $\phi = \theta_1 + \theta_{-1} - 2\theta_0$, where $\phi \in [-\pi, \pi]$ and $\phi = \pm\pi$ are identical; and $\rho_0 = N_0/N$ is the fraction of atoms in the $j = 0$ sublevel. In these coordinates, the system obeys the "single-particle" classical Hamiltonian [89]

$$h_{\text{spin}}(\phi, \rho_0) = c\rho_0 \left[(1 - \rho_0) + \sqrt{(1 - \rho_0)^2 - m^2} \cos\phi\right] + q(1 - \rho_0), \qquad (4.37)$$

where the coupling strength $c = g_2 N \int d^3r \, |\Phi(\vec{r})|^4$ is N dependent, g_2 is the spin-changing atom-atom interaction strength, the term $q(1 - \rho_0)$ describes atomic level shifts with controllable strength q (in essence due to the quadratic Zeeman interaction) and the conserved unit-magnetization $m = M/N$.
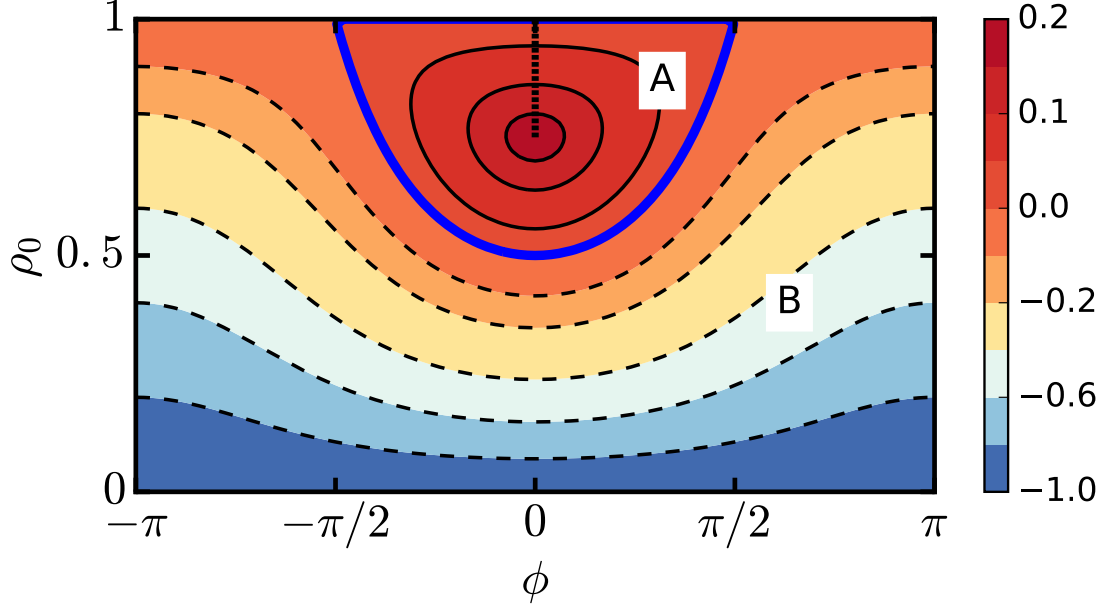
Figure 4.6: Equal-energy contours in the phase space (ϕ, ρ_0) of an antiferromagnetic spin-1 condensate in the single-mode and mean-field approximations. The magnetization $M = 0$, $q = -1$, and $c = 1$. The phase space is geometrically equivalent to a sphere as the edges $\phi = -\pi$ and π are equivalent and the lines $\rho_0 = 1$ and 0 are identified to the north and south pole, respectively. The thick solid blue line is the separatrix (S) that divides the phase space into regions A and B. The saddle point is located at the north pole $\rho_0 = 1$. (Note that the planar projection of the sphere incorrectly suggests that this point is a line segment.) In region A, the action-angle coordinate φ_1 is zero along the black dotted line, while in region B it is zero on $\phi = \pm\pi$. The color map is nonlinear in order to better visualize the equal-energy contours.

Here, we will only consider a condensate with antiferromagnetic $c > 0$ interactions and assume $m = 0$. Figure 4.6 shows equal-energy contours of $h_{\mathrm{spin}}(\phi, \rho_0)$ for a representative q in $(-2c, 0)$. The Hamiltonian then has a saddle point at the north pole $\rho_0 = 1$ and $h_{\mathrm{spin}}(\phi, \rho_0) \sim (1 - \rho_0)\{c(1 + \cos\phi) + q\}$ with a linear energy dependence for small positive $1 - \rho_0$. The slope, given in $\{\cdots\}$, changes sign twice when ϕ goes from 0 to 2π. Unlike the pendulum and double-well systems, there is only one separatrix S, which divides the phase space into regions A and B with rotation and bounded motion, respectively. The expression for $\rho_0(t)$ along a general trajectory is given in Appendix A.3. The solution along the separatrix that is symmetric about $t = 0$ is

$$\rho_{0,S}(t) = 1 - (1 - y_{1,S})\operatorname{sech}^2(\Omega t), \tag{4.38}$$

where $y_{1,S} = |q|/(2c)$ and $\Omega = \sqrt{2|q|c(1 - y_{1,S})}$. By solving $h_{\mathrm{spin}}(\phi_S(t), \rho_{0,S}(t)) = 0$ the corresponding $\phi_S(t)$ can be found.

We prepare the system in the mean-field ground state for $q > 0$, i.e., $\rho_0 = 1$ or equivalently $(\psi_{+1}, \psi_0, \psi_{-1}) = (0, \sqrt{N}, 0)$. The initial Wigner distribution is

$$W_0(\psi_j, \psi_j^*) = \frac{8}{\pi^3} e^{-2|\psi_{-1}|^2 - 2|\psi_0 - \sqrt{N}|^2 - 2|\psi_{+1}|^2}, \tag{4.39}$$

where $j \in \{+1, 0, -1\}$, corresponding to a coherent state for sublevel $j = 0$ with a mean atom number N and zero phase, and vacuum states for sublevels $j = \pm 1$. The probability measure for the distribution is $\prod_j d\psi_j^* d\psi_j$.

The parameter q is then quenched to a value between $-2c$ and 0 at time $t = 0$ and the system becomes dynamically unstable. Using Eq. 4.15 with two contributing

regions and one separatrix, the average $\langle \rho_0(t) \rangle$ long after the quench is given by

$$\lim_{t \to \infty} \langle \rho_0(t) \rangle \equiv \langle \rho_0(\infty) \rangle \sim 1 - \langle \varpi \rangle \frac{1 - y_{1,S}}{\pi \Omega}, \tag{4.40}$$

where we used the indicator functions $\chi_A(S) = \chi_B(S) = 1$ and defined auxiliary frequency ϖ that is now ω_1 in both regions with average $\langle \varpi \rangle = \langle \omega_1 \rangle_A + \langle \omega_1 \rangle_B$. In Appendix A.3.1, we show that $\langle \varpi \rangle \sim 2\pi\Omega/\ln(16N)$. The quantum correction to the long-time value of $\langle \rho_0(t) \rangle$ is, again, $O(1/\ln N)$.

Figure 4.7(a) shows $\langle \rho_0(\infty) \rangle$ as a function of q/c for $q \in (-2c, 0)$ and fixed atom number $N = 1000$. The analytical expression of $\langle \rho_0(\infty) \rangle$ with $\varpi = 2\pi\Omega/\ln(16N)$ gives a straight line. The figure also shows the predictions from numerical TWA for the same parameters. For small negative q, the two curves differ appreciably. We can reproduce the numerical TWA results when we replace $\langle \varpi \rangle$ in Eq. 4.40 by its numerical value as obtained from sampling the initial Wigner distribution. For $|q|/c$ much smaller than the scale of our figure, however, the $\langle \rho_0(\infty) \rangle$ from the numerical TWA and that based on computing $\langle \varpi \rangle$ from sampling still differ. We will return to this issue later on in this section.

The time evolution of $\langle \rho_0(t) \rangle$ is again calculated from Eq. 4.27. The dominant contribution to the expectation value is from the trajectories with the action-angle coordinate $\varphi_1(0) \approx 0$ (see Appendix A.3.2 for a formal justification). Hence, we can set $\varphi_1(0) = 0$ and, with $\alpha_A(S) = \alpha_B(S) = \pi$, find

$$\langle \rho_0(t) \rangle \sim 1 + \sum_{R=A,B} \sum_{m=-\infty}^{\infty} (-1)^m \left\langle \omega_1 \mathfrak{D}_S(m\omega_1) e^{im\omega_1 t} \right\rangle_R, \tag{4.41}$$

where $\mathfrak{D}_S(x)$ is the Fourier transform of $\rho_{0,S}(t)$. As in the previous section, we define the distribution function $\mathcal{F}(\varpi)$ with $\varpi = \omega_1$ in both regions. It is approximately

Gaussian with mean $\mu = \langle \varpi \rangle$ and width $\sigma \ll \mu$ (see Appendix A.3). Then, in a manner similar to that used to find Eq. 4.30, we derive

$$\langle \rho_0(t) \rangle \sim \langle \rho_0(\infty) \rangle - (1 - y_{1,S}) \sum_{m=1}^{\infty} (-1)^m \frac{m \mu^2 \cos(m \mu t)}{\Omega^2 \sinh[m \mu \pi / (2\Omega)]} e^{-m^2 \sigma^2 t^2 / 2} . \qquad (4.42)$$

Figure 4.7(b) shows the typical behavior of $\langle \rho_0(t) \rangle$ as a function of time. For long times, the evolution is a damped sinusoid oscillating around its asymptotic value, as only one term in the sum significantly contributes. For shorter times, the evolution is more complex and multiple terms are important. The numerical TWA simulations are in good agreement with our analytical expression.
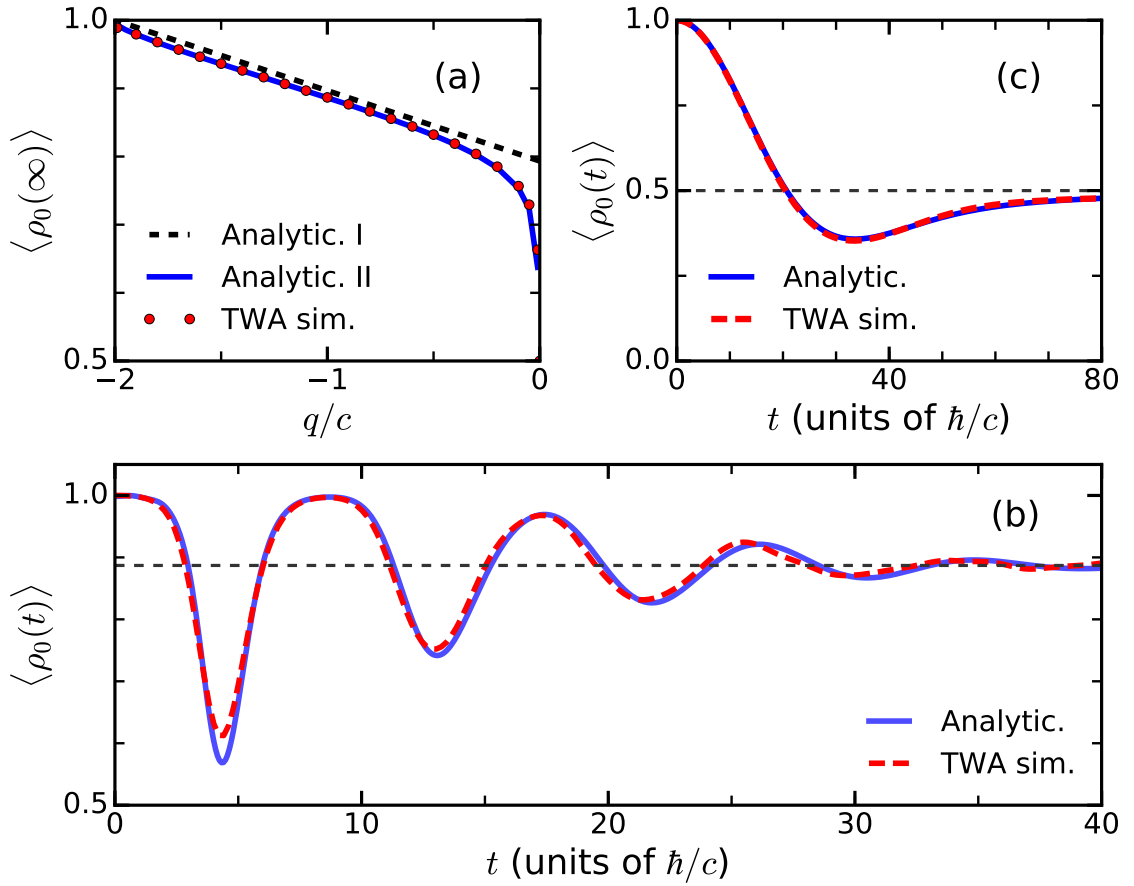

Figure 4.7: Long-time expectation values and time dynamics of a spin-1 BEC in SMA and TWA after an initial (polar) state with all atoms in spin projection zero

is quenched to a dynamically unstable point with $q < 0$. The number of atoms $N = 1000$. Panel (a) shows the long-time expectation value of the fraction of atoms in spin projection zero, $\langle \rho_0(\infty) \rangle$, as a function of q/c. The dashed black line and solid blue curve follow from Eq. 4.40 with mean $\mu \equiv \langle \varpi \rangle$ given by our analytical result and a numerical value as determined from sampling the initial Wigner distribution, respectively. Numerical TWA simulations correspond to the red circles. Panel (b) shows the time evolution of $\langle \rho_0(t) \rangle$ for $q/c = -1$. The solid blue and dashed red curves are obtained from Eq. 4.42 and numerical TWA simulations, respectively. For the solid blue line, the mean μ and width σ are obtained by numerical sampling the initial Wigner distribution. Finally, panel (c) shows the time evolution of $\langle \rho_0(t) \rangle$ for the special case where $q/c = 0$. The solid blue curve corresponds to Eq. 4.43, while the nearly-indistinguishable dashed red curve is from numerical TWA simulations. The horizontal dashed lines in panels (b) and (c) are the long-time values.

At $q = 0$, the Hamiltonian $h_{\text{spin}}(\phi, \rho_0)$ has a degenerate line of saddle points along $\phi = \pi$, instead of a single saddle point. The system is then critical and the formalism described so far can not be applied. Nevertheless, we show in Appendix A.3.3 that

$$\langle \rho_0(t) \rangle \sim 1 - \alpha t \, F(\alpha t), \tag{4.43}$$

where $\alpha = c \sqrt{2/N}$ and $F(x)$ is the Dawson integral [119]. Figure 4.7(c) shows this evolution as a function of time. The motion seems overdamped with little oscillatory behavior. Agreement with TWA simulation results is very good.

4.11   Conclusion and outlook

We have analytically studied the time dynamics of two integrable bosonic systems within the truncated Wigner approximation (TWA) when they become dynamically unstable after a quench in a system parameter. The initial Wigner distribution is then centered around a saddle point. We considered a Bose-Einstein condensate (BEC) in a symmetric double-well potential and an antiferromagnetic spinor BEC in the single-mode approximation. Using action-angle variables and the concept of phase-space mixing, we derived the long-time expectation value of observables, Eq. 4.15. We also derived the relaxation dynamics of the expectation value as given in Eq. 4.27. We used a simple pendulum as a guide for these derivations.

The time dynamics of the expectation value of an observable is determined by the distribution of frequency ω_1 of the classical, periodic trajectories. The evaluation of the time dynamics simplified due to the symmetries of the Hamiltonian and the initial Wigner distribution. These symmetries also motivated the definition of an auxiliary frequency ϖ, which has a simple relationship to ω_1. For the two bosonic systems, when the initial state is a coherent state of N atoms the mean of ϖ is $O(1/\ln N)$. Hence, the deviation of the long-time expectation value from its classical value at the saddle point is $O(1/\ln N)$. The mean determines the typical time scale of the oscillations in the time evolution. The width of ϖ is $O[1/(\ln N)^2]$ and determines the relaxation rate. Furthermore, we obtained their explicit dependence on external parameters.

Although we only considered a representative observable for each system, the

time dynamics of observables that quantify (condensate) phase or squeezing can be computed using our formalism. Our analysis is also directly applicable to other integrable systems with a single saddle point in phase space, such as a (anti-) ferromagnetic spinor BEC with nonzero magnetization and a BEC in an asymmetric double-well potential. The formalism can be generalized to integrable Hamiltonians with multiple saddle points, for example, the Lipkin-Meshkov-Glick model [138].

We finish with a brief discussion on the exact quantum dynamics for the few-mode systems and its comparison with the TWA, which motivates the next chapter. Figure 4.8 shows a comparison for a BEC in a double-well potential. We find that the TWA deviates from the quantum evolution after the first oscillation. In fact, this is consistent with the the quantum break time or Ehrenfest time [139], which is determined by the anharmonicity in the energy-level spacing [140] and scales as $O(\ln N)$ for the double-well system. Moreover, similar deviations occur in the dynamics of a pendulum and a spinor BEC. The deviation of the TWA from the exact quantum dynamics is the motivation for the next chapter, where we study corrections beyond the TWA, which arise because of interference of classical paths.
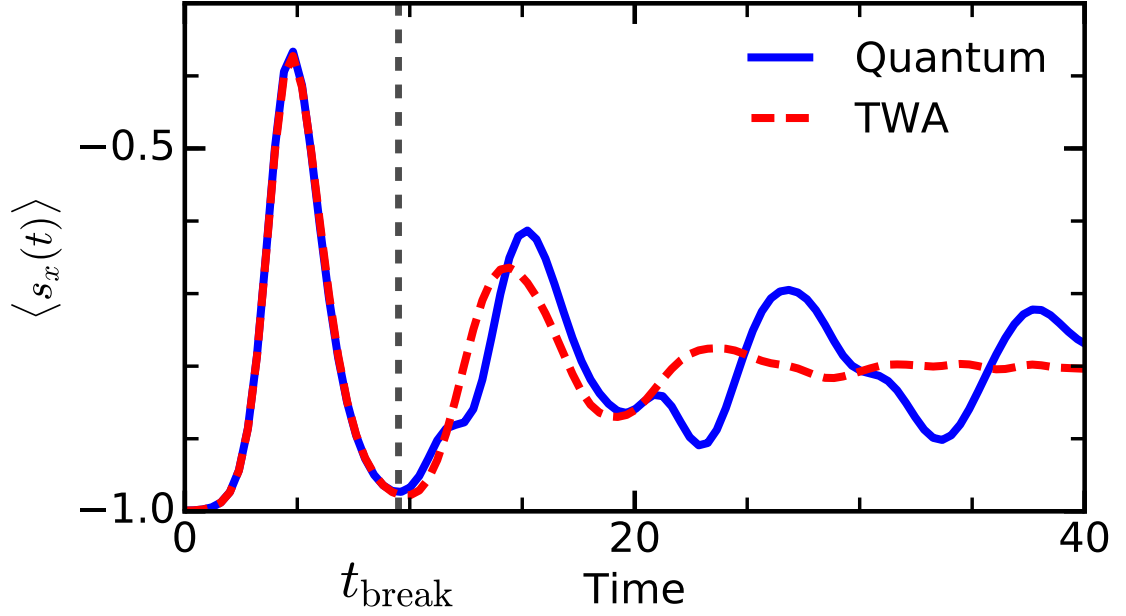
Figure 4.8: Comparison of the TWA and the quantum evolution of an observable for a BEC in a double-well potential. The blue solid curve is the exact quantum evolution of the expectation value of the observable s_x, which is defined in the text. The red dashed curve is the TWA result, which deviates from the quantum evolution after the quantum break time t_{break}. For the plots, the parameter $\Lambda = 2$ and the number of atoms is 1000.

Chapter 5: Non-perturbative effects beyond the truncated Wigner approximation

5.1 Introduction

The crucial difference between classical probability theory and quantum mechanics is the method of computing the transition probability between an initial and a final state. In classical probability theory, the transition probability is the sum over probabilities of the paths connecting the two states. In contrast, in quantum mechanics, it is obtained by first summing the probability amplitudes of all the connecting paths and then squaring the sum. This procedure leads to interference of probability amplitudes, a feature absent in the classical theory. The summation over probability amplitudes is most patent in the path integral formulation of quantum mechanics, where the probability amplitude of a transition is an integral of $e^{iS/\hbar}$ over all the paths (typically in the configuration space) and S is the classical action along a path [74]. An archetypal example of the phenomenon of interference is a double-slit experiment in which a beam of particles after passing through two slits forms an oscillating intensity pattern on a screen. This pattern, which is not explainable by a classical theory, results from the interference of alternate paths

that a particle can take by passing through either one of the slits.

An example in the context of many-body physics, where interference of classical paths becomes important is the phenomenon of weak localization, a precursor to Anderson localization [141]. Weak localization occurs in disordered electron systems with static impurities, which scatter electrons. These impurities are dilute, i.e., the typical distance between impurities is much greater than the wavelength of electrons. The interference of electron paths, which can be represented by sequences of impurities from which an electron scatters, with their time-reversal counterparts leads to observable consequences, like reduction of conductivity.

In this chapter, we will study the role of interference of classical paths in boson dynamics. First, we derive an exact relation for the Green's function of a Wigner function in Sec. 5.2. We then approximate this Green's function in the semiclassical regime in Sec. 5.3. As we saw in the previous chapter, the truncated Wigner approximation (TWA) is essentially a classical method as the propagation of the Wigner function is purely classical. In fact, in Sec. 5.3.1 we find that when the interference terms are ignored from the semiclassical approximation, we recover the TWA. Subsequently, we apply the semiclassical formalism to a nonlinear oscillator in Sec. 5.4. The quantum dynamics of this oscillator displays periodic collapse and revival of an initial coherent state. The TWA accurately describes the initial collapse but not the revival. The semiclassical approximation, however, can reproduce the periodic collapse and revival. Finally, we conclude in Sec. 5.5.

5.2   Green's function of the Wigner function

In this section, we derive an exact expression for the propagation of the Wigner function for a bosonic system. Let the number of modes of the system be finite, and d in number, with $\hat{a}_j$ and $\hat{a}_j^\dagger$ as the annihilation and creation operator of mode j, respectively. They satisfy the commutation relations $[a_j, a_k^\dagger] = \delta_{jk}$, where δ_{jk} is the Kronecker δ function. Consider the quadrature operators $\hat{x}_j = \sqrt{\frac{\hbar}{2}}(\hat{a}_j + \hat{a}_j^\dagger)$ and $\hat{p}_j = -i\sqrt{\frac{\hbar}{2}}(\hat{a}_j - \hat{a}_j^\dagger)$ satisfying the canonical commutation relations $[\hat{x}_j, \hat{p}_k] = i\hbar\delta_{jk}$. Their classical limits x_j and p_j is a set of canonical coordinates that span a phase space of dimension $2d$. The eigenstates of the quadrature operators $\hat{x}_j$ satisfy $\hat{x}_j |\mathbf{x}\rangle = x_j |\mathbf{x}\rangle$ for all $j \in \{1, \cdots, d\}$, where $\mathbf{x} = (x_1, x_2, \dots, x_d)$. They form a complete basis and $\int d\mathbf{x} \, |\mathbf{x}\rangle \langle \mathbf{x}| = 1$, where the integral is over $\mathbb{R}^d$ and we chose the inner products to satisfy $\langle \mathbf{x}'|\mathbf{x}\rangle = \delta(\mathbf{x} - \mathbf{x}')$. Moreover, similar statements apply for the quadrature operators $\hat{p}_j$ and we denote their eigenvalues by $\mathbf{p} = (p_1, p_2, \dots, p_d)$. Throughout this chapter, we will refer to the eigenvalues $\mathbf{x}$ and $\mathbf{p}$, which represent a phase-space point, as position and momentum, respectively.

Let the Wigner function at time t be $W(\mathbf{r}, t)$, where $\mathbf{r} = (\mathbf{x}, \mathbf{p})$ is a phase-space point. The Wigner function of a pure state $|\psi(t)\rangle$ at time t is

$$W(\mathbf{r}, t) = \frac{1}{(2\pi\hbar)^d} \int d\mathbf{q} \, \langle \mathbf{x} + \tfrac{1}{2}\mathbf{q}|\psi(t)\rangle \langle \psi(t)|\mathbf{x} - \tfrac{1}{2}\mathbf{q}\rangle \, e^{-i\mathbf{p}\cdot\mathbf{q}/\hbar}, \qquad (5.1)$$

where the integral is over the configuration space $\mathbb{R}^d$. Hereafter, we set $\hbar = 1$ for notational simplicity. We define the Green's function $G(\mathbf{r}_f, \mathbf{r}_i, t)$ of the Wigner

function by

$$W(\mathbf{r}_f, t) = \int d\mathbf{r}_i\, G(\mathbf{r}_f, \mathbf{r}_i, t) W(\mathbf{r}_i, 0), \tag{5.2}$$

for $t \geq 0$ with the initial condition $G(\mathbf{r}_f, \mathbf{r}_i, 0) = \delta(\mathbf{r}_f - \mathbf{r}_i)$.

Now, $|\psi(t)\rangle = U(t)|\psi_0\rangle$, where $U(t)$ is the time-evolution operator and $|\psi_0\rangle$ is the initial state. We insert in Eq. 5.1 the resolutions of identity in the position basis, $\int d\mathbf{y}_1 |\mathbf{y}_1\rangle \langle \mathbf{y}_1|$ and $\int d\mathbf{y}_2 |\mathbf{y}_2\rangle \langle \mathbf{y}_2|$, to find

$$W(\mathbf{r}_f, t) = \frac{1}{(2\pi)^d} \int d\mathbf{q}d\mathbf{y}_1 d\mathbf{y}_2\, K\left(\mathbf{x}_f + \tfrac{1}{2}\mathbf{q}, \mathbf{y}_1, t\right) \psi_0(\mathbf{y}_1) K^*\left(\mathbf{x}_f - \tfrac{1}{2}\mathbf{q}, \mathbf{y}_2, t\right) \psi_0^*(\mathbf{y}_2) e^{-i\mathbf{p}_f \cdot \mathbf{q}}, \tag{5.3}$$

where the propagator in the configuration space $K(\mathbf{x}_f, \mathbf{x}_i, t) = \langle \mathbf{x}_f | U(t) | \mathbf{x}_i \rangle$ and $\psi_0(\mathbf{x}) = \langle \mathbf{x} | \psi_0 \rangle$. We would like to express the initial condition on the right-hand side, $\psi_0(\mathbf{y}_1)\psi_0^*(\mathbf{y}_2)$, in terms of the initial Wigner distribution. To this end, we multiply Eq. 5.1 evaluated at $t = 0$ by $e^{i\mathbf{p}_i \cdot \mathbf{q}'}$ and integrate over $\mathbf{p}_i$ to find

$$\int d\mathbf{p}_i\, e^{i\mathbf{p}_i \cdot \mathbf{q}'} W(\mathbf{r}_i, 0) = \psi_0\left(\mathbf{x}_i + \tfrac{1}{2}\mathbf{q}'\right) \psi_0^*\left(\mathbf{x}_i - \tfrac{1}{2}\mathbf{q}'\right). \tag{5.4}$$

We substitute this expression in Eq. 5.3 and identify $\mathbf{y}_1 = \mathbf{x}_i + \tfrac{1}{2}\mathbf{q}'$ and $\mathbf{y}_2 = \mathbf{x}_i - \tfrac{1}{2}\mathbf{q}'$. From the definition of Green's function in Eq. 5.2 we find

$$G(\mathbf{r}_f, \mathbf{r}_i, t) = \frac{1}{(2\pi)^d} \int d\mathbf{q}d\mathbf{q}'\, K\left(\mathbf{x}_f + \tfrac{1}{2}\mathbf{q}, \mathbf{x}_i + \tfrac{1}{2}\mathbf{q}', t\right) K^*\left(\mathbf{x}_f - \tfrac{1}{2}\mathbf{q}, \mathbf{x}_i - \tfrac{1}{2}\mathbf{q}', t\right) e^{-i\mathbf{p}_f \cdot \mathbf{q} + i\mathbf{p}_i \cdot \mathbf{q}'}. \tag{5.5}$$

Thus, the exact Green's function of the Wigner distribution involves the product of two propagators in the configuration space. We expect that, similar to the calculation of a transition probability, where squaring of the sum of probability amplitudes leads to interference; in this case, the product of the two propagators will have interference terms. As far as I know, this expression was first derived by Marinov [142]

and has been used for semiclassical numerical studies of scattering in molecular potentials [143].

5.3 Semiclassical approximation of the Green's function

We now proceed to calculate a semiclassical approximation of $G(\mathbf{r}_f, \mathbf{r}_i, t)$. A quantum system is said to be in the semiclassical regime when the typical action that appears in the path integral is much greater than $\hbar$. For a bosonic mode, this is the case when its occupation number is large. The semiclassical approximation of the propagator, also known as the van Vleck-Gutzwiller propagator, is

$$K_{\mathrm{SC}}(\mathbf{x}_f, \mathbf{x}_i, t) = \sum_c \frac{e^{-i\mu^c\pi/2}}{(2\pi i)^{d/2}} \sqrt{\left| \det\left(\frac{\partial^2 S^c(\mathbf{x}_f, \mathbf{x}_i, t)}{\partial \mathbf{x}_f \partial \mathbf{x}_i} \right) \right|} e^{iS^c(\mathbf{x}_f, \mathbf{x}_i, t)}, \qquad (5.6)$$

where the sum is over all classical paths, indexed by c, that start from position $\mathbf{x}_i$ and reach $\mathbf{x}_f$ in time t, $2d$ is the dimension of the phase space and μ^c is the Maslov index [1]. The action $S^c(\mathbf{x}_f, \mathbf{x}_i, t) = \int_0^t d\tau\, L[\mathbf{x}^c(\tau), d\mathbf{x}^c(\tau)/d\tau]$, where L is the Lagrangian and $\mathbf{x}^c(\tau)$ is the position of a classical path as a function of time τ with $\mathbf{x}^c(0) = \mathbf{x}_i$ and $\mathbf{x}^c(t) = \mathbf{x}_f$. The prefactor under the square root is the absolute value of the determinant of a $d \times d$ matrix $\partial^2 S^c(\mathbf{x}_f, \mathbf{x}_i, t)/(\partial \mathbf{x}_f \partial \mathbf{x}_i)$. The van Vleck-Gutzwiller propagator is derived by starting from the path integral representation of the propagator. Then using the stationary-phase approximation with the stationary points being the classical paths satisfying the boundary conditions; and integrating quadratic fluctuations around these paths, one arrives at the van Vleck-Gutzwiller

---

[1] Roughly speaking, the Maslov index of a classical path is the number of turning points along the path.

propagator [144, 145]. It is an important tool in quantum chaos and is the basis for the derivation of the Gutzwiller trace formula [146].

Substitution of van Vleck-Gutzwiller propagator in Eq. 5.5 yields the semi-classical approximation to the Green's function

$$
G_{\text{SC}}(\mathbf{r}_f, \mathbf{r}_i, t) = \frac{1}{(2\pi)^{2d}} \int d\mathbf{q} d\mathbf{q}' \, e^{-i\mathbf{p}.\mathbf{q}+i\mathbf{p}'.\mathbf{q}'} \tag{5.7}
$$
$$
\times \sum_c \sqrt{\mathcal{D}^c(\mathbf{x}_f + \mathbf{q}/2, \mathbf{x}_i + \mathbf{q}'/2, t)} \, e^{iS^c(\mathbf{x}_f + \mathbf{q}/2, \mathbf{x}_i + \mathbf{q}'/2, t) - i\mu^c \pi/2}
$$
$$
\times \sum_{c'} \sqrt{\mathcal{D}^{c'}(\mathbf{x}_f - \mathbf{q}/2, \mathbf{x}_i - \mathbf{q}'/2, t)} \, e^{-iS^{c'}(\mathbf{x}_f - \mathbf{q}/2, \mathbf{x}_i - \mathbf{q}'/2, t) + i\mu^{c'} \pi/2},
$$

where $\mathcal{D}^c(\mathbf{x}_f, \mathbf{x}_i, t) = |\det[\partial^2 S^c(\mathbf{x}_f, \mathbf{x}_i, t)/(\partial \mathbf{x}_f \partial \mathbf{x}_i)]|$. Now we carry out a Taylor expansion of the action to find

$$
S^c\left(\mathbf{x}_f + \tfrac{1}{2}\mathbf{q}, \mathbf{x}_i + \tfrac{1}{2}\mathbf{q}', t\right) \approx S^c(\mathbf{x}_f, \mathbf{x}_i, t) + \frac{\mathbf{p}_f^c.\mathbf{q}}{2} - \frac{\mathbf{p}_i^c.\mathbf{q}'}{2}, \tag{5.8}
$$

where we have used the results derived in Appendix B.1 $\partial S^c(\mathbf{x}_f, \mathbf{x}_i, t)/\partial \mathbf{x}_i = -\mathbf{p}_i^c$ and $\partial S^c(\mathbf{x}_f, \mathbf{x}_i, t)/\partial \mathbf{x}_f = \mathbf{p}_f^c$, where $\mathbf{p}_i^c$ and $\mathbf{p}_f^c$ are the initial and final momentum, respectively, of the classical path along which the action is computed. Furthermore, we approximate

$$
\mathcal{D}^c(\mathbf{x}_f + \mathbf{q}/2, \mathbf{x}_i + \mathbf{q}'/2, t), \, \mathcal{D}^c(\mathbf{x}_f - \mathbf{q}/2, \mathbf{x}_i - \mathbf{q}'/2, t) \approx \mathcal{D}^c(\mathbf{x}_f, \mathbf{x}_i, t). \tag{5.9}
$$

Substituting expressions for S^c and $\mathcal{D}^c$ in Eq. 5.10 and carrying out the integral over $\mathbf{q}$ and $\mathbf{q}'$, we find

$$
G_{\text{SC}}(\mathbf{r}_f, \mathbf{r}_i, t) = \sum_{c,c'} \sqrt{\mathcal{D}^c \mathcal{D}^{c'}} e^{iS^c - iS^{c'} - i(\mu^c - \mu^{c'})\pi/2} \delta\left[\mathbf{p}_f - \tfrac{1}{2}(\mathbf{p}_f^c + \mathbf{p}_f^{c'})\right] \delta\left[\mathbf{p}_i - \tfrac{1}{2}(\mathbf{p}_i^c + \mathbf{p}_i^{c'})\right],
$$

$$
\tag{5.10}
$$

where, for clarity, we have suppressed the dependence of S^c, $\mathcal{D}^c$, etc., on $\mathbf{x}_i$, $\mathbf{x}_f$ and t. This is the main result of this chapter and relates the Green's function of the Wigner distribution to a double sum over classical paths connecting positions $\mathbf{x}_i$ and $\mathbf{x}_f$ in time t. A similar formalism has been used in the study of transport of electrons in ballistic chaotic cavities [147].

5.3.1 The truncated Wigner approximation

We claim that the diagonal part of the sum in Eq. 5.10, i.e., when $c = c'$, is the classical Liouville propagator, which is the Green's function within the TWA. In other words, the TWA neglects the terms arising from the interference of classical paths. A clear way of proving this assertion is to consider the evolution of an observable $\mathcal{O}(\mathbf{x}, \mathbf{p})$. Let $W_0(\mathbf{r})$ be the initial Wigner function. Then the expectation value of the observable at a later time t is (see also Eq. 4.1)

$$\langle \mathcal{O}(t) \rangle \equiv \langle \mathcal{O}(\mathbf{x}(t), \mathbf{p}(t)) \rangle = \int d\mathbf{x}_f d\mathbf{p}_f \, \mathcal{O}(\mathbf{x}_f, \mathbf{p}_f) W(\mathbf{r}_f, t)$$

$$= \int d\mathbf{x}_f d\mathbf{x}_i d\mathbf{p}_f d\mathbf{p}_i \, \mathcal{O}(\mathbf{x}_f, \mathbf{p}_f) G(\mathbf{r}_f, \mathbf{r}_i, t) W_0(\mathbf{r}_i), \quad (5.11)$$

where we used Eq. 5.2. The diagonal part of the Green's function of Eq. 5.10 is

$$G_{\text{TWA}}(\mathbf{r}_f, \mathbf{r}_i, t) = \sum_c \mathcal{D}^c(\mathbf{x}_f, \mathbf{x}_i, t) \, \delta \left(\mathbf{p}_f - \mathbf{p}_f^c \right) \delta \left(\mathbf{p}_i - \mathbf{p}_i^c \right). \quad (5.12)$$

We substitute this expression in Eq. 5.11 and integrate over $\mathbf{p}_f$ to find that the claimed expectation value within TWA is

$$\langle \mathcal{O}(t) \rangle_{\text{TWA}} = \int d\mathbf{x}_f d\mathbf{x}_i d\mathbf{p}_i \, \mathcal{O}(\mathbf{x}_f, \mathbf{p}_f^c) \sum_c \mathcal{D}^c(\mathbf{x}_f, \mathbf{x}_i, t) \, \delta \left(\mathbf{p}_i - \mathbf{p}_i^c \right) W_0(\mathbf{x}_i, \mathbf{p}_i). \quad (5.13)$$

Now, we would like the integration measure to depend only on the initial conditions, i.e., $d\mathbf{x}_i d\mathbf{p}_i$. To this end, we show in Appendix B.2 that

$$\delta[\mathbf{x}_f(\mathbf{x}_i, \mathbf{p}_i, t) - \mathbf{x}_f^c] = \sum_c \mathcal{D}^c(\mathbf{x}_f, \mathbf{x}_i, t)\, \delta\left(\mathbf{p}_i - \mathbf{p}_i^c\right), \qquad (5.14)$$

where the function $\mathbf{x}_f(\mathbf{x}_i, \mathbf{p}_i, t)$ is the position at time t of a unique classical trajectory that starts from the phase-space point $(\mathbf{x}_i, \mathbf{p}_i)$ at time 0. The sum on the right-hand side is over classical paths that connect $\mathbf{x}_i$ to $\mathbf{x}_f^c$ in time t and $\mathbf{p}_i^c$ is the initial momentum of such a path. Using this observation and after integrating over $\mathbf{x}_f$, Eq. 5.13 becomes

$$\langle \mathcal{O}(t) \rangle_{\text{TWA}} = \int d\mathbf{x}_i d\mathbf{p}_i\, \mathcal{O}(\mathbf{x}^c(t), \mathbf{p}^c(t)) W_0(\mathbf{x}_i, \mathbf{p}_i),$$

where $(\mathbf{x}^c(t), \mathbf{p}^c(t))$ is the classical path satisfying the initial conditions $\mathbf{x}^c(0) = \mathbf{x}_i$ and $\mathbf{p}^c(0) = \mathbf{p}_i$. Thus, we have arrived at an expression that is in accordance with the TWA (see Eq. 4.1), thereby proving the assertion.

It is pertinent to put the semiclassical formalism in context of the work by A. Polkovnikov [109, 115] on boson dynamics beyond the TWA. He systematically calculated perturbative corrections to TWA; however, the analysis does not yield the interference of classical paths, which is a non-perturbative effect. In particular, a nonlinear oscillator was studied whose quantum dynamics exhibits collapse and revival. Although the perturbative analysis describes the initial collapse, with increasing accuracy with the order of the perturbation, it fails to describe revivals in the system. The classical version of this oscillator was used to describe the phase-space mixing in Sec. 4.5. Next, we study the oscillator's quantum dynamics and compare it with its TWA and semiclassical dynamics.

5.4 Case study: A nonlinear oscillator

The quantum Hamiltonian of the single-mode nonlinear oscillator is

$$H_{\text{NO}} = \frac{U}{2}\hat{a}^\dagger\hat{a}^\dagger\hat{a}\hat{a}, \tag{5.15}$$

where U is the interaction strength and $\hat{a}(\hat{a}^\dagger)$ is the annihilation (creation) operator of the associated bosonic mode. As the number operator $\hat{a}^\dagger\hat{a}$ commutes with H_{NO}, the energy eigenstates are $|n\rangle$ with eigen-energies $E_n = Un(n-1)/2$, where n is the occupation number of the mode. Decomposing an initial state $|\psi_0\rangle = \sum_{n=0}^{\infty} c_n |n\rangle$ and noting that $n(n-1)/2$ is an integer, we can immediately see that the initial state periodically revives, i.e., $|\psi(t)\rangle = |\psi_0\rangle$ when t is an integer multiple of period $t_{\text{rev}} = 2\pi/U$.

The nonlinear oscillator has been studied in experiments with a BEC in an optical lattice [148]. When the tunneling between the lattice sites is switched off, the dynamics of a single site is described by the Hamiltonian in Eq. 5.15. The initial state is a coherent state, $|\alpha\rangle = e^{-|\alpha|^2/2}\sum_n \alpha^n/\sqrt{n!}\,|n\rangle$, which is a superposition of number states. The quantum state at time t is

$$|\psi(t)\rangle = e^{-|\alpha|^2/2}\sum_n \frac{\alpha^n}{\sqrt{n!}}e^{-iUn(n-1)t/2}\,|n\rangle. \tag{5.16}$$

The experiment measured the expectation value of $\hat{a}$ from the interference pattern formed by releasing the atoms from the lattice. It evolves as

$$\langle\psi(t)|\,\hat{a}\,|\psi(t)\rangle = \alpha e^{|\alpha|^2(e^{-iUt}-1)}, \tag{5.17}$$

which collapses and revives with a period t_{rev} as shown in Fig. 5.1. At short times,
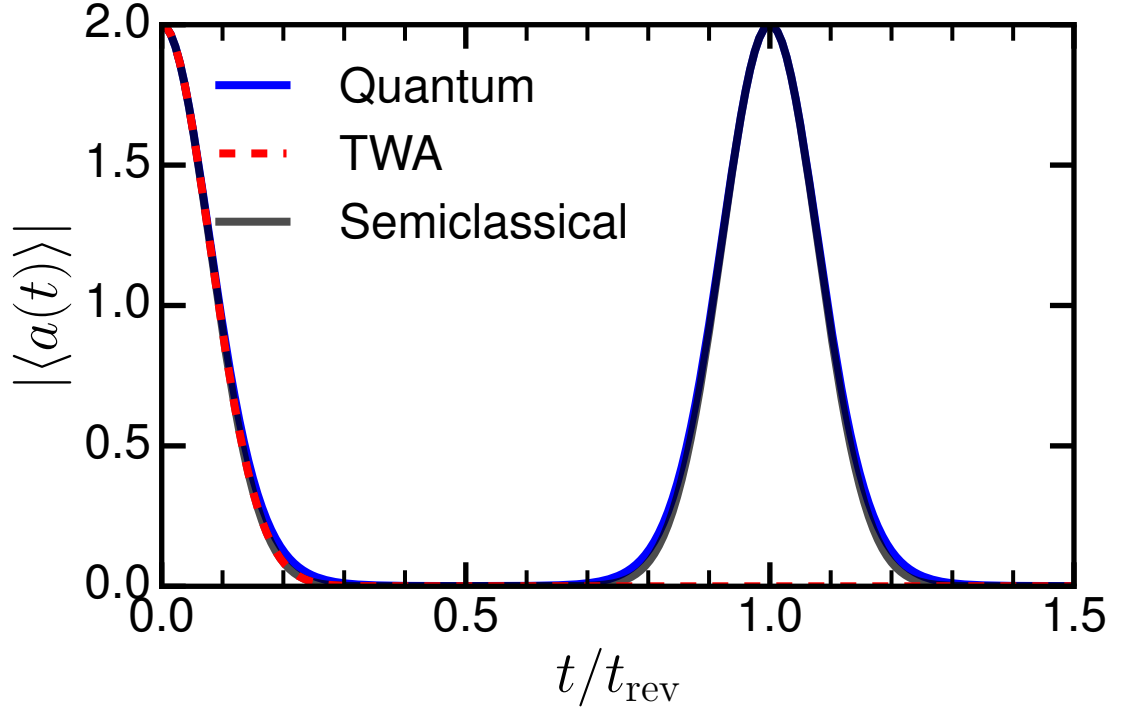
Figure 5.1: Collapse and revival in a nonlinear oscillator. The plot shows $|\langle a(t) \rangle|$ as a function of time for an initial coherent state whose mean atom number is 4. The quantum dynamics shows collapse and revival of $|\langle a(t) \rangle|$ with revival time t_{rev}. The TWA result, Eq. 5.22, closely replicates the first collapse but shows no revival. On the other hand, the semiclassical approximation, Eq. 5.23, agrees well with the quantum evolution for all times.

$Ut \ll 1$,

$$\langle \psi(t)| \, \hat{a} \, |\psi(t)\rangle \approx \alpha e^{-|\alpha|^2 U^2 t^2/2 - iU|\alpha|^2 t}. \tag{5.18}$$

Therefore, the time scale of collapse is $1/(U\sqrt{N})$, where $N = |\alpha|^2$ is the average number of atoms of the coherent state. This collapse and revival was observed in the experiment. In addition, the Hamiltonian has also been implemented using the Kerr nonlinearity for photons [149]. Besides the observation of collapse and revival of a coherent state, the experiment also measured the Husimi distribution.

Next, we study the time dynamics of a coherent state of the nonlinear oscillator within the TWA.

5.4.1 Dynamics according to the TWA

To evaluate the TWA average of $a(t)$, we first need to describe the dynamics of the classical Hamiltonian corresponding to H_{NO} [2]. It is

$$\mathcal{H}_{\mathrm{NO}} = U(x^2 + p^2)^2/8. \tag{5.19}$$

Then the classical equations of motion are

$$\frac{dx}{dt} = \frac{\partial \mathcal{H}_{\mathrm{NO}}}{\partial p} = \frac{U}{2}\rho^2 p, \quad \frac{dp}{dt} = -\frac{\partial \mathcal{H}_{\mathrm{NO}}}{\partial x} = -\frac{U}{2}\rho^2 x, \tag{5.20}$$

where $\rho^2 = x^2 + p^2$. A classical path, with a frequency $\omega = U\rho^2/2$, lies on a circle in phase space, centered around the origin. The system is integrable as the phase space is two-dimensional and the energy is conserved. The angle of the action-angle

---

[2] We use $\hat{a}^\dagger \hat{a} = (\hat{x}^2 + \hat{p}^2 - 1)/2$ to find that $H_{\mathrm{NO}} = U/8 \times [(\hat{x}^2 + \hat{p}^2)^2 - 4(\hat{x}^2 + \hat{p}^2) + 3]$, which is Weyl ordered. We then replace $\hat{x}$, $\hat{p}$ by their classical limits to obtain $\mathcal{H}_{\mathrm{NO}}$, and ignore the constant and second term in the semiclassical limit $N \gg 1$.

coordinates is the polar angle φ measured in clockwise direction, the direction of motion. Using the definition $\omega = \partial\mathcal{H}_{\mathrm{NO}}/\partial I$, we find that the action coordinate $I = \rho^2/2$.

For concreteness, let the initial coherent state, with an occupation number $N \gg 1$, be centered along the p-axis, i.e., $\alpha = i\sqrt{N}$. Its Wigner function

$$W(x,p) = \frac{1}{\pi}e^{-x^2-(p-\sqrt{2N})^2}, \tag{5.21}$$

is centered at $(x,p) = (0, \sqrt{2N})$ and has the normalization $\int_{-\infty}^{\infty} dx dp\, W(x,p) = 1$. For the calculation of a TWA average, it is convenient to work in polar coordinates. We define the range of the polar angle φ as $(-\pi, \pi]$ and its zero to be along the p-axis. Then, the Wigner-Weyl transform of $\hat{a}(t)$ is $a(t) = [x(t)+ip(t)]/\sqrt{2} = i\rho e^{-i\varphi(t)}/\sqrt{2}$. It evolves as $a(t) = i\rho e^{-i\omega t+\varphi_0} = i\rho e^{-iU\rho^2 t/2+\varphi_0}$, where φ_0 is the initial angle and we used fact that $\omega = U\rho^2/2$. After writing the Wigner function in polar coordinates and integrating, we find

$$\langle a(t)\rangle_{\mathrm{TWA}} \approx i\int_0^\infty d\rho \int_{-\pi}^\pi d\varphi_0\, \rho^2 e^{-(\rho-\sqrt{2N})^2-2N\varphi_0^2-iU\rho^2 t/2}$$

$$\approx i\sqrt{N}e^{-U^2Nt^2/2-iUNt}, \tag{5.22}$$

which matches the initial collapse of the coherent state in Eq. 5.18 but has no subsequent revival. A comparison of Eq. 5.22 with the exact quantum result of 5.18 is shown in Fig. 5.1.

This result is expected from the discussion of phase-mixing in Sec. 4.5. Due to phase space mixing, the distribution function mixes uniformly in the angle φ. As $a(t) \propto e^{i\varphi(t)}$, its expectation value collapses. Furthermore, within the TWA, the

distribution function remains mixed, hence, there is no revival. This observation indicates that the quantum evolution somehow reverses phase mixing and revives the quantum state. In the next section, we find that applying the semiclassical formalism, which includes interference terms, indeed, leads to revival.

5.4.2 Dynamics according to semiclassical approximation

The classical paths, which lie on circles in the phase space, can be indexed by their winding number around the phase-space origin. Moreover, after a sufficiently long time there are multiple paths connecting two positions in a given time. This multiplicity is due to nonlinearity of the Hamiltonian and is absent for a harmonic oscillator.

The calculation of $\langle a(t) \rangle$ according to the semiclassical approximation is lengthy and has been relegated to Appendix B.4. Here, we list the main steps of the calculation:

1. The time evolution of an observable $\mathcal{O}(x, p)$ is given by Eq. 5.11 and we substitute $G(r_f, r_i, t)$ by its semiclassical approximation $G_{\mathrm{SC}}(r_f, r_i, t)$ as given in Eq. 5.10.

2. Now the action $S^c(x_f, x_i, t)$ (see Appendix B.3), hence $G_{\mathrm{SC}}(r_f, r_i, t)$, and the dynamics is simplest in action-angle coordinates. Therefore, we convert the integral over x_i, x_f, p_i and p_f in Eq. 5.11 into an integral over the initial and final angles φ_i and φ_f, respectively, and a double sum over winding numbers of the classical paths. We also express the observable, $G_{\mathrm{SC}}(r_f, r_i, t)$, and the

initial Wigner function in terms of φ_i, φ_f and winding numbers.

3. Next, we note that the classical motion in the phase space is restricted around an annulus of radius $\sqrt{2N}$ and width of $O(1)$. Then, $\mathcal{O}(x,p) \approx \mathcal{O}(\sqrt{2N}\sin\varphi, \sqrt{2N}\cos\varphi)$; in particular, $a(x,p) \approx i\sqrt{N}e^{-i\varphi}$. We make a more careful approximation for the initial Wigner function as it varies sharply with ρ.

4. Carrying out the integrals and taking in account the Maslov indices of the paths, we find the semiclassical approximation

$$\langle a(t) \rangle_{\text{SC}} = \sum_{v=-\infty}^{\infty} i\sqrt{N}e^{-iUNt}e^{-2N(\pi v - Ut/2)^2}. \tag{5.23}$$

The semiclassical expression $\langle a(t) \rangle_{\text{SC}}$ is invariant under the transformation $t \to t + 2\pi/U$ and $v \to v - 1$; hence, is periodic with time period $t_{\text{rev}} = 2\pi/U$. Moreover, $\langle a(t) \rangle_{\text{SC}}$ matches the collapse and revival of the exact quantum average $\langle \psi(t) | \hat{a} | \psi(t) \rangle$ (see Fig. 5.1), with a relative error of $O(1/\sqrt{N})$.

5.5   Conclusion and outlook

In this chapter, we studied quantum corrections to boson dynamics that are beyond the TWA. We derived, Eq. 5.10, a semiclassical approximation to the exact Green's function of the Wigner function Eq. 5.5. Crucially, the approximation preserves the quantum interference of trajectories. In fact, we showed that the formalism reduces to the TWA when the interference terms are ignored. Thereafter, we studied a single-mode nonlinear oscillator whose exact quantum dynamics exhibits collapse and revival of a quantum state. We studied the dynamics of an observ-

able of this oscillator both using the TWA and the semiclassical formalism. Within TWA, due to phase mixing, the expectation value of the observable collapses but there is no revival. The semiclassical approximation, however, matches the exact quantum dynamics.

The analysis of this chapter provides insight into when the TWA deviates from the exact quantum dynamics. It occurs after a time when classical trajectories start to interfere. For quantum systems whose classical limit is chaotic, this time is known as the quantum break time or the Ehrenfest time and has been shown to be proportional to the logarithm of the characteristic Lyapunov exponent [139, 150]. Finally, interference of paths explains the disagreement of the TWA with the quantum dynamics of the dynamically-unstable systems, which we studied in the previous chapter. The quantum break time in these cases is the mean of the time taken by trajectories to return to the saddle point, precisely the time when multiple classical paths, which obey the same boundary conditions, contribute significantly to the classical evolution.

Chapter 6:   Summary and outlook

Bose-Einstein condensates of ultracold atoms have been the subject of experimental and related theoretical studies since their first experimental realization in 1995. The dynamics of a Bose-Einstein condensate (BEC) in a trap is, in general, described by a nonlinear equation called the Gross-Pitaevskii equation (GPE), which is derived under a mean-field approximation. A condensate can sometimes be described by a few modes, for example, a BEC in a double-well potential and a tightly trapped spinor BEC. In these cases too, a mean-field theory is generally adequate. The approximation, however, breaks down under certain scenarios. Broadly speaking, this dissertation was motivated by these experimental scenarios where the usual description by the GPE or a mean-field theory *fails* to adequately describe the dynamics of a BEC.

We first studied the collision of two BECs near a Feshbach resonance and derived an extension of the GPE to describe the dynamics. We found that, in analogy to the optical phenomenon of slow light, a BEC traveling through another BEC with a collision energy near a Feshbach resonance slows down. We also studied dynamical instabilities in BECs where the mean-field approximation is no longer valid and quantum corrections need to be included. We analytically studied the dynamics

of integrable few-mode bosonic systems after they are quenched to a dynamically unstable point. We found excellent agreement between analytical and numerical studies within the truncated Wigner approximation (TWA). The TWA, however, deviates from the exact quantum dynamics after the quantum break time. This observation motivated the study of dynamics in the semiclassical approximation and we found that the TWA ignores terms arising from the interference of classical paths. We then analyzed a nonlinear oscillator and realized that the TWA is a good approximation to the exact quantum dynamics only for short times; on the other hand, the semiclassical theory agrees well with the exact dynamics for all times.

We also studied an interferometric experiment, which measured the current through and phase difference across a rotating barrier in a ring-shaped BEC. In this case, instead of going beyond the mean-field equations of motion, we found that the single-particle analysis, equivalent to ignoring the nonlinear term of the GPE, is adequate to qualitatively explain the spirals in the interference pattern and to define the relevant time scales.

We now discuss future research directions where our results could have immediate applicability. The dynamical instability in a spinor BEC has been proposed by M. Gabbrielli *et al.* [151] as a means of creating a nonlinear interferometer that can surpass the standard quantum limit. In this work, the interferometer was numerically studied for times when the TWA is valid. Hence, the formalism developed in Chapter 4 could provide analytical insights into the performance of this interferometer. Furthermore, the TWA analysis of the dynamics of the few-mode systems studied in Chapter 4 is only accurate up to the quantum break time. To analyt-

ically study the dynamics beyond this time, the semiclassical theory of Chapter 5 could be applied to these systems. It will, however, require a careful treatment as the reduced phase spaces are compact making the usual definition of the Wigner function inapplicable.

Appendix A: Dynamics of few-mode quantum systems

A.1 Pendulum

The simple pendulum is used throughout to illustrate our derivation of dynamics and long-time expectation values for few-mode integrable systems. In this appendix we derive results specific to the pendulum. Its Hamiltonian is given in Eq. 4.9 with canonical coordinates θ and p satisfying $\{\theta, p\} = 1$, where $\{\cdot, \cdot\}$ is the Poisson bracket.

First, librational trajectories $(\theta_B(t), p_B(t))$ in phase-space region B are [119]

$$\sin\left(\theta_B(t)/2\right) = k \, \text{sn}\left(t + t_0, k\right), \tag{A.1}$$

$$p_B(t) = 2k \, \text{cn}\left(t + t_0, k\right), \tag{A.2}$$

where the modulus $k = \sqrt{\mathcal{E}/2}$, $\mathcal{E}$ is the energy of the trajectory and time t_0 depends on the initial condition. Secondly, rotational trajectories $(\theta_R(t), p_R(t))$ in regions $R = A$ and C are

$$\sin\left(\theta_R(t)/2\right) = \pm\text{sn}\left((t + t_0)/k, k\right), \tag{A.3}$$

$$p_R(t) = \pm(2/k) \, \text{dn}\left((t + t_0)/k, k\right), \tag{A.4}$$

where $k = \sqrt{2/\mathcal{E}}$. The $+$ and $-$ signs correspond to regions A and C, respectively.

The functions $\mathrm{sn}(z,k)$, $\mathrm{cn}(z,k)$, and $\mathrm{dn}(z,k)$ are Jacobi elliptic functions [119]. Finally, on the separatrices $\mathcal{E} = 2$ with trajectories $(\theta_{S\pm}(t), p_{S\pm}(t))$ given by Eq. 4.10.

A.1.1 Distribution function $\mathcal{F}(\varpi)$

In this section we calculate the distribution function

$$\mathcal{F}(z) \;=\; \int_{\Omega} d\theta dp \, W_0(\theta,p) \, \delta(z - \varpi(\theta,p)), \tag{A.5}$$

as defined in Eq. 4.20, as well as its mean and width. Here, the integral is over the whole phase space Ω and the initial Gaussian distribution $W_0(\theta,p)$, given in Eq. 4.16, has a width d along both θ and p. The auxiliary frequency $\varpi(\theta,p) = \omega_1 = \pi/[kK(k)]$ in regions A and C and $\varpi(\theta,p) = 2\omega_1 = \pi/K(k)$ in region B, where $K(k)$ is the complete elliptic integral of the first kind with modulus $k \in [0,1]$ [119].

Near the saddle point the energy $\mathcal{E} \sim 2 + (p^2 - q^2)/2$, where $q = (\theta - \pi)$ mod 2π. The relationship between energy and modulus leads to $k^2 \sim 1 - |p^2 - q^2|/4$ in *all* regions. Finally, $\varpi \sim \pi/K(k) \sim 2\pi/\ln(64/|p^2 - q^2|)$ using the asymptotic expansion $K(k) \sim \ln(16/k'^2)/2$ around $k = 1$ with complementary modulus k' defined by $k'^2 = 1 - k^2$.

To compute $\mathcal{F}(\varpi)$ it is convenient to first introduce the invertible transformation $\mathcal{X}(\varpi) = 2k'^2/d^2 \sim 32e^{-2\pi/\varpi}/d^2$. The dependence of $\mathcal{X}(\varpi)$ on d will become clear later. We then write

$$\mathcal{F}(\varpi) \sim \frac{2\pi}{\varpi^2}\mathcal{X}(\varpi)P\left(\mathcal{X}(\varpi)\right), \tag{A.6}$$

as $d \to 0$ with the distribution

$$P(\mathcal{X}) = \int_\Omega d\theta dp \, W_0(\theta, p) \, \delta \left(\mathcal{X} - \frac{|p^2 - q^2|}{2d^2} \right), \tag{A.7}$$

and the factor in front of $P(\mathcal{X}(\varpi))$ in the right-hand side of Eq. A.6 is the Jacobian $d\mathcal{X}/d\varpi$.

The separatrices divide the neighborhood of the saddle point into four quadrants. We solve Eq. A.7 in each quadrant separately. For the quadrant in region A ($p > 0$ and $p > q$) we change the integration variables to $p = d\sqrt{2\mathcal{X}}\cosh u$ and $q = d\sqrt{2\mathcal{X}}\sinh u$ with $u \in (-\infty, \infty)$. Similar changes of variables can be used in the other three quadrants (noting that two quadrants lie in region B). The contribution to $P(\mathcal{X})$ from each quadrant turns out to be the same and we finally find

$$P(\mathcal{X}) = \frac{2}{\pi} K_0(\mathcal{X}), \tag{A.8}$$

where $K_0(x)$ is a modified Bessel function [119] and $P(\mathcal{X})$ has no explicit dependence on the width d. We then have

$$\mathcal{F}(\varpi) \sim \frac{128 e^{-2\pi/\varpi}}{d^2 \varpi^2} K_0 \left(\frac{32 e^{-2\pi/\varpi}}{d^2} \right), \tag{A.9}$$

as $d \to 0$ and for $\varpi \ll 1$.

Figure A.1 shows $\mathcal{F}(\varpi)$ as a function of ϖ for a single d. We find that $\mathcal{F}(\varpi)$ is sharply peaked. It approaches zero as $C \, e^{-2\pi/\varpi}/\varpi^3$ when $\varpi \to 0^+$ and C is a constant. For $\varpi \gtrsim 1$, where Eq. A.9 is invalid, either p or q is much greater than d and $W_0(\theta, p)$, hence $\mathcal{F}(\varpi)$, is exponentially small. Thus, it is reasonable to approximate $\mathcal{F}(\varpi)$ by a Gaussian as shown in Fig. A.1.
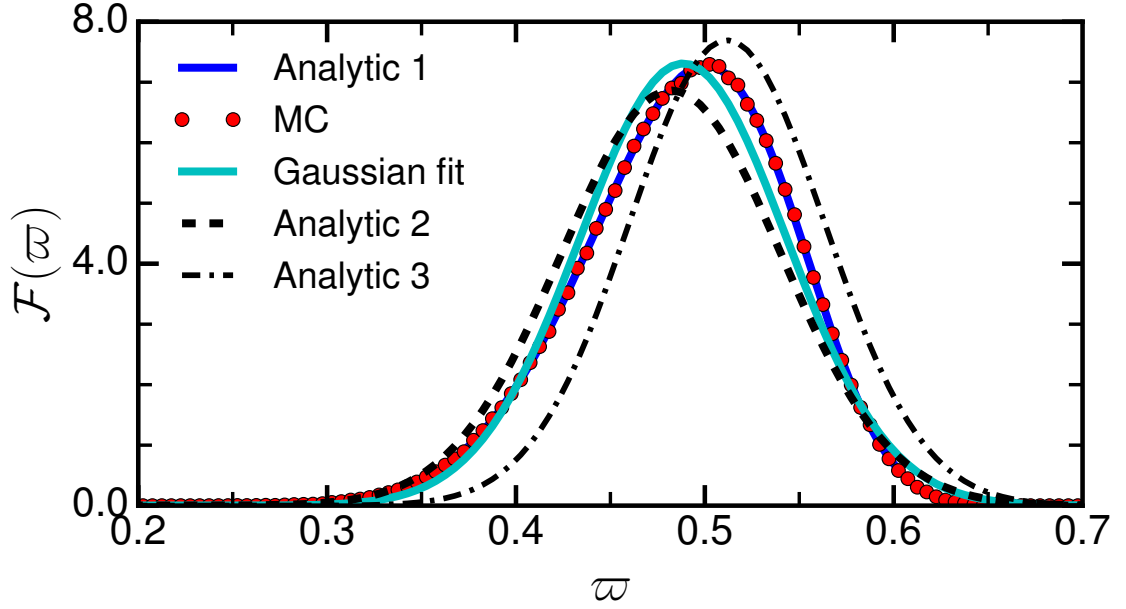
Figure A.1: Distribution function $\mathcal{F}(\varpi)$ as a function of the auxiliary frequency ϖ for the pendulum with an initial Wigner distribution (Eq. 4.16) with width $d = 1/20$. The blue solid line is the distribution in Eq. A.9. Indistinguishable from this curve is the $\mathcal{F}(\varpi)$ shown by red circles, which are obtained by numerical Monte Carlo sampling of the initial Wigner distribution. The cyan solid, black dashed, and black dashed-dotted lines are Gaussians whose mean and standard deviation are given by that of (1) the numerical distribution, (2) Eqs. A.11 and A.13, and (3) Eqs. A.14 and A.15, respectively.

We now calculate the mean and variance of ϖ using one of two methods. The mean $\mu \sim \int_0^\infty d\mathcal{X} \, P(\mathcal{X})\varpi(\mathcal{X})$ with $\varpi(\mathcal{X}) = 2\pi/\ln[32/(d^2\mathcal{X})]$. We then identify the small parameter $\lambda^{-1} = \ln(C/d^2)^{-1} \ll 1$, where the constant C will be determined later, and find

$$\mu \sim \frac{2\pi}{\lambda} + \frac{2\pi}{\lambda} \sum_{n=1}^{\infty} \frac{\mathrm{E}[\mathcal{Y}^n]}{\lambda^n}, \tag{A.10}$$

with the help of the geometric series. Here, $\mathcal{Y} = \ln(C\mathcal{X}/32)$ and $\mathrm{E}[\mathcal{Y}]$ is the expectation value of $\mathcal{Y}$ with respect to $P(\mathcal{X})$. For $C = 64e^\gamma$, where γ is the Euler-Mascheroni constant, the expectation value $E[\mathcal{Y}] = 0$. Hence,

$$\mu \sim \frac{2\pi}{\lambda} + O(1/\lambda^3). \tag{A.11}$$

Similarly, the variance

$$\sigma^2 \sim \left(\frac{2\pi}{\lambda}\right)^2 \left[\frac{\mathrm{E}[\mathcal{Y}^2] - \mathrm{E}[\mathcal{Y}]^2}{\lambda^2} + O(1/\lambda^3)\right] \tag{A.12}$$

and evaluation of the second moment of $\mathcal{Y}$ gives

$$\sigma \sim \frac{\pi^2}{\lambda^2} + O(1/\lambda^3). \tag{A.13}$$

Thus, we find $\mu = O(1/|\ln d|)$ and $\sigma = O(1/|\ln d|^2)$.

The second method estimates μ and σ from the location of and curvature at the maximum of $\mathcal{F}(\varpi)$ using the fact that the distribution is well approximated by a narrow Gaussian. We could not find a closed form for maximum of $\mathcal{F}(\varpi)$. Instead, we present results based on the extremum of $\varpi^2\mathcal{F}(\varpi)$. This only introduces small corrections as $\varpi^2\mathcal{F}(\varpi) \sim \mu^2\mathcal{F}(\varpi)$ over the width of the distribution near $\varpi = \mu$. After some algebra, we find

$$\mu \sim \frac{2\pi}{\ln\left(32/(\varkappa d^2)\right)}, \tag{A.14}$$

108

$$\sigma \sim \sqrt{-\left.\frac{g(\mathcal{X})}{d^2 g(\mathcal{X})/d\varpi^2}\right|_{\varpi=\mu}} = \frac{\mu^2}{2\pi\sqrt{1-\varkappa^2}} \tag{A.15}$$

where $g(\mathcal{X}) = \varpi^2 \mathcal{F}(\varpi) = 4\mathcal{X} K_0(\mathcal{X})$ and $\varkappa = 0.595\cdots$ is the solution of $dg(\mathcal{X})/d\mathcal{X} = 0$.

The estimates of μ and σ obtained by either method gives the same logarithmic scaling with d. The numerical prefactors inside the logarithm, however, are different. Figure A.1 shows Gaussian distributions with the estimated mean and width based on the two methods. Their difference from the true $\mathcal{F}(\varpi)$ vanishes as $d \to 0$.

A.1.2 Time dynamics of observables

In this subsection, we derive the time dynamics of observables for a pendulum. That is, we derive Eq. 4.28 from Eq. 4.27. The dependence of the quantity in the angular brackets $\langle\cdots\rangle_R$ in Eq. 4.27 on the action-angle coordinates is only through ω_1 and φ_1. (This is also true for the other two systems studied in the paper.) Denoting the quantity by $\mathcal{A}(\omega_1, \varphi_1)$ it is then convenient to write

$$\langle\mathcal{A}\rangle_R = \int d\omega_1 \int \frac{d\varphi_1}{2\pi}\mathcal{A}(\omega_1, \varphi_1)g_{0,R}(\omega_1, \varphi_1), \tag{A.16}$$

where

$$g_{0,R}(\omega_1, \varphi_1) = \int_{\mathcal{I}} d\mathbf{I} \int_0^{2\pi} \frac{d\boldsymbol{\varphi}'}{2\pi} f_{0,R}(\mathbf{I}, \boldsymbol{\varphi})\delta[\omega_1 - \omega_1(\mathbf{I})] \tag{A.17}$$

and $\boldsymbol{\varphi}' = (\varphi_2, \ldots, \varphi_n)$ are all the angles *except* φ_1. (The time dependence of $\mathcal{A}$ is suppressed for clarity.) For the pendulum with its 2D phase space Eq. A.17 simplifies to $g_{0,R}(\omega_1, \varphi_1) = dI_1/d\omega_1\, f_{0,R}(I_1, \varphi_1)$, where $dI_1/d\omega_1$ is the Jacobian of the transformation between I_1 and ω_1.

The function $g_{0,R}(\omega_1, \varphi_1)$ is concentrated around a few points in the (ω_1, φ_1) space from the observation that $W_0(\theta, p)$ is localized around the saddle point. The justification of this approximation is subtle and technical; it has been relegated to Appendix A.1.2.1. We find that

$$g_{0,R}(\omega_1, \varphi_1) \approx \begin{cases} 2\pi\, \overline{g}_{0,A}(\omega_1)\, \delta(\varphi_1), & R = A, C \\[2mm] \pi\, \overline{g}_{0,B}(\omega_1)\, [\delta(\varphi_1) + \delta(\varphi_1 - \pi)], & R = B \end{cases} \tag{A.18}$$

where $\overline{g}_{0,R}(\omega_1) = \int_0^{2\pi} d\varphi_1/(2\pi) g_{0,R}(\omega_1, \varphi_1)$ is a marginal distribution.

We can now simplify the average and sums on the right-hand side of Eq. 4.27 into a single average for observables that are even in θ and p. The bump functions $\mathcal{D}_{S+}(t)$ and $\mathcal{D}_{S-}(t)$ are then identical. Moreover, the angular dependence of $g_{0,B}(\omega_1, \varphi_1)$ implies that $\langle e^{im\varphi_1} \rangle_B = 0$ when m is odd so that odd Fourier components in region B do not contribute to $\langle \mathcal{O}(t) \rangle$. (For regions A and C, both even and odd Fourier components contribute.) Using these observations, the definition of the auxiliary frequency ϖ and the values of $\alpha_R(s)$, we combine the sum over regions and separatrices into a single sum and arrive at Eq. 4.28.

A.1.2.1   Derivation of Eq. A.18

We give a quantitative argument for Eq. A.18. In the evaluation of $\mathcal{F}(\varpi)$ in Appendix A.1.1 we observed that each quadrant in the neighborhood of the saddle point contributes equally. In region A, where $\varpi = \omega_1$, a comparison of Eq. 4.20 and the definition of $\overline{g}_{0,A}(\omega_1)$ shows that $\overline{g}_{0,A}(\omega_1) \propto \mathcal{F}(\omega_1)$. Thus, $g_{0,A}(\omega_1, \varphi_1)$ is localized around $\mu = \langle \varpi \rangle$ with a width $\sigma \ll \mu$ along the ω_1 coordinate.

Next, we define the standard deviation $\Delta_A(\omega_1)$ of φ_1 with respect to the conditional distribution $g_{0,A}(\omega_1, \varphi_1)/\bar{g}_{0,A}(\omega_1)$ at each value of ω_1. We now estimate $\Delta_A(\omega_1)$ from the momentum spread $\Delta p_A = O(d)$ in region A, where d is the width of $W_0(\theta, p)$. Using Eq. A.4 we find

$$p_A = \frac{2}{k} \, \mathrm{dn} \left(\frac{\varphi_1}{\omega_1 k} + K(k), k \right), \tag{A.19}$$

where $t_0 = kK(k)$, because p_A is minimal when $\varphi_1 = 0$ [see Fig. 4.2(a)]. Now, we expect the relevant φ_1 to be small and use the Taylor expansion $\mathrm{dn}(x + K(k), k) = k' + k'k^2 x^2/2 + \cdots$ for small x to find

$$p_A - p_A^{\mathrm{min}} \sim k' \left(\frac{\varphi_1}{\omega_1} \right)^2. \tag{A.20}$$

where $k' = \sqrt{1 - k^2} \sim 4e^{-\pi/\omega_1}$ and $p_A^{\mathrm{min}} = 2k'/k$. Thus, the width $\Delta_A(\omega_1) \propto \omega_1 \sqrt{\Delta p_A/k'} \propto \omega_1 e^{\pi/(2\omega_1)} \sqrt{d}$. At first glance, this relation contradicts the assumption that $\Delta_A(\omega_1)$ is small because $\Delta_A(\omega_1)$ diverges as $\omega_1 \to 0^+$. From Appendix A.1.1, however, we know that $\mathcal{F}(\omega_1)$ and, thus, $\bar{g}_{0,A}(\omega_1)$ go to zero rapidly as $\omega_1 \to 0^+$. In fact, at the mean value $\omega_1 = \mu$, given in Eq. A.14, we find $\Delta_A(\mu) = O(1/|\ln d|) \ll 1$. Furthermore, $\Delta_A(\omega_1)$ remains small where $g_{0,A}(\omega_1, \varphi_1)$ is significant as $\sigma \ll \mu$. Hence, $g_{0,A}(\omega_1, \varphi_1)$ is localized in both ω_1 and φ_1. [The distribution $f_{0,A}(I_1, \varphi_1)$ is not localized in φ_1 as it does not approach zero as $\omega_1(I_1) \to 0^+$.]

The nonzero, albeit small, width of $g_{0,R}(I_1, \varphi_1)$ in the ω_1 coordinate leads to mixing in φ_1. On the other hand, the distribution over ω_1 is invariant in time. We can then replace the narrow distribution $g_{0,A}(\omega_1, \varphi_1)$ along φ_1 by a delta function. That is, $g_{0,A}(\omega_1, \varphi_1) \approx 2\pi \bar{g}_{0,A}(\omega_1)\delta(\varphi_1)$. A similar analysis in regions B and C leads to the other two equations in Eq. A.18.

A.2 A condensate in a double-well potential

In this appendix, we derive results pertaining to a two-mode Bose-Einstein condensate in a double-well potential. Its "single-particle" Hamiltonian $h_{\mathrm{dw}}(\phi, z)$ is defined in Eq. 4.32 and $\{\phi, z\} = 1$. For $\Lambda > 1$ the Hamiltonian has a single saddle point and two separatrices S divide the phase space into three distinct regions $R = A$, B, and C. The solutions to the equations of motion are [122]

$$z_R(t) = \begin{cases} \mathcal{C} \operatorname{cn} \left(\mathcal{C}\Lambda(t - t_0)/(2\kappa), \kappa \right), & R = B \\[2mm] \pm\mathcal{C} \operatorname{dn} \left(\mathcal{C}\Lambda(t - t_0)/2, 1/\kappa \right), & R = A, C \end{cases} \tag{A.21}$$

where

$$\mathcal{C}^2 = \frac{2}{\Lambda^2} \left(\mathcal{E}\Lambda - 1 + \sqrt{\Lambda^2 - 2\mathcal{E}\Lambda + 1} \right), \tag{A.22}$$

$$\kappa^2 = \frac{1}{2} + \frac{\mathcal{E}\Lambda - 1}{2\sqrt{\Lambda^2 - 2\mathcal{E}\Lambda + 1}}. \tag{A.23}$$

The "single-particle" energy of the trajectory is $\mathcal{E}$ and t_0 depends on the initial condition. The corresponding $\phi_R(t)$ can be obtained by solving $h(\phi_R(t), z_R(t)) = \mathcal{E}$. (Note that Ref. [122] misses a factor of $1/2$ in the first argument of both $\operatorname{cn}(z, k)$ and $\operatorname{dn}(z, k)$.) Finally, on the separatrices $\mathcal{E} = 1$, $\kappa = 1$ and $\mathcal{C} = 2\sqrt{\Lambda - 1}/\Lambda$ with solutions $z_{S\pm}(t)$ given by Eq. 4.33.

A.2.1 Distribution function $\mathcal{F}(\varpi)$

We now compute the distribution function $\mathcal{F}(\varpi)$ for a Bose condensate in a double-well potential. The initial Wigner distribution Eq. 4.34 is localized around the saddle point $(\psi_1, \psi_2) = (\sqrt{N/2}, -\sqrt{N/2})$. It is convenient to introduce real

coordinates p_i and q_i defined by $p_1 + iq_1 = \psi_1 - \sqrt{N/2}$ and $p_2 + iq_2 = \psi_2 + \sqrt{N/2}$.

In these coordinates, the Wigner distribution becomes

$$W_0(p_i, q_i) = \frac{4}{\pi^2} e^{-2(p_1^2 + q_1^2 + p_2^2 + q_2^2)}, \tag{A.24}$$

where $i \in \{1, 2\}$ and the probability measure is $dp_1 dq_1 dp_2 dq_2$. Near the saddle point

$$z = \sqrt{\frac{2}{N}}(p_1 + p_2) + O(N^{-1}), \tag{A.25}$$

$$\phi = -\pi + \frac{q_1 + q_2}{\sqrt{N}} + O(N^{-1}) \tag{A.26}$$

and their substitution into $h_{\mathrm{dw}}(\phi, z)$ gives the energy

$$\mathcal{E} = 1 + \frac{1}{N}\left[(\Lambda - 1)(p_1 + p_2)^2 - (q_1 + q_2)^2\right] + O(N^{-3/2}) \tag{A.27}$$

close to one.

Next, we express the auxiliary frequency $\varpi = \omega_1$ in regions A, C and $2\omega_1$ in region B in terms of coordinates p_i and q_i. From Eq. A.21 and the periodicity of elliptic functions, it follows that near the separatrix $\varpi \sim \pi\sqrt{\Lambda - 1}/K(k) \sim 2\pi\sqrt{\Lambda - 1}/\ln(16/k'^2)$ where $k = \kappa$ in region B and $1/\kappa$ in regions A, C. The modulus k and its complement k' depend on $\mathcal{E}$ and thus on the p_i and q_i. With the help of Eqs. A.23 and A.27, we find

$$\mathcal{X} \equiv 2\left(\frac{\Lambda - 1}{\Lambda}\right)^2 N k'^2 \sim |(\Lambda - 1)(p_1 + p_2)^2 - (q_1 + q_2)^2|. \tag{A.28}$$

This choice of $\mathcal{X}$, in particular its N dependence, will simplify later derivations. We realize that $\varpi \sim 2\pi\sqrt{\Lambda - 1}/\ln[32N(\Lambda - 1)^2/(\mathcal{X}\Lambda^2)]$ and $\mathcal{X}(\varpi) = 32N(1 - \Lambda^{-1})^2 e^{-2\pi\sqrt{\Lambda - 1}/\varpi}$. Thus, we have established a relation between ϖ and p_i, q_i via the variable $\mathcal{X}$.
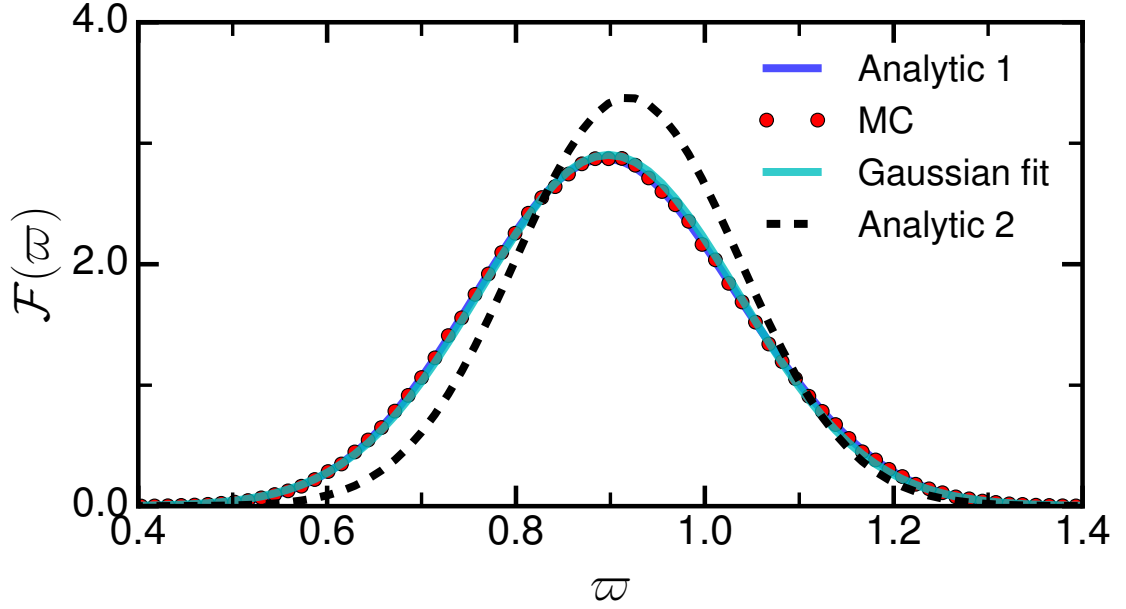
Figure A.2: Distribution function $\mathcal{F}(\varpi)$ as a function of auxiliary frequency ϖ for a Bose-Einstein condensate in a double-well potential with 1000 atoms and $\Lambda = 2$. The solid blue curve is the distribution in Eq. A.29. Indistinguishable from this curve is the $\mathcal{F}(\varpi)$ shown by red circles, which is obtained by Monte Carlo sampling of the initial Wigner distribution. The cyan solid line is a Gaussian fit to these data. The dashed line is a Gaussian distribution whose mean and standard deviation are given by Eqs. A.34 and A.35, respectively.

The distribution $\mathcal{F}(\varpi)$ is then

$$\mathcal{F}(\varpi) = \frac{2\pi\sqrt{\Lambda - 1}}{\varpi^2}\mathcal{X}(\varpi)\mathcal{P}(\mathcal{X}(\varpi)), \qquad (A.29)$$

where

$$\mathcal{P}(\mathcal{X}) = \int dp_1 dq_1 dp_2 dq_2\, W_0(p_i, q_i)\, \delta(\mathcal{X} - \mathcal{Z}(p_i, q_i)), \qquad (A.30)$$

with $\mathcal{Z}(p_i, q_i)$ equal to the right-hand side of Eq. A.28 and the factor multiplying $\mathcal{P}(\mathcal{X})$ in Eq. A.29 is the Jacobian $d\mathcal{X}/d\varpi$.

We simplify the integrals in Eq. A.30 by changing to "center of mass" and "relative" coordinates $P = (p_1 + p_2)/2$, $p = p_1 - p_2$, $Q = (q_1 + q_2)/2$ and $q = q_1 - q_2$. We find

$$\mathcal{P}(\mathcal{X}) = \frac{4}{\pi}\int_{-\infty}^{\infty} dP dQ\, e^{-4P^2 - 4Q^2}\delta\left(\mathcal{X} - 4|(\Lambda - 1)P^2 - Q^2|\right), \qquad (A.31)$$

which yields

$$\mathcal{P}(\mathcal{X}) = \frac{2}{\pi\sqrt{\Lambda - 1}}\cosh\left(\frac{\Lambda - 2}{2(\Lambda - 1)}\mathcal{X}\right)K_0\left(\frac{\Lambda\mathcal{X}}{2(\Lambda - 1)}\right). \qquad (A.32)$$

Figure A.2 shows $\mathcal{F}(\varpi)$ for $N = 1000$ and $\Lambda = 2$. It is evident from the figure that $\mathcal{F}(\varpi)$ is well approximated by a Gaussian distribution. The mean μ and width σ of $\mathcal{F}(\varpi)$ can be computed from Eqs. A.10 and A.12, respectively, with $\lambda = \ln[32N(1 - \Lambda^{-1})^2/\Lambda^2]/\sqrt{\Lambda - 1}$. Although we have not been able to evaluate analytically the moments $E[\mathcal{Y}^n]$ with $\mathcal{Y} = \ln(\mathcal{X})$, the equations imply that μ is $O(1/\ln N)$ and σ is $O[1/(\ln N)^2]$.

We can compute μ using the second method described in Appendix A.1.1. The location of the maximum of Eq. A.29 is a solution to a transcendental equation

that does not have a closed form for arbitrary values of Λ. For small positive $\Lambda - 1$, however, we find a closed-form solution by replacing cosh in Eq. A.32 by a constant, chosen such that the approximate $P(\mathcal{X})$ remains unit normalized. Thus,

$$P(\mathcal{X}) \approx \frac{\Lambda}{\pi(\Lambda - 1)} K_0 \left(\frac{\Lambda \mathcal{X}}{2(\Lambda - 1)} \right). \tag{A.33}$$

and we find

$$\mu \approx \frac{2\pi\sqrt{\Lambda - 1}}{\ln\left[16N(\Lambda - 1)/(\Lambda \varkappa)\right]}, \tag{A.34}$$

$$\sigma \approx \frac{\mu^2}{2\pi\sqrt{(\Lambda - 1)(1 - \varkappa^2)}}, \tag{A.35}$$

where $\varkappa = 0.595\cdots$ and $\Lambda - 1 \ll 1$.

A.2.2 Time dynamics of observables

The structure of the phase space of a condensate in double-well potential is similar to that of the pendulum. Therefore, we can directly apply the analysis of time dynamics for a pendulum given in Appendix A.1.2. In particular, the distribution functions $g_{0,R}(\omega_1, \varphi_1)$, as defined in Eq. A.17, are localized and are given by Eq. A.18. Furthermore, observable $\langle s_x(t) \rangle$ obeys Eq. 4.29.

A.3 Spinor gas in single-mode approximation

In this appendix, we obtain results for an antiferromagnetic $(c > 0)$ spinor condensate under SMA. Its "single-particle" Hamiltonian $h_{\text{spin}}(\phi, \rho_0)$ is given in Eq. 4.37 and $\{\phi, \rho_0\} = 1$. For $-2c < q < 0$ the Hamiltonian has a single saddle point and a separatrix S dividing the phase space into regions $R = A$ and B. In

116

both regions [89]

$$\rho_{0,R}(t) = y_2 - (y_2 - y_1)\operatorname{cn}^2(\Omega(t - t_0), k), \tag{A.36}$$

where $\operatorname{cn}(z, k)$ is a Jacobi elliptic function [119] and $y_1 \leq y_2 \leq y_3$ are the three real roots of the cubic equation in ρ_0

$$[\mathcal{E} - q(1 - \rho_0)][(2c\rho_0 + q)(1 - \rho_0) - \mathcal{E}] - (c\rho_0 m)^2 = 0. \tag{A.37}$$

Here, $\mathcal{E}$ is the "single-particle" energy of the trajectory and m is the unit magnetization. In terms of these roots, $\Omega = \sqrt{2|q|c(y_3 - y_1)}$ and the modulus $k = \sqrt{(y_2 - y_1)/(y_3 - y_1)}$. The solution is periodic in time with period $T = 2K(k)/\Omega$ and frequency $\omega_1 = 2\pi/T = 2\pi\Omega/[2K(k)]$. The corresponding $\phi_R(t)$ is obtained by solving $h_{\mathrm{spin}}(\phi_R(t), \rho_{0,R}(t)) = \mathcal{E}$.

On the separatrix S the energy $\mathcal{E} = 0$ and the roots of Eq. A.37 are $y_{1,S} = |q|/(2c)$ and $y_{2,S} = y_{3,S} = 1$. Using the fact $\operatorname{cn}(x, k) \sim \operatorname{sech}(x)$ as $k \to 1$ and setting $t_0 = 0$, we find the separatrix solution

$$\rho_{0,S}(t) = 1 - (1 - y_{1,S})\operatorname{sech}^2(\Omega_S t), \tag{A.38}$$

where $\Omega_S = \sqrt{2|q|c(1 - y_{1,S})}$.

A.3.1   Distribution function $\mathcal{F}(\varpi)$

We now study the distribution $\mathcal{F}(\varpi)$ for the spinor condensate by relating the auxiliary frequency ϖ to the conserved quantities $\mathcal{E}$, m and N. As the initial Wigner distribution $W_0(\psi_j, \psi_j^*)$ is localized near the saddle point with $\rho_0 = 1$, i.e., $(\psi_{+1}, \psi_0, \psi_{-1}) = (0, \sqrt{N}, 0)$, we again define real coordinates p_j and q_j via $\psi_j =$

$\delta_{j0}\sqrt{N} + p_j + iq_j$. Then the relevant trajectories have energy $\mathcal{E} = 0 + \widetilde{\mathcal{E}}/N + O(N^{-3/2})$ and unit-magnetization $m = 0 + \widetilde{m}/N + O(N^{-3/2})$, both close to zero. The quantities $\widetilde{\mathcal{E}}$ and $\widetilde{m}$ are $O(1)$ and depend on p_j and q_j. We solve for the roots y_i perturbatively with small parameter $1/N$ and find that the modulus k is close to one. Then the auxiliary frequency $\varpi = \omega_1 \sim 2\pi\Omega/\ln(16/k'^2)$ in regions A and B. We define

$$\mathcal{X} \equiv Nk'^2 \sim \frac{c}{|q|} \frac{\sqrt{\widetilde{\mathcal{E}}^2 + \alpha\widetilde{m}^2}}{(1 - y_{1,S})^2}, \tag{A.39}$$

which is independent of N, and $\alpha = 2|q|(1-y_{1,S})/c$. Conversely, $\varpi = 2\pi\Omega/[\ln(16N/\mathcal{X})]$. Unlike for the previous two systems, we have not been able to find an analytical expression for the distribution of $\mathcal{X}$. Nevertheless, we can apply Eq. A.10 with small parameter $\lambda^{-1} = \Omega/\ln(16N)$ and find

$$\mu \sim \frac{2\pi\Omega}{\ln(16N)}. \tag{A.40}$$

Moreover, Eq. A.12 implies that $\sigma = O[1/(\ln N)^2]$; hence, $\sigma \ll \mu$ as $N \to \infty$.

We have numerically evaluated $\mathcal{F}(\varpi)$ and found that it is a Gaussian to a good approximation for $-2c < q < 0$. Figure A.3 shows $\mathcal{F}(\varpi)$ for $q/c = -1$ and $N = 1000$ and a Gaussian fit to this distribution. For Fig. 4.7 we use the mean and width of the numerically obtained $\mathcal{F}(\varpi)$.

A.3.2   Time dynamics of observables for $-2c < q < 0$

We now obtain an approximation for $g_{0,R}(\omega_1, \varphi_1)$, as defined in Eq. A.17, for the spinor system, where $R \in \{A, B\}$. The initial Wigner distribution $W_0(\psi_i, \psi_i^*)$ is localized around the saddle point and, thus, we expect $g_{0,R}(\omega_1, \varphi_1)$ to be localized
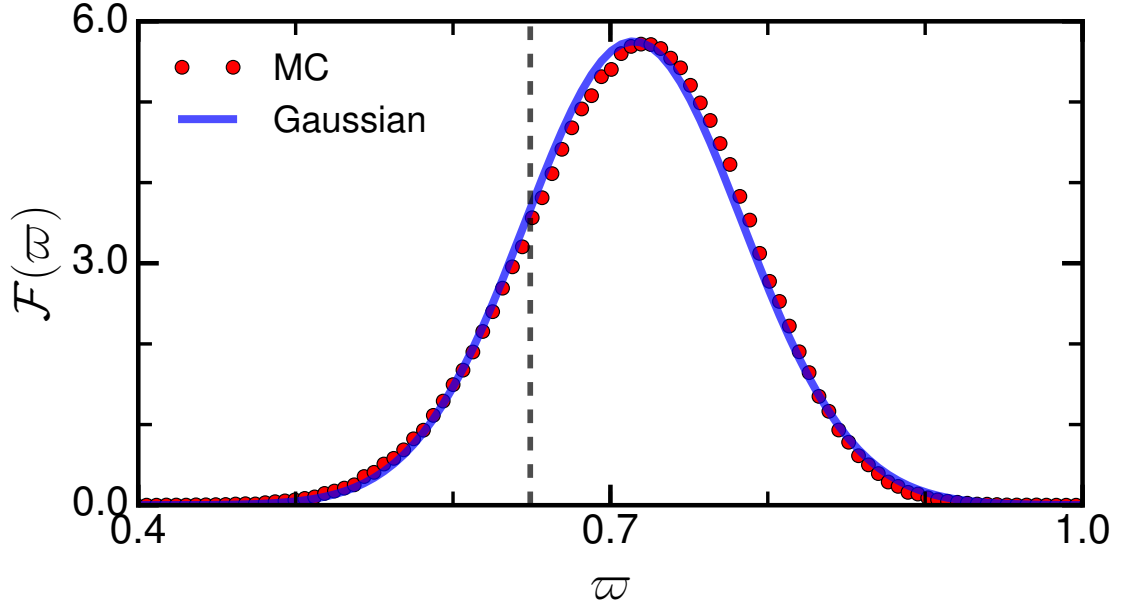
Figure A.3: Distribution function $\mathcal{F}(\varpi)$ as a function of the auxiliary frequency ϖ for a spinor condensate with 1000 atoms and $q/c = -1$. Red dots represent $\mathcal{F}(\varpi)$ obtained by Monte Carlo sampling of the initial Wigner distribution given by Eq. 4.39 and the blue solid line is a Gaussian fit to these data. The mean according to Eq. A.40 is the dashed vertical line.

around the $\varphi_1 = 0$ (see Fig 4.6). This can be formally justified by writing $\rho_0(t)$ along a trajectory near the separatrix in terms of the angle φ_1. Then, similar to Appendix A.1.2.1 we can show that the spread in φ_1 is much smaller than one where $g_{0,R}(\omega_1, \varphi_1)$ is significant. Thus,

$$g_{0,R}(\omega_1, \varphi_1) \approx 2\pi \overline{g}_{0,R}(\omega_1) \delta(\varphi_1), \tag{A.41}$$

where $\overline{g}_{0,R}(\omega_1) = \int_0^{2\pi} d\varphi_1/(2\pi) g_{0,R}(\omega_1, \varphi_1)$ is a marginal distribution.

A.3.3 Time dynamics for $q = 0$

The dynamics of a spinor condensate quenched to $q = 0$ is qualitatively different from that for $q < 0$. Instead of a single saddle point, the Hamiltonian has a degenerate line of saddle points along $\phi = \pi$. Along a trajectory close to this line $\rho_0(t)$ is a sinusoid given by

$$\rho_0(t) \sim \cos^2[\sqrt{2c\mathcal{E}}(t + t_0)], \tag{A.42}$$

where energy $\mathcal{E} \equiv h_{\text{spin}}(\phi, \rho_0) > 0$ and t_0 is determined by the initial condition. This trajectory does not spend a significant fraction of its time period near $\rho_0 = 1$ that violates one of the assumptions under which Eq. 4.15 was derived.

We can, nevertheless, find an analytical expression for $\langle \rho_0(t) \rangle$ by evaluating the expectation value directly from Eq. 4.1. The initial Wigner distribution, Eq. 4.39, is localized around $\rho_0 = 1$, and thus time $t_0 \approx 0$ for the relevant trajectories. Hence, we only require the distribution function

$$P(\mathcal{E}) = \int d\psi_i^* d\psi_i \, W_0(\psi_i, \psi_i^*) \, \delta(\mathcal{E} - h_{\text{spin}}(\phi, \rho_0)). \tag{A.43}$$

Now, $\rho_0 = 1$ corresponds to the mean-field state $(\psi_{+1}, \psi_0, \psi_{-1}) = (0, \sqrt{N}, 0)$ and near $\rho_0 = 1$ the Hamiltonian $h_{\mathrm{spin}}(\phi, \rho_0) = c[(p_{+1} + p_{-1})^2 + (q_{+1} - q_{-1})^2]/N + O(N^{-3/2})$, with quadratures p_j and q_j defined by $\psi_{+1} = p_{+1} + iq_{+1}$ and $\psi_{-1} = p_{-1} + iq_{-1}$. Substituting the Wigner distribution into Eq. A.43 and computing the integrals, we find $P(\mathcal{E}) \sim Nc^{-1}e^{-N\mathcal{E}/c}$. Finally, averaging Eq. A.42 over this distribution yields

$$\langle \rho_0(t) \rangle \sim 1 - \alpha t\, F(\alpha t), \tag{A.44}$$

where $\alpha = c\sqrt{2/N}$ and $F(x)$ is the Dawson integral [119].

Appendix B: Beyond the truncated Wigner approximation

B.1   Derivatives of action

Here, we evaluate the derivatives of the action $S^c(\mathbf{x}_f, \mathbf{x}_i, t)$ with respect to the initial and final positions. For simplicity, we assume that the configuration space is one-dimensional; generalization to higher dimensions is straightforward. Consider a classical path $[x^c(\tau), p^c(\tau)]$, which starts from the phase-space point (x_i^c, p_i^c) and ends at (x_f^c, p_f^c). To calculate $\partial S^c(x_f, x_i, t)/\partial x_i$, consider another classical path whose position in time, $x^c(\tau) + \delta x^c(\tau)$, is infinitesimally close to $x^c(\tau)$ such that $\delta x^c(0) = \Delta x_i$ is a infinitesimal change in the initial position and $\delta x^c(t) = 0$, i.e., the final position is fixed. Then the change in the action is

$$\Delta S^c = \int_0^t d\tau \left(\frac{\partial L}{\partial x} \delta x^c(\tau) + \frac{\partial L}{\partial \dot{x}} \delta \dot{x}^c(\tau) \right)$$
$$= \int_0^t dt \left(\frac{\partial L}{\partial x} - \frac{d}{dt} \frac{\partial L}{\partial \dot{x}} \right) \delta x^c(\tau) + \frac{\partial L}{\partial \dot{x}} \delta x^c(\tau) \Big|_0^t,$$

where $\dot{x} = dx/d\tau$ and we have suppressed the arguments of L. Now, the first term vanishes because $x^c(\tau)$ satisfies the Euler-Lagrange equations of motion. Using the fact that $p = \partial L(x, \dot{x})/\partial \dot{x}$, we have $\Delta S^c = -p_i^c \Delta x_i$. Therefore,

$$\frac{\partial S^c(x_f, x_i, t)}{\partial x_i} = -p_i^c. \tag{B.1}$$

Similarly, we can prove that

$$\frac{\partial S^c(x_f, x_i, t)}{\partial x_f} = p_f^c. \tag{B.2}$$

B.2 Derivation of Eq. 5.14

Here, we derive Eq. 5.14, which was used for proving that the semiclassical approximation reduces to the TWA when the interference terms are ignored. First, note that the final position $\mathbf{x}_f$ at a given time is uniquely determined by the initial position and momentum $\mathbf{x}_i$ and $\mathbf{p}_i$; therefore, at fixed values of $\mathbf{x}_i$ and t, $\mathbf{x}_f(\mathbf{x}_i, \mathbf{p}_i, t)$ is a function of $\mathbf{p}_i$ (from $\mathbb{R}^d$ to $\mathbb{R}^d$, where $2d$ is the phase space dimension). Next, we write

$$\delta(\mathbf{x}_f(\mathbf{x}_i, \mathbf{p}_i, t) - \mathbf{x}_f^c) = \sum_c \frac{\delta\left(\mathbf{p}_i - \mathbf{p}_i^c\right)}{\left|\det\left[\left(\frac{\partial \mathbf{x}_f}{\partial \mathbf{p}_i}\right)\Big|_{\mathbf{p}_i=\mathbf{p}_i^c}\right]\right|}, \tag{B.3}$$

where the sum is over all roots $\mathbf{p}_i^c$ of the equation $\mathbf{x}_f(\mathbf{x}_i, \mathbf{p}_i, t) = \mathbf{x}_f^c$ [1]. The quantity in the denominator on the right-hand side is the absolute value of the Jacobian determinant of the transformation from $\mathbf{p}_i$ to $\mathbf{x}_f$. Next, we apply the inverse function theorem, which states that matrix inverse of a Jacobian is the Jacobian of the inverse mapping, to find

$$\frac{1}{\det\left[\left(\frac{\partial \mathbf{x}_f}{\partial \mathbf{p}_i}\right)\Big|_{\mathbf{p}_i=\mathbf{p}_i^c}\right]} = \det\left[\left(\frac{\partial \mathbf{p}_i^c}{\partial \mathbf{x}_f}\right)\Big|_{\mathbf{x}_f=\mathbf{x}_f^c}\right], \tag{B.4}$$

---

[1] The equation is the multidimensional version of the formula $\delta(z(y)-z_0) = \sum_i \delta(y-y_i)/|z'(y_i)|$, where the sum is over the roots y_i of the equation $z(y) = z_0$ and $z'(y)$ is the derivative of z with respect to y.

where the initial momentum is, in general, a multivalued function of $\mathbf{x}_f$ (at fixed values of $\mathbf{x}_i$ and t) with the branches indexed by c. Finally, we use the multivariable version of Eq. B.1 to find

$$\frac{\partial \mathbf{p}_i^c}{\partial \mathbf{x}_f} = -\frac{\partial^2 S^c(\mathbf{x}_f, \mathbf{x}_i, t)}{\partial \mathbf{x}_f \partial \mathbf{x}_i} \tag{B.5}$$

Substituting this relation in Eq. B.3, we arrive at Eq. 5.14.

B.3   Action of the nonlinear oscillator

We now compute the action $S^c(x_f, x_i, t)$ of the nonlinear oscillator described in Sec. 5.4. The action depends on the index c, which we have not yet quantified. A natural guess would be the winding number w of the path around the phase-space origin. For a given (x_f, x_i, w, t), however, there can be multiple paths. Two such paths are shown in Fig. B.1 for $w = 0$. In contrast, a given value of $(\varphi_f, \varphi_i, w, t)$, where φ_i and φ_f are the initial and the final angles, respectively, uniquely determines a classical path. The reason is that the frequency, which satisfies $\omega t = (\varphi_f - \varphi_i) \bmod 2\pi + 2\pi w$, is then known; thereby, uniquely determining the radius $\rho = \sqrt{2\omega/U}$, which is a constant for a classical path. Therefore, the winding number indexes the classical paths if the boundary conditions are in terms of the angles. Thus, we define the action in terms of angle coordinates $\mathscr{S}^w(\varphi_f, \varphi_i, t) = S^c[x_f(\varphi_f, \varphi_i, w, t), x_i(\varphi_f, \varphi_i, w, t), t]$, where w is the winding number of the path c and x_f, x_i are the initial and final x coordinates, respectively, which are uniquely determined by $(\varphi_f, \varphi_i, w, t)$.

Let's evaluate

$$\mathscr{S}^w(\varphi_f, \varphi_i, t) = \int_0^t d\tau \, L\left[x^c(\tau), \frac{dx^c(\tau)}{d\tau}\right]$$

$$= \int_0^t dt \left[p^c(t)\frac{dx^c(\tau)}{d\tau} - \mathcal{H}_{\mathrm{NO}}\right], \tag{B.6}$$

where the classical Hamiltonian $\mathcal{H}_{\mathrm{NO}}$ is given by Eq. 5.19. Substituting $x(\tau) = \rho \sin\varphi(\tau)$ and $p(\tau) = \rho \cos\varphi(\tau)$, we find

$$\mathscr{S}^w(\varphi_f, \varphi_i, t) = \int_0^t d\tau \left(\omega\rho^2 \cos^2\varphi(\tau) - \frac{U\rho^4}{8}\right),$$

where we used the fact that $d\rho/d\tau = 0$ and $d\varphi/d\tau = \omega$; and we have suppressed the dependence of ρ and ω on φ_i, φ_f, w and t. The path in the polar coordinates $(\rho, \varphi(\tau))$ satisfies the boundary conditions $\varphi(0) = \varphi_i$ and $\varphi(t) = \varphi_f$. Then, after converting the integral over time to one over angle, we find

$$\mathscr{S}^w(\varphi_f, \varphi_i, t) = \frac{[(\varphi_f - \varphi_i) \bmod 2\pi + 2\pi w]}{2Ut} \tag{B.7}$$

$$\times \left[(\varphi_f - \varphi_i) \bmod 2\pi + 2\pi w + \sin(2\varphi_f) - \sin(2\varphi_i)\right].$$

B.4 Calculation of $\langle \hat{a}(t) \rangle$

Here, we calculate the expectation value of $a(t)$ within the semiclassical approximation. For clarity, we follow the outline presented in Sec. 5.4.2.

1. Consider the evolution of the expectation value of an observable $\mathcal{O}(x, p)$. (We will specialize to the case $\mathcal{O}(x, p) = a(x, p)$ later.) Its evolution under semiclassical approximation is

$$\langle \mathcal{O}(t) \rangle_{\mathrm{SC}} = \int dx_i dx_f dp_i dp_f \, \mathcal{O}(x_f, p_f) G_{\mathrm{SC}}(r_f, r_i, t) W_0(x_i, p_i). \tag{B.8}$$
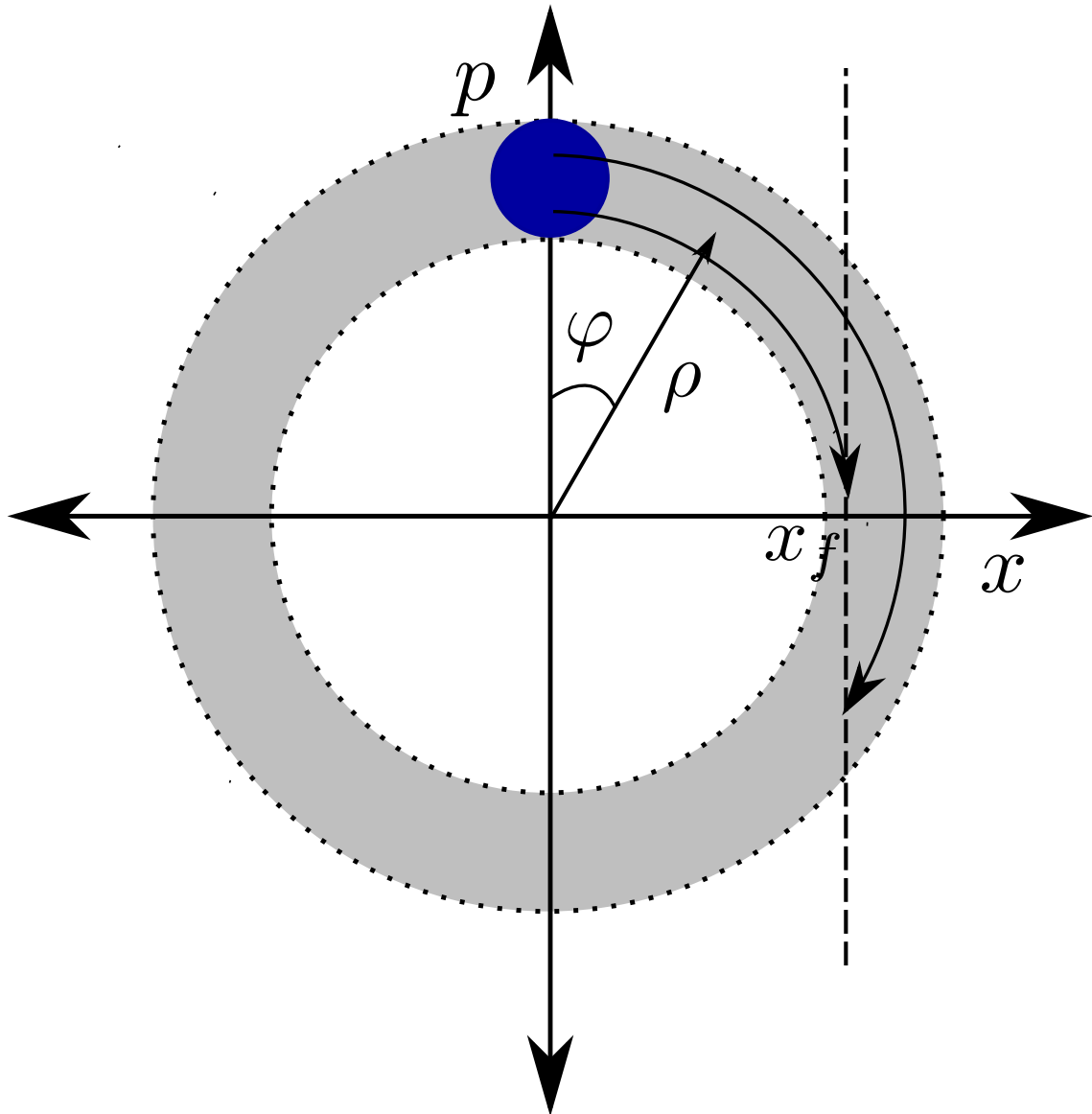
Figure B.1: Phase space of a nonlinear oscillator, which is spanned by position x and momentum p. The initial Wigner distribution of Eq. 5.21 is peaked around the area shown by the blue solid circle. The dotted circles demarcates the gray annulus in which the relevant trajectories starting from the blue solid circle are restricted. Shown are two classical paths that start from $x = 0$ and end at $x = x_f$. Both paths have zero winding number around the origin. The polar coordinates (ρ, φ), with the polar angle φ measured from the p-axis in a clockwise direction, are also shown.

Substituting $G_{\mathrm{SC}}(r_f, r_i, t)$ from Eq. 5.10 and integrating over the momenta p_i and p_f, we find

$$\langle \mathcal{O}(t) \rangle_{\mathrm{SC}} = \int dx_i dx_f \sum_{c,c'} \mathcal{O}\left(x_f, \frac{p_f^c + p_f^{c'}}{2}\right) W_0\left(x_i, \frac{p_i^c + p_i^{c'}}{2}\right) \qquad (\text{B.9})$$

$$\times \sqrt{\mathcal{D}^c \mathcal{D}^{c'}} \, e^{iS^c - iS^{c'} - i(\mu^c - \mu^{c'})\pi/2},$$

where we have suppressed the dependence of p_i^c, $\mathcal{D}^c$, S^c, etc., on x_i, x_f and t.

2. Next, we note that the action has a simpler form in terms of the angles (see Eq. B.7). Hence, we proceed to change the integration variables in Eq. B.10 to the angle coordinates. To this end, we first note that the sum in Eq. B.9 is over two sets of classical paths. In contrast, the integral is over one set of initial and final positions. So, for later manipulations, we introduce another set of initial and final positions to find

$$\langle \mathcal{O}(t) \rangle_{\mathrm{SC}} = \int dx_i dx_f dx'_i dx'_f \, \delta(x_i - x'_i)\delta(x_f - x'_f) \qquad (\text{B.10})$$

$$\times \sum_{c,c'} \mathcal{O}\left[\frac{x_f + x'_f}{2}, \frac{p_f^c(x_f, x_i, t) + p_f^{c'}(x'_f, x'_i, t)}{2}\right] W_0\left[\frac{x_i + x'_i}{2}, \frac{p_i^c(x_f, x_i, t) + p_i^{c'}(x'_f, x'_i, t)}{2}\right]$$

$$\times \sqrt{\mathcal{D}^c(x_f, x_i, t)\mathcal{D}^{c'}(x'_f, x'_i, t)} \, e^{iS^c(x_f, x_i, t) - iS^{c'}(x'_f, x'_i, t) - i[\mu^c(x_f, x_i, t) - \mu^{c'}(x'_f, x'_i, t)]\pi/2},$$

where we have shown explicit dependence of the quantities to avoid any confusion. The next step is to change the integration measure in terms of the angles. This step is carried out in Appendix B.4.1 and we find

$$\int dx_i dx_f \sum_c (\dots) = \sum_{w=w_{\min}}^{w_{\max}} \int_{-\pi}^{\pi} d\varphi_f \int_{-\pi}^{\pi} d\varphi_i \left| \det\left[\frac{\partial(x_i^w, x_f^w)}{\partial(\varphi_i, \varphi_f)}\right] \right| (\dots), \qquad (\text{B.11})$$

where $x_i^w(\varphi_f, \varphi_i) = x_i(\varphi_f, \varphi_i, w, t)$, $x_f^w(\varphi_f, \varphi_i) = x_f(\varphi_f, \varphi_i, w, t)$ and $\partial(x_i^w, x_f^w)/\partial(\varphi_i, \varphi_f)$ is the Jacobian of the transformation. The winding number w is restricted between

127

the winding numbers of the inner and outer circles of the annulus as shown in Fig. B.1. Doing a similar transformation for the variables x'_i, x'_f and substituting these results in Eq. B.10, we arrive at

$$
\langle \mathcal{O}(t) \rangle_{\text{SC}} = \sum_{w,w'=w_{\text{min}}}^{w_{\text{max}}} \int d\varphi_i d\varphi_f d\varphi'_i d\varphi'_f \left| \det \left[\frac{\partial(x_i^w, x_f^w)}{\partial(\varphi_i, \varphi_f)} \right] \right| \left| \det \left[\frac{\partial(x_i^{w'}, x_f^{w'})}{\partial(\varphi'_i, \varphi'_f)} \right] \right| \delta(x_i^w - x_i^{w'})
$$

$$
\times \delta(x_f^w - x_f^{w'}) \mathcal{O} \left(\frac{x_f^w + x_f^{w'}}{2}, \frac{p_f^w + p_f^{w'}}{2} \right) W_0 \left(\frac{x_i^w + x_i^{w'}}{2}, \frac{p_i^w + p_i^{w'}}{2} \right)
$$

$$
\times \sqrt{\mathcal{D}^w \mathcal{D}^{w'}} \, e^{i\mathcal{S}^w - i\mathcal{S}^{w'} - i(\mu^w - \mu^{w'})\pi/2}, \tag{B.12}
$$

where the arguments of quantities with superscript w and w' are $(\varphi_i, \varphi_f, t)$ and $(\varphi'_i, \varphi'_f, t)$, respectively. Moreover, we have introduced $\mathcal{D}^w(\varphi_f, \varphi_i, t) = \mathcal{D}^c(x_f^w, x_i^w, t)$ and $\mathcal{S}^w(\varphi_f, \varphi_i, t)$ is given by Eq. B.7.

3. To proceed further, we need to explicitly write all the quantities appearing in Eq. B.12 in terms of $(\varphi_f, \varphi_i, w, t)$. For this purpose, we make use of the fact that the relevant classical motion is restricted in an annulus of width $O(1)$ around $\rho = \sqrt{2N}$ (see Fig. B.1). Therefore, in this region, the phase space coordinates $x_i^w \approx \sqrt{2N} \sin \varphi_i$, $p_i^w \approx \sqrt{2N} \sin \varphi_i$, etc.; which implies that the Jacobian

$$
\left| \det \left[\frac{\partial(x_i^w, x_f^w)}{\partial(\varphi_i, \varphi_f)} \right] \right| \approx 2N |\cos \varphi_i \cos \varphi_f| \tag{B.13}
$$

and

$$
\mathcal{D}^w(\varphi_f, \varphi_i, t) \approx \frac{1}{2UNt |\cos \varphi_i \cos \varphi_f|}, \tag{B.14}
$$

etc. Moreover, as the initial Wigner distribution $W_0(x, p)$ is localized around angle $\varphi = 0$, we can approximate the delta function $\delta(x_i^w - x_i^{w'}) \approx \delta(\varphi_f - \varphi'_f)/(\sqrt{2N} \cos \varphi_f)$.

The other delta function becomes

$$\delta(x_f^w - x_f^{w'}) \approx \frac{\delta(\varphi_f - \varphi_f') + \delta(\varphi_f + \varphi_f' - \pi)}{\sqrt{2N} \cos \varphi_f}.$$ (B.15)

Substituting these approximations into Eq. B.12 and integrating over φ_i' and φ_f', we find

$$\langle \mathcal{O}(t) \rangle_{\mathrm{SC}} = \frac{1}{Ut} \sum_{w,w'=w_{\min}}^{w_{\max}} \int d\varphi_i d\varphi_f \, \mathcal{O}\left(\frac{x_f^w + x_f^{w'}}{2}, \frac{p_f^w + p_f^{w'}}{2} \right) W_0 \left(\frac{x_i^w + x_i^{w'}}{2}, \frac{p_i^w + p_i^{w'}}{2} \right)$$

$$\times \, e^{i\mathscr{S}^w - i\mathscr{S}^{w'} - i(\mu^w - \mu^{w'})\pi/2},$$ (B.16)

where we have neglected the term arising from the second term in Eq. B.15. Now the arguments of quantities with either superscript w or w' are φ_f, φ_i and t.

Next, we use the fact that $\mathcal{O}(x,p)$ is a slowly varying function of x, p. So within the annulus of interest, we can write $\mathcal{O}\left(\frac{x_f^w + x_f^{w'}}{2}, \frac{p_f^w + p_f^{w'}}{2} \right) \approx \mathcal{O}(\sqrt{2N} \sin \varphi_f, \sqrt{2N} \cos \varphi_f)$. In particular,

$$a \left(\frac{x_f^w + x_f^{w'}}{2}, \frac{p_f^w + p_f^{w'}}{2} \right) \approx i\sqrt{N} e^{-i\varphi_f}.$$ (B.17)

We *cannot* make a similar approximation for initial Wigner function, i.e., replace ρ by $\sqrt{2N}$, because it varies sharply around $\rho = \sqrt{2N}$. We write

$$W_0 \left(\tfrac{1}{2}(x_i^w + x_i^{w'}), \tfrac{1}{2}(p_i^w + p_i^{w'}) \right) = W_0 \left(\tfrac{1}{2}(\rho^w + \rho^{w'}) \sin \varphi_i, \tfrac{1}{2}(\rho^w + \rho^{w'}) \cos \varphi_i \right).$$ (B.18)

From $\omega = U\rho^2$, we have

$$\frac{\rho^w(\varphi_f, \varphi_i, t)}{\sqrt{2N}} = \left[\frac{(\varphi_f - \varphi_i) \bmod 2\pi + 2\pi w}{UNt} \right]^{1/2}$$

$$\approx 1 + \frac{1}{2} \left[\frac{(\varphi_f - \varphi_i) \bmod 2\pi + 2\pi w}{2UNt} - 1 \right],$$ (B.19)

129

where we have Taylor expanded around $\rho/\sqrt{2N} = 1$. Substituting this expression in Eq. 5.21, we find

$$W_0 \left(\frac{x_i^w + x_i^{w'}}{2}, \frac{p_i^w + p_i^{w'}}{2} \right) \approx \exp \left\{ -\frac{[(\varphi_f - \varphi_i) \bmod 2\pi + \pi(w + w') - UNt]^2}{2U^2Nt^2} - 2N\varphi_i^2 \right\}.$$

(B.20)

Also, from Eq. B.7, we have

$$\mathscr{S}^w - \mathscr{S}^{w'} = \frac{2\pi(w - w')[(\varphi_f - \varphi_i) \bmod 2\pi + \pi(w + w')]}{Ut}.$$

(B.21)

Finally, the Maslov index, which is the number of turning points in the x-coordinates of a classical path, increases by two for every winding. Therefore,

$$\mu^w - \mu^{w'} = 2(w - w').$$

(B.22)

After substituting $\mathcal{O}(x, p) = a(x, p)$, Eqs. B.17, B.20, B.21 and B.22 in Eq. B.16, we find

$$\langle a(t) \rangle_{\mathrm{SC}} = \frac{i\sqrt{N}}{\pi Ut} \sum_{w,w'=w_{\min}}^{w_{\max}} \int_{-\pi}^{\pi} d\varphi_i \int_{-\pi}^{\pi} d\varphi_f \, e^{-i\varphi_f} e^{-\left[(\varphi_f - \varphi_i) \bmod 2\pi + \pi(w+w') - UNt\right]^2/(2U^2Nt^2)}$$

$$\times e^{-2N\varphi_i^2} e^{i2\pi(w-w')[(\varphi_f - \varphi_i) \bmod 2\pi + \pi(w+w')]/(Ut) - i(w-w')\pi}.$$

(B.23)

Now the limits on the winding number can be extended to $[0, \infty)$ as the winding numbers $w_{\min}$ and $w_{\max}$ enclose the range where the initial Wigner distribution in Eq. B.20 is peaked. Finally, writing the sum over w and w' in terms of $u = w + w'$ and $v = w - w'$ and integrating over the angles, we arrive at

$$\langle a(t) \rangle_{\mathrm{SC}} = \sum_{v=-\infty}^{\infty} i\sqrt{N} e^{-iUNt} e^{-2N(\pi v - Ut/2)^2} e^{-1/(8N)}$$

$$\approx \sum_{v=-\infty}^{\infty} i\sqrt{N} e^{-iUNt} e^{-2N(\pi v - Ut/2)^2},$$

(B.24)

which is Eq. 5.23 of the main text.

B.4.1 Derivation of Eq. B.11

Here, we derive Eq. B.11. We restrict our attention to the paths that start from the phase-space region where the initial Wigner distribution is peaked, which is shown by a blue solid circle in Fig. B.1. They lie in an annulus shown in gray in the figure. Now, the winding number of a path at a fixed traversal time is a monotonically non-decreasing function of the radius of the circle on which it lies. Let the (time-dependent) winding number of a path which lies on the inner and outer circle of the annulus be $w_{\min}$ and $w_{\max}$, respectively, with $w_{\min} \leq w_{\max}$. Then, there can be two relevant paths for a given winding number which reaches the final position x_f from position x_i in a given time t. Figure B.1 shows a pair of such paths with winding number 0, which start from $x_i = 0$. Moreover, one of the paths ends in the upper half $(p > 0)$ and the other in the lower half $(p \leq 0)$ of the phase space. Therefore, we can interchange the integrals over boundary conditions and sum over paths to find

$$\int dx_i dx_f \sum_c (\dots) = \sum_{w=w_{\min}, \text{upper}}^{w_{\max}} \int dx_i dx_f (\dots) + \sum_{w=w_{\min}, \text{lower}}^{w_{\max}} \int dx_i dx_f (\dots),$$

(B.25)

where the subscripts upper and lower indicate sum over paths that end in the upper and lower half of the phase space, respectively.

Now in each half of the phase space, the final angle is uniquely determined given (x_f, x_i, w, t). Therefore, we can now change the measure in terms of the angles

and combine the sum to find

$$\int dx_i dx_f \sum_c (\dots) = \sum_{w=w_{\text{min}}}^{w_{\text{max}}} \int_{-\pi}^{\pi} d\varphi_f \int_{-\pi}^{\pi} d\varphi_i \left| \det \left[\frac{\partial(x_i^w, x_f^w)}{\partial(\varphi_i, \varphi_f)} \right] \right| (\dots), \qquad \text{(B.26)}$$

where $x_i^w(\varphi_f, \varphi_i) = x_i(\varphi_f, \varphi_i, w, t)$, $x_f^w(\varphi_f, \varphi_i) = x_f(\varphi_f, \varphi_i, w, t)$ and $\partial(x_i^w, x_f^w)/\partial(\varphi_i, \varphi_f)$

is the Jacobian of the transformation.

$\square$

Bibliography

[1] A. Einstein. Quantentheorie des einatomigen idealen gases. 2. Abhandlung. *Sitzungsberichte der Preussischen Akademie der Wissenschaften, Physikalisch-mathematische Klasse*, pages 3–14, 1925.

[2] M. H. Anderson, J. R. Ensher, M. R. Matthews, C. E. Wieman, and E. A. Cornell. Observation of Bose-Einstein Condensation in a Dilute Atomic Vapor. *Science*, 269(5221):198–201, July 1995.

[3] C.J. Pethick and H. Smith. *Bose-Einstein Condensation in Dilute Gases*. Cambridge University Press, 2008.

[4] M.-O. Mewes, M. R. Andrews, D. M. Kurn, D. S. Durfee, C. G. Townsend, and W. Ketterle. Output coupler for Bose-Einstein condensed atoms. *Phys. Rev. Lett.*, 78(4):582–585, January 1997.

[5] E. W. Hagley, L. Deng, M. Kozuma, J. Wen, K. Helmerson, S. L. Rolston, and W. D. Phillips. A well-collimated quasi-continuous atom laser. *Science*, 283(5408):1706–1709, March 1999.

[6] A. D. Cronin, J. Schmiedmayer, and D. E. Pritchard. Optics and interferometry with atoms and molecules. *Rev. Mod. Phys.*, 81(3):1051–1129, July 2009.

[7] J. Estève, C. Gross, A. Weller, S. Giovanazzi, and M. K. Oberthaler. Squeezing and entanglement in a Bose-Einstein condensate. *Nature*, 455(7217):1216–1219, October 2008.

[8] O. Penrose and L. Onsager. Bose-Einstein condensation and liquid Helium. *Physical Review*, 104(3):576–584, November 1956.

[9] A. J. Leggett. *Quantum liquids: Bose condensation and Cooper pairing in condensed-matter systems*. Oxford University Press, Oxford, 2006.

[10] N. D. Mermin and H. Wagner. Absence of ferromagnetism or antiferromagnetism in one- or two-dimensional isotropic Heisenberg models. *Phys. Rev. Lett.*, 17(22):1133–1136, November 1966.

[11] P. C. Hohenberg. Existence of long-range order in one and two dimensions. *Physical Review*, 158(2):383–386, June 1967.

[12] T. L. Curtright, D. B. Fairlie, and C. K. Zachos. *A Concise Treatise on Quantum Mechanics in Phase Space.* World Scientific, Singapore, 2014.

[13] W. B. Case. Wigner functions and Weyl transforms for pedestrians. *American Journal of Physics*, 76(10):937–946, October 2008.

[14] H. J. Metcalf and P. van der Straten. *Laser cooling and trapping.* Springer Science & Business Media, 2012.

[15] W. D. Phillips. Nobel lecture: Laser cooling and trapping of neutral atoms. *Rev. Mod. Phys.*, 70(3):721, 1998.

[16] W. Ketterle, D. S. Durfee, and D. M. Stamper-Kurn. Making, probing and understanding Bose-Einstein condensates. *arXiv:cond-mat/9904034*, April 1999.

[17] R. Mathew and E. Tiesinga. Controlling the group velocity of colliding atomic Bose-Einstein condensates with Feshbach resonances. *Phys. Rev. A*, 87(5), 2013.

[18] R. Mathew, A. Kumar, S. Eckel, F. Jendrzejewski, G. K. Campbell, Mark Edwards, and E. Tiesinga. Self-heterodyne detection of the *in situ* phase of an atomic superconducting quantum interference device. *Phys. Rev. A*, 92(3), 2015.

[19] R. Mathew and E. Tiesinga. Phase-space mixing in dynamically unstable, integrable few-mode quantum systems. *Phys. Rev. A*, 96(1):013604, July 2017.

[20] M. R. Andrews, C. G. Townsend, H.-J. Miesner, D. S. Durfee, D. M. Kurn, and W. Ketterle. Observation of interference between two Bose condensates. *Science*, 275(5300):637–641, January 1997.

[21] J. Baudon, M. Hamamda, J. Grucker, M. Boustimi, F. Perales, G. Dutier, and M. Ducloy. Negative-index media for matter-wave optics. *Phys. Rev. Lett.*, 102(14):140403, April 2009.

[22] L. Deng, E. W. Hagley, J. Wen, M. Trippenbach, Y. Band, P. S. Julienne, J. E. Simsarian, K. Helmerson, S. L. Rolston, and W. D. Phillips. Four-wave mixing with matter waves. *Nature*, 398(6724):218–220, March 1999.

[23] K. V. Kheruntsyan, J.-C. Jaskula, P. Deuar, M. Bonneau, G. B. Partridge, J. Ruaudel, R. Lopes, D. Boiron, and C. I. Westbrook. Violation of the cauchy-schwarz inequality with matter waves. *Phys. Rev. Lett.*, 108(26):260401, June 2012.

[24] M. Fleischhauer, A. Imamoglu, and J. P. Marangos. Electromagnetically induced transparency: Optics in coherent media. *Rev. Mod. Phys.*, 77(2):633–673, July 2005.

[25] L. V. Hau, S. E. Harris, Z. Dutton, and C. H. Behroozi. Light speed reduction to 17 metres per second in an ultracold atomic gas. *Nature*, 397(6720):594–598, February 1999.

[26] N. S. Ginsberg, S. R. Garner, and L. V. Hau. Coherent control of optical information with matter wave dynamics. *Nature*, 445(7128):623–626, February 2007.

[27] M. M. Kash, V. A. Sautenkov, A. S. Zibrov, L. Hollberg, G. R. Welch, M. D. Lukin, Y. Rostovtsev, E. S. Fry, and M. O. Scully. Ultraslow group velocity and enhanced nonlinear optical effects in a coherently driven hot atomic gas. *Phys. Rev. Lett.*, 82(26):5229–5232, June 1999.

[28] C. Chin, R. Grimm, P. Julienne, and E. Tiesinga. Feshbach resonances in ultracold gases. *Rev. Mod. Phys.*, 82(2):1225–1286, April 2010.

[29] M. Inguscio, W. Ketterle, and C. Salomon, editors. *Ultracold Fermi Gases*. IOS Press, Amsterdam, 2008. Proceedings of the International School of Physics "Enrico Fermi," Course CLXIV, Varenna, 20-30 June 2006.

[30] S. Giorgini, L. P. Pitaevskii, and S. Stringari. Theory of ultracold atomic Fermi gases. *Rev. Mod. Phys.*, 80(4):1215–1274, October 2008.

[31] T. Weber, J. Herbig, M. Mark, H.-C. Nägerl, and R. Grimm. Bose-Einstein condensation of Cesium. *Science*, 299(5604):232–235, January 2003.

[32] S. L. Cornish, N. R. Claussen, J. L. Roberts, E. A. Cornell, and C. E. Wieman. Stable ^{85}Rb Bose-Einstein condensates with widely tunable interactions. *Phys. Rev. Lett.*, 85(9):1795–1798, August 2000.

[33] G. Roati, M. Zaccanti, C. D'Errico, J. Catani, M. Modugno, A. Simoni, M. Inguscio, and G. Modugno. ^{39}K Bose-Einstein condensate with tunable interactions. *Phys. Rev. Lett.*, 99(1):010403, July 2007.

[34] L. Mathey, E. Tiesinga, P. S. Julienne, and C. W. Clark. Collisional cooling of ultracold-atom ensembles using Feshbach resonances. *Phys. Rev. A*, 80(3):030702, September 2009.

[35] R. Ciuryło, E. Tiesinga, and P. S. Julienne. Optical tuning of the scattering length of cold alkaline-earth-metal atoms. *Phys. Rev. A*, 71(3):030701, March 2005.

[36] S. Blatt, T. L. Nicholson, B. J. Bloom, J. R. Williams, J. W. Thomsen, P. S. Julienne, and J. Ye. Measurement of optical Feshbach resonances in an ideal gas. *Phys. Rev. Lett.*, 107(7):073202, August 2011.

[37] Mi Yan, B. J. DeSalvo, B. Ramachandhran, H. Pu, and T. C. Killian. Controlling condensate collapse and expansion with an optical Feshbach resonance. *Phys. Rev. Lett.*, 110(12):123201, March 2013.

[38] J. R. Taylor. *Scattering Theory: The Quantum Theory of Nonrelativistic Collisions.* Dover, New York, 2006.

[39] T. Köhler, K. Góral, and P. S. Julienne. Production of cold molecules via magnetically tunable Feshbach resonances. *Rev. Mod. Phys.*, 78(4):1311–1361, 2006.

[40] T. Köhler and K. Burnett. Microscopic quantum dynamics approach to the dilute condensed Bose gas. *Phys. Rev. A*, 65(3):033601, February 2002.

[41] T. Gasenzer. High-light-intensity photoassociation in a Bose-Einstein condensate. *Phys. Rev. A*, 70(2):021603, August 2004.

[42] A. P. Chikkatur, A. Görlitz, D. M. Stamper-Kurn, S. Inouye, S. Gupta, and W. Ketterle. Suppression and enhancement of impurity scattering in a Bose-Einstein condensate. *Phys. Rev. Lett.*, 85(3):483–486, July 2000.

[43] Y. B. Band, M. Trippenbach, J. P. Burke, and P. S. Julienne. Elastic scattering loss of atoms from colliding Bose-Einstein condensate wave packets. *Phys. Rev. Lett.*, 84(24):5462–5465, June 2000.

[44] J. M. Vogels, K. Xu, and W. Ketterle. Generation of macroscopic pair-correlated atomic beams by four-wave mixing in Bose-Einstein condensates. *Phys. Rev. Lett.*, 89(2):020401, June 2002.

[45] J. Chwedeńczuk, M. Trippenbach, and K. Rzążewski. Elastic scattering losses in the four-wave mixing of Bose-Einstein condensates. *J. Phys. B*, 37(24):L391, December 2004.

[46] C. Buggle, J. Léonard, W. von Klitzing, and J. T. M. Walraven. Interferometric determination of the s and d-wave scattering amplitudes in ^{87}Rb. *Phys. Rev. Lett.*, 93(17):173202, October 2004.

[47] N. R. Thomas, N. Kjærgaard, P. S. Julienne, and A. C. Wilson. Imaging of s and d partial-wave interference in quantum scattering of identical bosonic atoms. *Phys. Rev. Lett.*, 93(17):173201, October 2004.

[48] B. T. Seaman, M. Krämer, D. Z. Anderson, and M. J. Holland. Atomtronics: Ultracold-atom analogs of electronic devices. *Phys. Rev. A*, 75(2):023615, February 2007.

[49] J. G. Lee, B. J. McIlvain, C. J. Lobb, and W. T. Hill III. Analogs of basic electronic circuit elements in a free-space atom chip. *Sci. Rep.*, 3:1034, January 2013.

[50] S. Krinner, D. Stadler, D. Husmann, J.-P. Brantut, and T. Esslinger. Observation of quantized conductance in neutral matter. *Nature*, 517(7532):64–67, January 2015.

[51] M. C. Beeler, R. A. Williams, K. Jiménez-García, L. J. LeBlanc, A. R. Perry, and I. B. Spielman. The spin Hall effect in a quantum gas. *Nature*, 498(7453):201–204, June 2013.

[52] A. Ramanathan, K. C. Wright, S. R. Muniz, M. Zelan, W. T. Hill, C. J. Lobb, K. Helmerson, W. D. Phillips, and G. K. Campbell. Superflow in a toroidal Bose-Einstein condensate: An atom circuit with a tunable weak link. *Phys. Rev. Lett.*, 106(13):130401, March 2011.

[53] K. C. Wright, R. B. Blakestad, C. J. Lobb, W. D. Phillips, and G. K. Campbell. Driving phase slips in a superfluid atom circuit with a rotating weak link. *Phys. Rev. Lett.*, 110(2):025302, January 2013.

[54] S. Eckel, J. G. Lee, F. Jendrzejewski, N. Murray, C. W. Clark, C. J. Lobb, W. D. Phillips, M. Edwards, and G.K. Campbell. Hysteresis in a quantized superfluid atomtronic circuit. *Nature*, 506(7487):200–203, February 2014.

[55] C. Ryu, P. W. Blackburn, A. A. Blinova, and M. G. Boshier. Experimental realization of Josephson junctions for an atom SQUID. *Phys. Rev. Lett.*, 111(20):205301, November 2013.

[56] F. Jendrzejewski, S. Eckel, N. Murray, C. Lanier, M. Edwards, C. J. Lobb, and G. K. Campbell. Resistive flow in a weakly interacting Bose-Einstein condensate. *Phys. Rev. Lett.*, 113(4):045305, July 2014.

[57] L. Amico, D. Aghamalyan, F. Auksztol, H. Crepaz, R. Dumke, and L. C. Kwek. Superfluid qubit systems with ring shaped optical lattices. *Sci. Rep.*, 4:4298, March 2014.

[58] D. Aghamalyan, M. Cominotti, M. Rizzi, D. Rossini, F. Hekking, A. Minguzzi, L.-C. Kwek, and L. Amico. Coherent superposition of current flows in an atomtronic quantum interference device. *New J. Phys.*, 17(4):045023, April 2015.

[59] V. A. Kashurnikov, A. I. Podlivaev, N. V. Prokof'ev, and B. V. Svistunov. Supercurrent states in one-dimensional finite-size rings. *Phys. Rev. B*, 53(19):13091–13105, May 1996.

[60] Yu. Kagan, N. V. Prokof'ev, and B. V. Svistunov. Supercurrent stability in a quasi-one-dimensional weakly interacting Bose gas. *Phys. Rev. A*, 61(4):045601, March 2000.

[61] H. P. Büchler, V. B. Geshkenbein, and G. Blatter. Superfluidity versus Bloch oscillations in confined atomic gases. *Phys. Rev. Lett.*, 87(10):100403, August 2001.

[62] M. Cominotti, D. Rossini, M. Rizzi, F. Hekking, and A. Minguzzi. Optimal persistent currents for interacting bosons on a ring with a gauge field. *Phys. Rev. Lett.*, 113(2):025301, July 2014.

[63] K.K. Likharev. Superconducting weak links. *Rev. Mod. Phys.*, 51(1):101–159, January 1979.

[64] M. R. Andrews, C. G. Townsend, H.-J. Miesner, D. S. Durfree, D. M. Kurn, and W. Ketterle. Observation of interference between two Bose condensates. *Science*, 275(5300):637, January 1997.

[65] Y. Castin and J. Dalibard. Relative phase of two Bose-Einstein condensates. *Phys. Rev. A*, 55(6):4330–4337, June 1997.

[66] J. E. Simsarian, J. Denschlag, M. Edwards, C. W. Clark, L. Deng, E. W. Hagley, K. Helmerson, S. L. Rolston, and W. D. Phillips. Imaging the phase of an evolving Bose-Einstein condensate wave function. *Phys. Rev. Lett.*, 85(10):2040–2043, September 2000.

[67] S. Inouye, S. Gupta, T. Rosenband, A. P. Chikkatur, A. Görlitz, T. L. Gustavson, A. E. Leanhardt, D. E. Pritchard, and W. Ketterle. Observation of vortex phase singularities in Bose-Einstein condensates. *Phys. Rev. Lett.*, 87(8):080402, August 2001.

[68] Z. Hadzibabic, P. Krüger, M. Cheneau, B. Battelier, and J. Dalibard. Berezinskii-Kosterlitz-Thouless crossover in a trapped atomic gas. *Nature*, 441(7097):1118–21, June 2006.

[69] C. Kohstall, S. Riedl, E. R. Sánchez Guajardo, L. A. Sidorenkov, J. Hecker Denschlag, and R. Grimm. Observation of interference between two molecular Bose-Einstein condensates. *New J. Phys.*, 13(6):065027, June 2011.

[70] Y. Shin, C. Sanner, G.-B. Jo, T. A. Pasquini, M. Saba, W. Ketterle, D. E. Pritchard, M. Vengalattore, and M. Prentiss. Interference of Bose-Einstein condensates split with an atom chip. *Phys. Rev. A*, 72(2):021604, August 2005.

[71] L. Corman, L. Chomaz, T. Bienaimé, R. Desbuquois, C. Weitenberg, S. Nascimbène, J. Dalibard, and J. Beugnon. Quench-induced supercurrents in an annular Bose gas. *Phys. Rev. Lett.*, 113(13):135302, September 2014.

[72] S. Eckel, F. Jendrzejewski, A. Kumar, C. J. Lobb, and G. K. Campbell. Interferometric measurement of the current-phase relationship of a superfluid weak link. *Phys. Rev. X*, 4(3):031052, September 2014.

[73] L. Richter, H. Mandelberg, M. Kruger, and P. McGrath. Linewidth determination from self-heterodyne measurements with subcoherence delay times. *IEEE J. Quantum Electron.*, 22(11):2070–2074, November 1986.

[74] R. P. Feynman, A. R. Hibbs, and D. F. Styer. *Quantum Mechanics and Path Integrals: Emended Edition*. Dover Publications, 2010.

[75] C. M. Bender and S. A. Orszag. *Advanced Mathematical Methods for Scientists and Engineers*. McGraw-Hill, New York, 1978.

[76] Y. Castin and R. Dum. Bose-Einstein condensates in time dependent traps. *Phys. Rev. Lett.*, 77(27):5315–5319, December 1996.

[77] M. Edwards, M. Krygier, H. Seddiqi, B. Benton, and C. W. Clark. Approximate mean-field equations of motion for quasi-two-dimensional Bose-Einstein-condensate systems. *Phys. Rev. E*, 86:056710, Nov 2012.

[78] V. M. Pérez-García, H. Michinel, J. I. Cirac, M. Lewenstein, and P. Zoller. Dynamics of Bose-Einstein condensates: Variational solutions of the Gross-Pitaevskii equations. *Phys. Rev. A*, 56:1424–1432, Aug 1997.

[79] Yu. Kagan, E. L. Surkov, and G. V. Shlyapnikov. Evolution of a Bose-condensed gas under variations of the confining potential. *Phys. Rev. A*, 54(3):R1753–R1756, September 1996.

[80] I. Bloch, J. Dalibard, and W. Zwerger. Many-body physics with ultracold gases. *Rev. Mod. Phys.*, 80(3):885–964, July 2008.

[81] J. Dziarmaga. Dynamics of a quantum phase transition and relaxation to a steady state. *Advances in Physics*, 59(6):1063–1189, November 2010.

[82] L. D'Alessio, Y. Kafri, A. Polkovnikov, and M. Rigol. From quantum chaos and eigenstate thermalization to statistical mechanics and thermodynamics. *Advances in Physics*, 65(3):239–362, May 2016.

[83] T. Kinoshita, T. Wenger, and D. S. Weiss. A quantum Newton's cradle. *Nature*, 440(7086):900–903, April 2006.

[84] T. Langen, S. Erne, R. Geiger, B. Rauer, T. Schweigler, M. Kuhnert, W. Rohringer, I.E. Mazets, T. Gasenzer, and J. Schmiedmayer. Experimental observation of a generalized Gibbs ensemble. *Science*, 348(6231):207–211, April 2015.

[85] V.I. Arnold. *Mathematical Methods of Classical Mechanics*. Graduate Texts in Mathematics. Springer New York, 1997.

[86] V.E. Korepin, N.M. Bogoliubov, and A.G. Izergin. *Quantum Inverse Scattering Method and Correlation Functions*. Cambridge Monographs on Mathematical Physics. Cambridge University Press, 1997.

[87] A. Smerzi, S. Fantoni, S. Giovanazzi, and S. R. Shenoy. Quantum coherent atomic tunneling between two trapped Bose-Einstein condensates. *Phys. Rev. Lett.*, 79(25):4950–4953, December 1997.

[88] C. K. Law, H. Pu, and N. P. Bigelow. Quantum spins mixing in spinor Bose-Einstein condensates. *Phys. Rev. Lett.*, 81:5257–5261, December 1998.

[89] W. Zhang, D. L. Zhou, M.-S. Chang, M. S. Chapman, and L. You. Coherent spin mixing dynamics in a spin-1 atomic condensate. *Phys. Rev. A*, 72(1):013602, July 2005.

[90] S. Mossmann and C. Jung. Semiclassical approach to Bose-Einstein condensates in a triple well potential. *Phys. Rev. A*, 74(3):033601, September 2006.

[91] A. P. Itin and P. Schmelcher. Semiclassical spectrum of small Bose-Hubbard chains: A normal-form approach. *Phys. Rev. A*, 84(6):063609, December 2011.

[92] I. I. Satija, C. L. Pando L., and E. Tiesinga. Soliton dynamics of an atomic spinor condensate on a ring lattice. *Phys. Rev. A*, 87(3):033608, March 2013.

[93] H. Pu, C. K. Law, J. H. Eberly, and N. P. Bigelow. Coherent disintegration and stability of vortices in trapped Bose condensates. *Phys. Rev. A*, 59(2):1533–1537, February 1999.

[94] D.V. Skryabin. Instabilities of vortices in a binary mixture of trapped Bose-Einstein condensates: Role of collective excitations with positive and negative energies. *Phys. Rev. A*, 63(1):013602, December 2000.

[95] Y. Kawaguchi and T. Ohmi. Splitting instability of a multiply charged vortex in a Bose-Einstein condensate. *Phys. Rev. A*, 70(4):043610, October 2004.

[96] B. Wu and Q. Niu. Landau and dynamical instabilities of the superflow of Bose-Einstein condensates in optical lattices. *Phys. Rev. A*, 64(6):061603, November 2001.

[97] C. Menotti, A. Smerzi, and A. Trombettoni. Superfluid dynamics of a Bose-Einstein condensate in a periodic potential. *New Journal of Physics*, 5(1):112, 2003.

[98] M. G. Moore, O. Zobay, and P. Meystre. Quantum optics of a Bose-Einstein condensate coupled to a quantized light field. *Phys. Rev. A*, 60(2):1491–1506, August 1999.

[99] Y. Shin, M. Saba, M. Vengalattore, T. A. Pasquini, C. Sanner, A. E. Leanhardt, M. Prentiss, D. E. Pritchard, and W. Ketterle. Dynamical instability of a doubly quantized vortex in a Bose-Einstein condensate. *Phys. Rev. Lett.*, 93(16):160406, October 2004.

[100] L. Fallani, L. De Sarlo, J. E. Lye, M. Modugno, R. Saers, C. Fort, and M. Inguscio. Observation of dynamical instability for a Bose-Einstein condensate in a moving 1d optical lattice. *Phys. Rev. Lett.*, 93(14):140406, September 2004.

[101] M. Cristiani, O. Morsch, N. Malossi, M. Jona-Lasinio, M. Anderlini, E. Courtade, and E. Arimondo. Instabilities of a Bose-Einstein condensate in a periodic potential: an experimental investigation. *Optics Express*, 12(1):4–10, January 2004.

[102] A. J. Ferris, M. J. Davis, R. W. Geursen, P. B. Blakie, and A. C. Wilson. Dynamical instabilities of Bose-Einstein condensates at the band edge in one-dimensional optical lattices. *Phys. Rev. A*, 77(1):012712, January 2008.

[103] D. Schmidt, H. Tomczyk, S. Slama, and C. Zimmermann. Dynamical instability of a Bose-Einstein condensate in an optical ring resonator. *Phys. Rev. Lett.*, 112(11):115302, March 2014.

[104] S. R. Leslie, J. Guzman, M. Vengalattore, J. D. Sau, M. L. Cohen, and D. M. Stamper-Kurn. Amplification of fluctuations in a spinor Bose-Einstein condensate. *Phys. Rev. A*, 79(4):043631, April 2009.

[105] C. Klempt, O. Topic, G. Gebreyesus, M. Scherer, T. Henninger, P. Hyllus, W. Ertmer, L. Santos, and J. J. Arlt. Parametric amplification of vacuum fluctuations in a spinor condensate. *Phys. Rev. Lett.*, 104(19):195303, May 2010.

[106] C. D. Hamley, C. S. Gerving, T. M. Hoang, E. M. Bookjans, and M. S. Chapman. Spin-nematic squeezed vacuum in a quantum gas. *Nature Physics*, 8(4):305–308, April 2012.

[107] A. Sinatra, C. Lobo, and Y. Castin. The truncated Wigner method for Bose-condensed gases: limits of validity and applications. *Journal of Physics B: Atomic, Molecular and Optical Physics*, 35(17):3599, 2002.

[108] P. B. Blakie, A. S. Bradley, M. J. Davis, R. J. Ballagh, and C. W. Gardiner. Dynamics and statistical mechanics of ultra-cold Bose gases using c-field techniques. *Advances in Physics*, 57(5):363–455, September 2008.

[109] A. Polkovnikov. Phase space representation of quantum dynamics. *Annals of Physics*, 325(8):1790–1852, August 2010.

[110] J. D. Sau, S. R. Leslie, M. L. Cohen, and D. M. Stamper-Kurn. Spin squeezing of high-spin, spatially extended quantum fields. *New Journal of Physics*, 12(8):085011, 2010.

[111] R. Barnett, A. Polkovnikov, and M. Vengalattore. Prethermalization in quenched spinor condensates. *Phys. Rev. A*, 84(2):023606, August 2011.

[112] J. Larson, B. M. Anderson, and A. Altland. Chaos-driven dynamics in spin-orbit-coupled atomic gases. *Phys. Rev. A*, 87(1):013624, January 2013.

[113] J. G. Cosme and O. Fialko. Thermalization in closed quantum systems: Semiclassical approach. *Phys. Rev. A*, 90(5), 2014.

[114] A. C. Mathey, C. W. Clark, and L. Mathey. Decay of a superfluid current of ultracold atoms in a toroidal trap. *Phys. Rev. A*, 90(2):023604, August 2014.

[115] A. Polkovnikov. Quantum corrections to the dynamics of interacting bosons: Beyond the truncated Wigner approximation. *Phy. Rev. A*, 68(5):053604, November 2003.

[116] G. W. Hammett, W. Dorland, and F. W. Perkins. Fluid models of phase mixing, Landau damping, and nonlinear gyrokinetic dynamics. *Physics of Fluids B: Plasma Physics (1989-1993)*, 4(7):2052–2061, July 1992.

[117] S. Tremaine. The geometry of phase mixing. *Monthly Notices of the Royal Astronomical Society*, 307(4):877–883, August 1999.

[118] E. M. Lifshitz and L. P. Pitaevskii. *Physical Kinetics*. Pergamon, Oxford, 1981.

[119] *NIST Digital Library of Mathematical Functions*. http://dlmf.nist.gov/, Release 1.0.13 of 2016-09-16. F. W. J. Olver, A. B. Olde Daalhuis, D. W. Lozier, B. I. Schneider, R. F. Boisvert, C. W. Clark, B. R. Miller and B. V. Saunders, eds.

[120] A. J. Brizard. Jacobi zeta function and action-angle coordinates for the pendulum. *Communications in Nonlinear Science and Numerical Simulation*, 18(3):511–518, March 2013.

[121] I. M. Gelfand and G. E. Shilov. *Generalized functions: Volume I*. Academic Press, New York, NY, 1964.

[122] S. Raghavan, A. Smerzi, S. Fantoni, and S. R. Shenoy. Coherent oscillations between two weakly coupled Bose-Einstein condensates: Josephson effects, π oscillations, and macroscopic quantum self-trapping. *Phys. Rev. A*, 59(1):620–633, January 1999.

[123] A. J. Leggett. Bose-Einstein condensation in the alkali gases: Some fundamental concepts. *Rev. Mod. Phys.*, 73(2):307–356, April 2001.

[124] M. Albiez, R. Gati, J. Fölling, S. Hunsmann, M. Cristiani, and M. K. Oberthaler. Direct observation of tunneling and nonlinear self-trapping in a single bosonic Josephson junction. *Phys. Rev. Lett.*, 95(1):010402, June 2005.

[125] T. Zibold, E. Nicklas, C. Gross, and M. K. Oberthaler. Classical bifurcation at the transition from rabi to Josephson dynamics. *Phys. Rev. Lett.*, 105(20):204101, November 2010.

[126] J. R. Anglin and A. Vardi. Dynamics of a two-mode Bose-Einstein condensate beyond mean-field theory. *Phys. Rev. A*, 64(1):013605, May 2001.

[127] K. W. Mahmud, H. Perry, and W. P. Reinhardt. Quantum phase-space picture of Bose-Einstein condensates in a double well. *Phys. Rev. A*, 71(2):023615, February 2005.

[128] M. Chuchem, K. Smith-Mannschott, M. Hiller, T. Kottos, A. Vardi, and D. Cohen. Quantum dynamics in the bosonic Josephson junction. *Phys. Rev. A*, 82(5):053617, November 2010.

[129] J. Links, H.-Q. Zhou, R. H. McKenzie, and M. D. Gould. Algebraic Bethe ansatz method for the exact calculation of energy spectra and form factors: applications to models of Bose-Einstein condensates and metallic nanograins. *Journal of Physics A: Mathematical and General*, 36(19):R63, 2003.

[130] F. Zhou. Spin correlation and discrete symmetry in spinor Bose-Einstein condensates. *Phys. Rev. Lett.*, 87(8), 2001.

[131] M.-S. Chang, Q. Qin, W. Zhang, L. You, and M. S. Chapman. Coherent spinor dynamics in a spin-1 Bose condensate. *Nature Physics*, 1(2):111–116, November 2005.

[132] A. T. Black, E. Gomez, L. D. Turner, S. Jung, and P. D. Lett. Spinor dynamics in an antiferromagnetic spin-1 condensate. *Phys. Rev. Lett.*, 99(7):070403, August 2007.

[133] Y. Liu, S. Jung, S. E. Maxwell, L. D. Turner, E. Tiesinga, and P. D. Lett. Quantum phase transitions and continuous observation of spinor dynamics in an antiferromagnetic condensate. *Phys Rev. Lett.*, 102(12):125301, March 2009.

[134] E. M. Bookjans, A. Vinit, and C. Raman. Quantum phase transition in an antiferromagnetic spinor Bose-Einstein condensate. *Phys. Rev. Lett.*, 107(19):195306, November 2011.

[135] C.S. Gerving, T.M. Hoang, B.J. Land, M. Anquez, C.D. Hamley, and M.S. Chapman. Non-equilibrium dynamics of an unstable quantum pendulum explored in a spin-1 Bose-Einstein condensate. *Nature Communications*, 3:1169, November 2012.

[136] N. M. Bogoliubov. Spinor bose condensate and the su(1,1) Richardson model. *Journal of Mathematical Sciences*, 136(1):3552–3559, July 2006.

[137] A. Lamacraft. Spin-1 microcondensate in a magnetic field. *Phys. Rev. A*, 83(3):033605, March 2011.

[138] P. Ribeiro, J. Vidal, and R. Mosseri. Exact spectrum of the Lipkin-Meshkov-Glick model in the thermodynamic limit and finite-size corrections. *Phys. Rev. E*, 78(2):021106, August 2008.

[139] G. P. Berman and G.M. Zaslavsky. Logarithm breaking time in quantum chaos. In G. Casati and B. Chirikov, editors, *Quantum Chaos: Between Order and Disorder*, pages 435–446. Cambridge University Press, Cambridge, 004 1995.

[140] F. Nissen and J. Keeling. Wentzel-Kramers-Brillouin approach and quantum corrections to classical dynamics in the Josephson problem. *Phys. Rev. A*, 81(6):063628, June 2010.

[141] J. Rammer. *Quantum transport theory*, volume 99. Westview Press, 2004.

[142] M. S. Marinov. A new type of phase-space path integral. *Phys. Lett. A*, 153(1):5–11, February 1991.

[143] T. Dittrich, E. A. Gómez, and L. A. Pachón. Semiclassical propagation of Wigner functions. *The Journal of Chemical Physics*, 132(21):214102, June 2010.

[144] R. G. Littlejohn. The Van Vleck formula, Maslov theory, and phase space geometry. *Journal of Statistical Physics*, 68(1-2):7–50, July 1992.

[145] L. S. Schulman. *Techniques and applications of path integration*. Dover Publications, 2005.

[146] M. C. Gutzwiller. Periodic Orbits and Classical Quantization Conditions. *Journal of Mathematical Physics*, 12(3):343–358, March 1971.

[147] P. W. Brouwer and A. Altland. Anderson localization from classical trajectories. *Phys. Rev. B*, 78(7):075304, August 2008.

[148] M. Greiner, O. Mandel, T. W. Hänsch, and I. Bloch. Collapse and revival of the matter wave field of a Bose-Einstein condensate. *Nature*, 419(6902):51–54, September 2002.

[149] G. Kirchmair, B. Vlastakis, Z. Leghtas, S. E. Nigg, H. Paik, E. Ginossar, M. Mirrahimi, L. Frunzio, S. M. Girvin, and R. J. Schoelkopf. Observation of quantum state collapse and revival due to the single-photon Kerr effect. *Nature*, 495(7440):205–209, March 2013.

[150] C. Tian, A. Kamenev, and A. Larkin. Ehrenfest time in the weak dynamical localization. *Phys. Rev. B*, 72(4):045108, July 2005.

[151] M. Gabbrielli, L. Pezzè, and A. Smerzi. Spin-Mixing Interferometry with Bose-Einstein Condensates. *Phys. Rev. Lett.*, 115(16):163002, October 2015.